

Friction Stir Processing of AZ31 Magnesium Alloy

Thesis

submitted in partial fulfilment of the requirements for the degree of

Doctor of Philosophy

from

Indian Institute of Technology Bombay, India
&
Monash University, Australia

by

Abhishek Tripathi

Supervisors:

**Prof. Indradev Samajdar, Prof. Asim Tewari (IIT Bombay)
Prof. Jian-Feng Nie (Monash University)**



The course of study for this award was developed jointly by Monash University, Australia and the Indian Institute of Technology Bombay and was given academic recognition by each of them. The programme was administrated by The IITB-Monash Research Academy.

January 2016

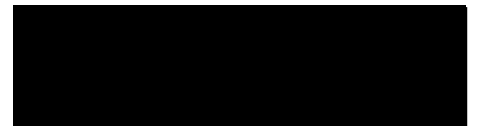
*Dedicated to my parents and
Mr. A K Jha, my physics teacher*

Approval Sheet

The thesis entitled “**Friction Stir Processing of AZ31 Magnesium Alloy**” by Abhishek Tripathi is approved for the degree of **Doctor of Philosophy**.



(Prof. Debalay Chakrabarti)
External Examiner



(Prof. K. Narasimhan)
Internal Examiner



(Prof. Indradev Samajdar)
IITB Supervisor



(Prof. Asim Tewari)
IITB Co-Supervisor



(Prof. Jian-Feng Nie)
Monash Supervisor



(Prof. Santanu Banerjee)
Chairman

Date: 16th May, 2016

Place: IITB-Monash Research Academy, IIT Bombay

Declaration

This thesis contains no material which has been accepted for the award of any other degree or diploma at any university or equivalent institution and that, to the best of my knowledge and belief, this thesis contains no material previously published or written by another person, except where due reference is made in the text of the thesis.

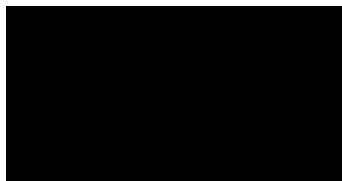
Copyright Notice

Notice 1

Under the Copyright Act 1968, this thesis must be used only under the normal conditions of scholarly fair dealing. In particular no results or conclusions should be extracted from it, nor should it be copied or closely paraphrased in whole or in part without the written consent of the author. Proper written acknowledgment should be made for any assistance obtained from this thesis.

Notice 2

I certify that I have made all reasonable efforts to secure copyright permissions for third-party content included in this thesis and have not knowingly added copyright content to my work without the owner's permission.



Abhishek Tripathi

Date: 16th May 2016

(IITB ID: 10411409, )

Abstract

Magnesium alloys are known to be one of the lightest structural alloys and hence they are of interest to the potential applications in aerospace and automobile industry. However, widescale commercial usage of magnesium alloys is limited given its low formability at room temperature. Conventional processing techniques fail to alter the formability and other mechanical properties significantly. A severe plastic deformation processing technique called friction stir processing (FSP) developed on the principles of friction stir welding (FSW) is touted to significantly change the microstructure, texture and hence the mechanical properties of magnesium alloys. This thesis is primarily based on investigating the mechanisms of microstructure and texture evolution during FSP of a commercial AZ31 magnesium alloy. The work presented in the thesis comprise of four projects, all under the broad theme of investigating the microstructure and texture evolution in AZ31 alloy: (i) Microstructural origin of friction stir processed zone in a magnesium alloy, (ii) Microstructural evolution during multipass friction stir processing of a magnesium alloy, (iii) Friction stir processing under different thermal history, and (iv) Study of grain structure evolution during annealing of a twin roll cast AZ31 Mg alloy.

In (i) microstructural and texture evolution at the edge regions of a friction stir processed (FSP) magnesium alloy AZ31 was studied which was aimed at explaining the mechanism of the microstructural evolution during FSP. A model of microstructural development through grain boundary sliding of the ultra-fine grains was proposed based on the texture and microstructural observations in the concerned regions. Further, in (ii) the microstructure and texture developments and also prediction of texture using visco-plastic-self-consistent (VPSC) modelling of commercial magnesium alloy AZ31 being friction stir processed through multi-pass and multi-directional (unidirectional, reverse and transverse tool movements) was studied. Later, in (iii) the effect of various coolant mediums viz. air, liquid nitrogen and water on the microstructural and thermal profiles in the friction stir processed zone was investigated. Experimental observations, on the process zone dimensions and temperature profiles, showed significant differences: which highlighted the effect of the thermal history. A numerical simulation was made using multi-physics finite element method. A three-dimensional steady-state coupled laminar fluid flow and heat transfer model was

developed, which could capture the experimentally observed process zone dimensions and temperature profiles.

Lastly, in (iv) evolution of microstructure under static annealing at 300°C and 500°C for different times of twin-roll-cast (TRC) magnesium alloy AZ31 was outlined. Grain path envelope analysis was used for quantitatively analyzing the microstructural evolution. Twin-rolled structure had bimodal grain size which was preserved after annealing at 300°C. However, annealing at 500°C led to a unimodal grain size. A deformation induced recrystallization recovery (DIRR) model was proposed which could explain the observed microstructural features.

Acknowledgements

I would begin by acknowledging the person with whom I spent most of my time during my tenure as a PhD candidate. It was a fascinating experience working with Prof. Indradev Samajdar, and I am short of words in expressing my gratitude towards his efforts in moulding me as a person and as a scientist. I have met very few persons in my life with such a level of energy, dedication, focus and hard work, and especially towards his students. I feel very fortunate to have had a supervisor like Prof. Samajdar. His 'never give up' attitude really fascinated me. Working with him was a great learning experience. I really appreciate his contribution towards moulding my thesis. I would like to thank my co-supervisor Prof. Asim Tewari for his constant moral support, encouragement and passionate teaching through-out my tenure. His contagious positive aura always encouraged me to do better. He always showed me the light at the end of the tunnel, which guided me to find solutions in challenging times. The interactions with him were really stimulating and helped in shaping my thoughts about my research work.

I would like to thank my Monash University supervisor Prof. Jian-Feng Nie for making my stay at the Monash University a pleasant and a learning experience and for taking keen interest in my work and discussing at length the details of my research and giving useful comments. I would also like to especially thank Dr. Su-Ming Zhu, for giving me so much of his time and helping me out with the TEM during my stay at Monash University. I am really indebted for all his help.

I would like to thank Prof. K Narashimhan and Prof. Allan Morton, for their useful and precise comments on my work during the course of my candidature, as my research progress committee member.

I would specially like to thank Prof. Roger Doherty, for taking so much interest in discussing my work and giving useful suggestions and I greatly acknowledge his contributions towards shaping my thesis. I enjoyed many technical and informal talks with him on wide ranging subjects and was really honoured to have had a chance to work with him. I would like to thank Prof. A K Kanjarla, for teaching me texture modelling and providing me texture modelling codes. I would also like to thank Dr. N Srinivasan and Dr. G M Reddy, for letting me avail the friction stir processing facilities at DMRL, Hyderabad. I would like to

thank Amelia Liu and Emily Chen for their technical help during my stay at Monash University. I would also like to thank Kashyap Mohan for discussing with me the finite element simulation details.

My stay at IIT Bombay would not have been this memorable without the loving company of my lab-mates. I was fortunate to have such a helpful and understanding lab mates, who were always there to guide and help me. My seniors Prof. Sushil Mishra, Prof. Santosh Sahoo, Dr. Raveendra, Dr. Vijay Hiwarkar, Dr. Satish Kumar, Dr. Ajay Revelly, Lokendra Jain, Dr. Basavaraj, Dr. Ritwik Basu were always there to guide me to the right path. I really enjoyed the company of Jaiveer, Gulshan, Ashish, Srinivasan, Arijith, Durga, Divya, Gyan, Rohan, Geeta, Ram Pratap, Minit, Sourav, Niraj, Aditya, Riya, Partho, Urmilla, Khushal, Hitesh, Ershad, Sukanta, Nasim, Aamir, Soma, Shomik, Manna and Abdul. I am also thankful to my friends Prasanta, Rinkel, Shreya and Swati who were always there for me.

Finally, I would like to thank my loving and caring family, my grandparents, my parents and my two loving sisters Parul and Pallavi, for their constant love and support. I would specially like to thank my mother *Sudha Tripathi*, for her selfless love, care and sacrifices towards me.

Contents

Abstract	ii
List of figures	viii
List of tables	xv
Abbreviations	xvi
Chapter 1	1
Introduction	1
1.1 Background	1
1.2 Framework of the thesis	3
Chapter 2	7
Literature Review	7
2.1 Magnesium: Overview and history	7
2.2 Magnesium alloys	12
2.2.1 Alloys based on Mg-Al system	12
2.2.2 Alloys based on Mg-Zn system	13
2.2.3 Alloys based on Mg-RE system	13
2.2.4 Wrought Mg based alloys	13
2.3 Crystallographic orientation and its representation	15
2.4 Texture analysis in hexagonal materials	17
2.4.1 Texture components in hexagonal materials	18
2.5 Introduction to friction stir welding/processing	21
2.5.1 Microstructural evolution during friction stir processing	23
2.5.2 Texture evolution during friction stir processing	32
2.5.3 Texture simulation during friction stir processing	36
2.5.4 Effect of quenching medium during friction stir processing	39
2.5.5 Finite element simulation of friction stir welding/processing	40
2.6 Introduction to twin roll casting	44
2.7 Introduction to grain path envelope analysis	45
References	48
Chapter 3	55
Microstructural origin of friction stir processed zone in a magnesium alloy	55
3.1 Abstract	55
3.2 Introduction	56
3.3 Experimental methods.....	57
3.4 Results and discussion	59
3.5 Conclusions	62
References	63
Chapter 4	64
Microstructural evolution during multi-pass friction stir processing of a magnesium alloy	64

4.1 Abstract	64
4.2 Introduction	65
4.3 Experimental methods and simulation details	66
4.3.1 Experimental methods	66
4.3.2 Texture simulations	70
4.4 Results	71
4.4.1 Microstructural evolution	71
4.4.2 Development of crystallographic texture	72
4.5 Discussion	80
4.6 Summary	91
References	91
Chapter 5	96
Friction stir processing under different thermal history:Experimental observation and numerical validation	96
5.1 Abstract	96
5.2 Introduction	97
5.3 Experimental methods.....	98
5.4 Three dimensional steady state model	100
5.4.1 Simulation geometry and boundary conditions	100
5.4.2 Equations for steady state material and heat flow	102
5.4.3 Constitutive properties of AZ31 Mg alloy	104
5.4.4 Heat input	105
5.5 Results and discussion	106
5.6 Summary	114
5.7 Appendix.....	115
References	116
Chapter 6	120
Study of grain structure evolution during study of a twin roll cast Mg alloy	120
6.1 Abstract	120
6.2 Introduction	121
6.3 Experimental procedure	123
6.4 Results and discussion	124
6.4.1 Microstructure evolution model	134
6.5 Summary	136
6.6 Appendix.....	137
6.6.1 Grain path envelope formalization	137
References	139
Chapter 7	142
Concluding Remarks	142

List of Figures

Figure 2.1: Schematic of the direction of alloy development for magnesium alloys [2].....	9
Figure 2.2: Isothermal section of the Mg-Zn-Al ternary phase diagram at 593 K [21].....	11
Figure 2.3: Schematic representation of Euler angles using Bunge notation [29].....	16
Figure 2.4: Simulated rolling texture ((0002) and (10 $\bar{1}$ 0) poles) in hexagonal closed packed metals with c/a ratio: (a) ~1.633, (b) >1.633 and (c) <1.633 [30].	18
Figure 2.5: Ideal pole figures of some important texture components for Mg (c/a = 1.624) [30].....	19
Figure 2.6: Ideal ODF positions for some low index orientation of the hexagonal closed pack crystalline structure [30].	20
Figure 2.7: (0002) and (10 $\bar{1}$ 0) pole figures at various locations at the advancing and retreating side of a friction stir welded magnesium alloy AZ61 [38].....	20
Figure 2.8: Schematic drawing of FSW [42].....	21
Figure 2.9: Cross-sectional profile showing the different zone in FSP of 7075Al-T651 [70].	23
Figure 2.10: a) Microstructural evolution in the thermo-mechanically affected zone in FSP 7075Al [83] and (b) optical microstructures in the stir zones in the welds of Al alloys 6063-T5 and T4 [88].	24
Figure 2.11: Effect of FSP parameters and alloy systems on peak temperature [42].....	25
Figure 2.12: (a) Schematic of the stop-action friction stir weld. The sample axis (plate-normal direction (ND), welding direction (WD) and transverse direction (TD)) are also shown. b) Plane view of the section. c) Grain evolution ahead of the tool on the advancing side of the tool [41].....	26
Figure 2.13: Top view of the stop action technique used to freeze the structure [91].....	26
Figure 2.14: (a) EBSD map from ahead of the tool on the advancing side of the weld, showing a grain splitting into deformation bands with two alternating orientations (c) Misorientation profile. (d) Average grain size as a function of distance behind the tool taken along weld centerline [91].	27
Figure 2.15: a) Schematic of the regions where TEM samples were prepared, b) formation of very fine grains in th processed region [81].....	27

Figure 2.16: TEM micrographs of the different regions of the friction stir processed 7075 Al alloy; (a) S1 with the SAD pattern, (b) a dark-field image from S1, (c) S2, (d) S3, (e) S4 and (f) S5 [81].	28
Figure 2.17: Optical micrographs of the AZ31B Mg alloy under FSP: (a) cross-sectional macrostructure; (b) microstructure of the various regions namely SZ, TZ and HAZ; and (c) microstructure through the thickness [61].	29
Figure 2.18: EBSD map taken ahead the tool keyhole (a) and behind the tool keyhole and (b) ahead of the tool [99].	30
Figure 2.19: Microstructure evolution at relatively high welding temperature: (a) the composite EBSD map showing grain structure developed ahead of the welding tool in the stop-action experiment with selected areas shown at higher magnifications in (b)–(e) [109].	31
Figure 2.20: a) Schematic illustration of selected areas for analysis of microtexture, b) (0002) and (10 $\bar{1}$ 0) pole figures of the base material. c) (0002) and (10 $\bar{1}$ 0) pole figures along the middle line (as indicated in (a)) [38].	33
Figure 2.21: a) Schematic of the friction-stir processing, b) basal tracing from the base material, transition region, to stir zone on the advancing side of the FSP Mg plate [63].	34
Figure 2.22: (a) Cross section of the processed zone with tool profile indicated, (b) (0002) and (10 $\bar{1}$ 0) poles of FSP AZ31 material measured at different locations as shown in (a) [105].	34
Figure 2.23: Basal (0002) pole figures from the top surface of a FSW joint made at a welding speed of 5 mm/s and tool rotational rate of 1000 rpm at different locations [121].	35
Figure 2.24: (0002) and (10 $\bar{1}$ 0) pole figures of AZ91 in (a) as-cast, (b) one-pass FSP and (c) two-pass FSP [120].	36
Figure 2.25: Streamline plot at various locations of FSW. Region 1 indicates the retreating side and region 2 indicates the advancing side. Nine streamlines are indicated from (a) through (i). Also shown, is the (111) pole figure for the transition regions and stagnation point along the longest streamline [114].	38
Figure 2.26: (a) Schematic of the cooling system used, (b) Micro hardness profile measured on cross-sectional planes for the FSP AZ31 alloy [58].	39
Figure 2.27: Schematic showing the grain refinement process of the two pass FSP AZ31 Mg specimens [110].	40

Figure 2.28: (a) Cross-section macrostructure of the processed zone. Contours of temperature (b) and (c), and contours of strain rate (d) and (e) for smooth pin and threaded pin, respectively, at a traveling time of 90 s. The red arrows in (a) and the black dashed lines in (b) through (e) mark the outline of the stir zone [144].	42
Figure 2.29: Simulated temperature distribution 1kg/s of coolant mass flow rate and at a rotational speed of a) 1000, b) 1200 and c) 1750rpm [126].....	43
Figure 2.30: Schematic diagram of twin-roll casting process [149].....	44
Figure 2.31: Schematic of the growth path envelopes for various microstructural changes: (a) growth rate size dependent only, (b) growth rate time dependent only (c) growth rate size and time dependent and (d) crossing growth paths [163].	46
Figure 2.32: Illustration of the procedure for deducing the growth path envelope (c) and nucleation rates (d) from a representation of the evolution of particle size distribution (a) [163].	47
Figure 3.1: a) Schematic and top view of the friction stir processed zone. Region of interest is highlighted. b) Optical micrograph of the edge region showing presence of fine (region 1) and coarse (region 2) grains. Corresponding EBSD, in image quality (IQ) map, shows visible difference in the grain size. c) μ FXrD, in both two and one dimensional representation, for the regions 1 and 2.	58
Figure 3.2: a) EBSD image quality (IQ) map showing co-existence of the fine-coarse interleaved grain structures. b) Fine grains typically had low (<300) IQ. c) They also had higher misorientation: as shown in the map of kernel average misorientation (KAM). d) Average KAM values, and the standard deviations of the KAM distributions, are indicated for the low and high IQ regions. e) Also included are the texture index ($f(g)^2 dg$ where $f(g)$ is the ODF intensity) and average grain size of the respective regions.	60
Figure 3.3: a) Site specific transmission electron microscopy of the low-high IQ or fine-coarse interleaved structure (as in figure 3.2a). Low IQ regions appeared (marked with appropriate straight lines) as possible strain localizations in TEM imaging. It contained grains of few hundred nm. These were almost always surrounded by high angle boundaries (as indicated by transmission Kikuchi diffractions). (b) Pico-hardness of the low and high IQ regions.	61
Figure 4.1: Schematic of (a) FSP (friction stir processing) plate and tool. Schematics of multi-pass FSP under (b) unidirectional, (c) reverse and (d) transverse tool movements.	

In (b)-(d) different locations (p1 to p5) of the FSP (used for characterization) are indicated. (b) also indicates tilt angle θ for morphological representation; and locations AS (advancing side), RS (retreating side)..... 68

Figure 4.2: (a) Optical micrographs at three different locations (p1, p3 and p5) of the second (unidirectional), reverse and transverse pass FSP. Parent structure is also shown. Aspect ratio (Eq. (1)) at different tilt angles (θ : as in figure 4.1b) for different FSP locations for unidirectional (b) first, (c) second, (d) third and (e) fourth pass FSP. Also included are aspect ratios for (f) reverse and (g) transverse tool movements. 70

Figure 4.3: EBSD images, in inverse pole figure (IPF) notation, for (a) parent (prior FSP material), and (b) post-FSP different locations (p1, p3 and p5) after unidirectional second, reverse and transverse pass. 74

Figure 4.4: Average grain size and (b) grain average misorientation (GAM) at different locations (p1 to p5) after different FSP pass schedules (as in figures 4.1(b)-(d)). Respective values of prior-FSP parent material are shown as dotted line. The data from under water unidirectional 1 pass FSP (water quenched) are included in the figures. Error bars represent standard deviations from multiple EBSD scans. 75

Figure 4.5: EBSD IQ (image quality) map showing bimodal grain size distribution (also included) in the processed zone. Transmission electron micrograph showing ultra-fine grains..... 75

Figure 4.6: Experimental X-ray pole figures of (a) prior-FSP material and (b) at different locations (p1-p5, see figure 4.1b) after unidirectional 2nd pass FSP. In (b), (0002), (01 $\bar{1}$ 2), (01 $\bar{1}$ 3), and (11 $\bar{2}$ 4) pole figures are shown. (c) (0002) (or (0001)) X-ray pole figures at different locations (as in figure 4.1b) after 1-4 unidirectional FSP passes. (c) also includes pole figures from unidirectional 1 pass water quenched (process under water) specimen. Pole figure convention and contour levels (and in (a)) were kept identical. (d) Schematic of location dependent shift of the post-FSP pole figures (as in figures 4.6b and 4.6c)..... 80

Figure 4.7: (0002) (or (0001)) X-ray pole figures at different locations (as in figure 4.1c and d) of reverse pass and transverse pass FSP. Pole figure convention and contour levels are same as in figure 4.6a. (b) Texture indices at different locations of the multi-pass and multi-direction FSP. (b) includes data from unidirectional 1 pass water quenched (process under water) specimen. 83

Figure 4.8: Experimental X-ray pole figures (0002) (or (0001)) at cross-sectional locations (see figure 4.1b) locations for unidirectional (a) 1 and (b) 4 pass FSP.....	84
Figure 4.9: Simulated pole figures after imposition of different velocity gradients. The simulations were conducted by considering -1 and +1 values for L_{12} , L_{13} and L_{23} components.	86
Figure 4.10: (a) Simulated pole figures, with an effective von Mises strain ($\bar{\epsilon}$) of 1.0 and appropriate velocity gradients, approximately captured experimental results at extreme FSP locations of p1 and p5 for unidirectional FSP. (b) Simulated pole figures with appropriate velocity gradient matrix for the reverse pass FSP at the locations p1 and p5. (c) Simulated pole figures with appropriate velocity gradient matrix for 51 and 11 locations (as in figure 4.1d) of transverse pass FSP.....	89
Figure 4.11: Texture simulations for effective von Mises strain ($\bar{\epsilon}$) of 0.2, 0.6, 0.8, 1.0, 1.8, 2.4, 3.0 and 8.0.....	90
Figure 4.12: Schematic capturing experimental pole-shifts on the surface (2 ± 2 mm from the top surface: locations p1-p5) and at the cross-section (locations AS1/AS2, C1-C3 and RS1/RS2). Also shown are the velocity gradients imposed on the VPSC simulations reflecting such pole-shifts.	90
Figure 5.1: (a) Schematic of the tool and workpiece used in the FSP. This includes processing direction and tool rotation. The set-up was used to measure z-axis load, spindle torque and temperature profiles (through embedded thermocouple). (b) Cross-sectional schematic of the FSP. Advancing and retreating sides and the position of the embedded k-type thermocouple are shown.	99
Figure 5.2: (a) Schematic of the workpiece in Comsol TM , (b) mesh distribution, (c) tool profile used, and (d) velocity profile and its expression.	102
Figure 5.3: (a) Optical micrographs and (b) EBSD images (in inverse pole figure notation) for the prior and post FSP specimens. These include prior-FSP parent and microstructures at the center of the processed zones. (c) Grain size (from EBSD data) in the respective process zones. Error bars representing standard deviations from multiple EBSD scans. The images and data include FSP under air (PA), water (PW) and liquid nitrogen (PLN).	107
Figure 5.4: Profiles of the experimentally measured (a) z-axis load and (b) spindle torque. These are shown covering tool plunge duration and the start of the translational	

movement of the tool. The figures include FSP under air (PA), water (PW) and liquid nitrogen (PLN).	108
Figure 5.5: (a) Cross-sectional images of the FSP zone and (b) FE simulated temperature profiles. These are shown for FSP under air, water and liquid nitrogen. The tool profile is marked in the respective images.	111
Figure 5.6: (a) Experimental and (b) FE simulated temperature profiles for FSP under air (PA), water (PW) and liquid nitrogen (PLN). In both figures, the peak temperatures are identified.	111
Figure 5.7: (a) Experimental and (b) FE simulated profiles of length versus depth. In (b), respective temperatures (as in figure 5.6b) of 610K, 575K and 543K were used to draw the profiles. (c) Differential temperature ($T - T_{min}$) in the cross-section and also along y-axis (as a function of depth). (d) Change in grain size and temperature between processed zone center and advancing side. These are shown for FSP under air (PA), water (PW) and liquid nitrogen (PLN).....	114
Figure 5.8: Experimental (marked as \circ) true stress versus true strain data of AZ31 compression tests [61]. Data for different temperatures (293K, 473K and 523K) and strain rates (0.001 s^{-1} and 1000 s^{-1}) were ‘fitted’ into constitutive equations of ‘model’.	114
Figure 6.1: Schematic of the twin-roll-cast (TRC) sheet indicating rolling direction (RD) and the area observed through optical microscopy. Montage of optical images and magnified images from middle and top are also included.....	122
Figure 6.2: EBSD images in inverse pole figure (IPF) notation of as received TRC sheet (mid thickness section) and after annealing treatment at different temperature/time	125
Figure 6.3: (a) Mean intercept length and (b) standard deviation (normalized by mean intercept length) versus annealing time. Measurements were obtained from optical micrographs subjected to 300°C and 500°C annealing respectively. Values for the pre-annealing TRC sheet is shown as dotted lines.	126
Figure 6.4: Normalized frequency distribution of mean intercept length after 300°C and 500°C for various annealing times. The insert shows the frequency distribution after 16 hour annealing.....	127
Figure 6.5: Inverse size distribution function having intercept length more than R as a function of R (intercept length) at annealing temperature of (a) 300°C and (b) 500°C.	128

Figure 6.6: Grain evolution envelope at annealing temperature of (a) 300°C and (b) 500°C. Mean intercept length at the given annealing time is also given. 129

Figure 6.7: Variation of area fraction of the grain size bins for (a) as received TRC and for the annealing time of 16 hours for the two annealing temperatures of (b) 300°C and (c) 500°C. 131

Figure 6.8: Variation of Kernel Average Misorientation (KAM) as a function of grain size for (a) as received TRC and for the annealing time of 16 hours for the two annealing temperatures of (b) 300°C and (c) 500°C. The figures distinguish between small and large grains. 132

Figure 6.9 (a) Schematic of the TRC resulting in fine equiaxed grains at the top and bottom of the sheet and bimodal grains at the middle region. (b) shows the microstructural evolution of the middle region after 300°C (16 hours) and 500°C (16 hours) annealing. Actual microstructures, taken at the same magnification, are used to describe the microstructure evolution. 133

List of Tables

Table 2.1: Values of solubility for binary Mg alloys [20]	10
Table 2.2: Mg-Zn crystallographic data for the phases present in the phase diagram of Mg-Zn [22]	12
Table 2.3: Mg-Al crystallographic data for the phases present in the phase diagram of Mg-Al [22]	12
Table 2.4: Probable precipitation processes in magnesium alloys [21].	14
Table 2.5: Characteristic texture components in HCP materials [30].	18
Table 3.1: Chemical composition (in wt% alloying elements) of the AZ31 Magnesium alloy [14].	58
Table 4.1: Experimentally observed R' and ϕ values (figure 4.6) for the pole figures at different locations (see figure 4.1b)	73
Table 4.2: R' and ϕ values of the simulated pole figures (see figure 4.9) with different velocity gradients and an effective von Mises strain ($\bar{\epsilon}$) of 1.0	78
Table 5.1 Chemical composition (in wt% alloying elements) of the friction stir processed AZ31 magnesium alloy	99
Table 5.2: List of symbols and notations	101
Table 6.1: Chemical composition (in wt% alloying elements) of the twin-roll cast AZ31 magnesium alloy	123

Abbreviations

Mg	Magnesium
hcp	Hexagonal Close Packed
fcc	Face Centred Cubic
FSW	Friction Stir welding
FSP	Friction Stir processing
TRC	Twin Roll casting
EBSD	Electron Back-Scatter Diffraction
OIM	Orientation Image Microscopy
TSL	TexSEM Laboratories
XRD	X-Ray Diffraction
GP	Guinier Preston Zones
TEM	Transmission Electron Microscope
FEG	Field Emission Gun
CRSS	Critical Resolved Shear Stress
DC	Direct Chill Casting
RD	Rolling Direction
TD	Transverse Direction
ND	Normal Direction
PF	Pole Figure
ODF	Orientation Distribution Function
IPF	Inverse Pole Figure
GAM	Grain Average Misorientation
KAM	Kernel Average Misorientation
GOS	Grain Orientation Spread
IQ	Image Quality
CI	Confidence Index

Chapter 1

Introduction

1.1 Background

Magnesium alloys are one of the lightest structural alloys available [1]. This makes it an attractive alloy system for applications in automobile and in aerospace [1,2]. However, restricted formability limits its applications [3–6]. Crystallographic orientations strongly affect the plastic deformation and hence the formability in hexagonal metallic materials [7–9]. Ductility and formability of Mg alloys is limited by the availability of only basal slip and $\{10\bar{1}2\}$ twinning systems at the room temperature [4], which also affects the possible modifications in deformation texture under a given strain mode [10–12]. Near basal texture is undesirable for formability of magnesium [7–9]. Conventional thermo-mechanical processing techniques, namely plane strain compression and annealing, do not alter the strong basal texture present [10,11,13–15]. Hence, the need for an alternative processing technique arises. Friction stir processing (FSP) [16], developed on the principles of friction stir welding (FSW) [17], is a new emerging solid state processing technique aimed at modifying the texture, microstructure and consequently improving the properties of the magnesium alloys.

FSP provide localized modification and control of microstructure/texture in near-surface layers by enforcing intense plastic deformation which leads to thermal exposure and intensive material mixing [18,19]. A unique characteristic of FSW/FSP is exceptionally high gradients of temperature, strain, and strain rate. As a result, the obtained microstructures typically show a drastic variation in grain size and morphology, misorientation distribution, and crystallographic texture [20–22].

The underlying mechanism for microstructural evolution, during FSW/FSP is a widely debated topic [21–28]. Severe plastic deformation and static/dynamic aspects of annealing (namely: recovery, recrystallization and grain coarsening [29]) are typically attributed to the formation of equiaxed grains of several microns in size. Also, the crystallographic texture that evolves during FSW contains sharp spatial gradients, and the evolution is argued to be effected by the material flow. The material flow in turn is found to be dictated by the shear deformation along the pin surface during the processing [30,31]. Temperature plays an important role in determining the magnitude and mechanisms of microstructural refinement, and hence, the use of heat sinks [32] can generate sub-micron or even nano-meter sized ultra-fine grains. Modelling of the temperature evolution in various heat sinks for an accurate prediction of microstructural evolution can be useful [33].

Another important issue in magnesium alloys is the commercially viable production of sheets. Sheet metal production using conventional direct chill (DC) casting and hot rolling is complex for Mg alloys. DC cast Mg alloys have poor workability and low heat capacity, often requiring repeated reheating during hot rolling [34]. This restricts commercial Mg alloy sheet production [2]. Twin-roll-casting (TRC) is an emerging manufacturing technology for producing metal sheets, strips or plates [34,35] in which both casting and rolling is done in a single step, hence avoiding subsequent rolling and is touted produce superior properties than the conventional ingot or DC casting. However, the understanding of post-TRC annealing microstructure evolution is limited [36].

Given its significant applications, the fundamental understanding of mechanisms of microstructural and texture evolution during TRC/FSP is rather empirical. The present thesis is an attempt to further refine our understanding of these mechanisms by systematically studying the microstructural origin by capturing the in-situ grain evolution in FSP, prediction of texture evolution using visco-plastic self-consistent (VPSC) modelling, correlation of

microstructural evolution with the thermal history of the FSP zone by finite element modelling and quantitatively analysing the microstructural evolution during annealing in TRC.

1.2 Framework of the thesis

The thesis is divided into chapters consisting of literature review and four pieces of work given in separate chapters.

Chapter 2: Literature review

This chapter reviews the recent and most cited articles on friction stir processing, mainly focussing on mechanisms of microstructural and texture evolution, texture modelling, and finite element modelling. This also includes introduction to another very important processing technique called twin-roll-casting and introduction to grain envelope analysis.

Chapter 3: Microstructural origin of friction stir processed zone in a magnesium alloy

This chapter outlines the study of the microstructural and texture evolution at the edge regions of a friction stir processed (FSP) magnesium alloy AZ31, aimed at explaining the mechanism of the microstructural evolution during FSP. A model of microstructural development through grain boundary sliding of the ultra-fine grains was proposed based on the texture and microstructural observations in the concerned regions.

Chapter 4: Microstructural evolution during multi-pass friction stir processing of magnesium alloy AZ31

This chapter brings out the study on the microstructure and texture developments and also prediction of texture using visco-plastic-self-consistent (VPSC) modelling of commercial magnesium alloy AZ31 being friction stir processed through multi-pass and multi-directional (unidirectional, reverse and transverse tool movements). Location dependent shifting of basal poles along the arc of a hypothetical ellipse was observed, and was captured by the VPSC model. However, the applicability of the model was restricted by the extent of strain imparted. Combinations of ultrafine grain superplasticity followed by grain coarsening were proposed as a possible mechanism for the microstructural evolution during FSP.

Chapter 5: Friction stir processing under different thermal history: experimental observation and numerical simulation

This chapter briefs the study of the effect of various coolant mediums viz. air, liquid nitrogen and water on the microstructural and thermal profiles in the friction stir processed zone. Experimental observations, on the process zone dimensions and temperature profiles, showed significant differences: which highlighted the effect of the thermal history. A numerical simulation was made using multi-physics finite element method. A three-dimensional steady-state coupled laminar fluid flow and heat transfer model was developed, which could capture the experimentally observed process zone dimensions and temperature profiles.

Chapter 6: Study of grain structure evolution during annealing of twin-roll-cast Mg alloy AZ31

This chapter outlines the evolution of microstructure under static annealing at 300°C and 500°C for different times of twin-roll-cast (TRC) magnesium alloy AZ31. Grain path envelope analysis was used for quantitatively analyzing the microstructural evolution. Twin-rolled structure had bimodal grain size which was preserved after annealing at 300°C. However, annealing at 500°C led to a unimodal grain size. A deformation induced recrystallization recovery (DIRR) model was proposed which could explain the observed microstructural features.

Chapter 7: Concluding remarks

Finally, this section outlines the basic findings and the associated conclusions from each of the studies presented in chapters 3-6.

References

1. B. L. Mordike and T. Ebert, *Mater. Sci. Eng. A* **302**, 37 (2001).
2. M. Easton, A. Beer, M. Barnett, C. Davies, G. Dunlop, Y. Durandet, S. Blacket, T. Hilditch, and P. Beggs, *JOM* **60**, 57 (2008).
3. K. U. Kainer, *Magnesium : Proceedings of the 6th International Conference Magnesium Alloys and Their Applications* (2003).
4. S. R. Agnew, J. W. Senn, and J. A. Horton, *JOM* **58**, 62 (2006).
5. S. R. Agnew and O. Duygulu, *Mater. Sci. Forum* **419-422**, 177 (2003).

6. F.-K. Chen and T.-B. Huang, *J. Mater. Process. Technol.* **142**, 643 (2003).
7. Y. Wang and J. Huang, *Mater. Chem. Phys.* **81**, 11 (2003).
8. B. Hutchinson, *Int. J. Mater. Res.* **100**, 556 (2009).
9. W. B. Hutchinson and M. R. Barnett, *Scr. Mater.* **63**, 737 (2010).
10. H. T. Jeong and T. K. Ha, *J. Mater. Process. Technol.* **187-188**, 559 (2007).
11. G. Huang, Q. Liu, L. Wang, R. Xin, X. Chen, and F. Pan, *Trans. Nonferrous Met. Soc. China* **18**, s170 (2008).
12. A. Styczynski, C. Hartig, J. Bohlen, and D. Letzig, *Scr. Mater.* **50**, 943 (2004).
13. M. Wang, R. Xin, B. Wang, and Q. Liu, *Mater. Sci. Eng. A* **528**, 2941 (2011).
14. M. R. Barnett, M. D. Nave, and C. J. Bettles, *Mater. Sci. Eng. A* **386**, 205 (2004).
15. M. D. Nave and M. R. Barnett, *Scr. Mater.* **51**, 881 (2004).
16. Z. Y. Ma, *Metall. Mater. Trans. A* **39**, 642 (2008).
17. R. S. Mishra and Z. Y. Ma, *Mater. Sci. Eng. R Reports* **50**, 1 (2005).
18. W. Yuan and R. S. Mishra, *Mater. Sci. Eng. A* **558**, 716 (2012).
19. Z. Y. Ma, R. S. Mishra, and M. W. Mahoney, *Acta Mater.* **50**, 4419 (2002).
20. W. Woo, H. Choo, M. B. Prime, Z. Feng, and B. Clausen, *Acta Mater.* **56**, 1701 (2008).
21. P. B. Prangnell and C. P. Heason, *Acta Mater.* **53**, 3179 (2005).
22. T. R. McNelley, S. Swaminathan, and J. Q. Su, *Scr. Mater.* **58**, 349 (2008).
23. K. V. Jata and S. L. Semiatin, *Scr. Mater.* **43**, 743 (2000).
24. R. W. Fonda, J. F. Bingert, and K. J. Colligan, *Scr. Mater.* **51**, 243 (2004).
25. J.-Q. Su, T. W. Nelson, and C. J. Sterling, *Mater. Sci. Eng. A* **405**, 277 (2005).
26. K. Oh-ishi, A. P. Zhilyaev, and T. R. Mcnelley, *Metall. Mater. Trans. A* **37A**, 2239 (2006).
27. U. F. H. R. Suhuddin, S. Mironov, Y. S. Sato, H. Kokawa, and C.-W. Lee, *Acta Mater.* **57**, 5406 (2009).
28. J.-Q. Su, T. Nelson, R. Mishra, and M. Mahoney, *Acta Mater.* **51**, 713 (2003).
29. F. J. Humphreys and M. Hatherly, *Recrystallization and Related Annealing Phenomenon*, Second Edition (Elsevier, 2004).
30. D. P. Field, T. W. Nelson, Y. Hovanski, and K. V. Jata, *Metall. Mater. Trans. A* **32**, 2869 (2001).
31. S. H. C. Park, Y. S. Sato, and H. Kokawa, *Metall. Mater. Trans. A* **34**, 987 (2003).
32. C. I. Chang, X. H. Du, and J. C. Huang, *Scr. Mater.* **57**, 209 (2007).
33. S. Aljoaba, O. Dillon, M. Khraisheh, and I. S. Jawahir, *J. Mater. Eng. Perform.* **21**, 1141 (2011).

34. R. V Allen, D. R. East, T. J. Johnson, W. E. Borbidge, and D. Liang, *Magnes. Technol.* **2001** 75 (2001).
35. D. Liang and C. B. Cowley, *JOM* **56**, 26 (2004).
36. Y. Wang, S. B. Kang, and J. Cho, *J. Mater. Process. Technol.* **210**, 1270 (2010).

Chapter 2

Literature Review

2.1 Magnesium: Overview and history

Magnesium is referred [1,2] as the ninth most abundant element in the universe. In terms of relative presence, it is respectively ‘eighth’ in the earth’s crust and fourth most common element on earth (behind iron, oxygen and silicon). Magnesium alloys are known to be one of the lightest structural alloys [2]. This makes it an attractive alloy system for applications in automobile and in aero-space [2,3]. Typical alloying elements are aluminum, zinc, manganese, silicon, copper, rare earth metals and zirconium [4]. Magnesium wrought alloy have tensile strength in the range 180-440 MPa and elongation in the range of 7-40% [4]. Commonly known magnesium wrought alloys are AZ31, AZ61, AZ80, ZK60, HK31, HM21, ZC71 and ZE41 (A=Aluminium, Z=Zinc, K=Zirconium, H=Thorium, M=Manganese, E=Rare earths, C=Copper) [4].

Magnesium was discovered and isolated as a chemical element in 1808 by Sir Humphrey Davey [5]. The production of magnesium was not much till the end of the nineteenth century, but the First World War brought a surge in the demand of magnesium mainly for alloying in aluminum, star lights and tracer bullets [6]. The Second World War increased the production further, with a record drop in the price [6]. Applications were mostly in airplanes and several aspects of armament production [6]. Post second world war, however, the production of magnesium fell [5]. Post world war niche applications involved use in automobile (example: VolkswagenTM Beetle) [5] and structural components of the British Magnox nuclear reactors [7]. These were not sustainable use, as applications got restricted by the performance of the respective alloys.

It took nearly 40 years for the magnesium production to reach to the level of world war II [6]. However, since 1993 the consumption and production of magnesium has risen steadily [6]. It is often forecasted that the magnesium production will increase further mainly driven by its applications in automotive components. Such applications are driven by the need for better fuel economy and lesser emissions [2,4,6]. Magnesium alloys are used and envisaged as candidate material for parts of steering wheels, steering column parts, seats, gearbox housings, gear boxes, air intake systems, stretcher, tank covers and instrument panels [6]. Other usage may range from bicycle frames to screen housing in mobile handset [2,6]. The latter is both lightweight and provides screening against electro-magnetic radiation [2].

The usage of magnesium alloys is still restricted due to its poor formability and low ductility at room temperature [8]. Magnesium has limited slip systems available due to its hexagonal close packed structure to accommodate deformation at room temperature. The critical resolved shear stress (CRSS) for basal planes is significantly lower than the non-basal [9]. This leads to strong near-basal crystallographic texture developments during processing, both deformation and annealing, and corresponding anisotropic properties [10,11]. Easy activation of basal slip system $\{0002\}\langle 11\bar{2}0 \rangle$ is not sufficient to accommodate plastic deformation. Other non-basal slip systems are hence required for improving the room temperature formability [12,13]. Suitable texture and microstructure modifications are thus essential [13] for activation of non-basal slip systems. Much of today's technological research on magnesium alloys is directed in this effort.

Magnesium and its alloys have several advantages. It has high specific strength and good castability [2]. The material is also suitable for high-pressure die-casting [2]. With suitable alloying, magnesium can provide excellent corrosion resistance and resistance to aging [2,6]. The alloys have reasonable electrical and thermal conductivity [2,4]. They are also recyclable. However, there are several ‘limitations’. Other than the critical formability issue (discussed earlier), magnesium alloys offer low elastic modulus and has limited toughness and cold workability [2,4]. Recent interests in magnesium naturally bring research in alloy development [5,14]. For example, magnesium alloys with rare-earth elements (RE) have emerged [11,15]. Rare-earth magnesium alloys have received considerable interest due to their potential for achieving better creep resistance and higher strength. They are one of the lightest structural metallic materials and thus have received considerable attention for advanced applications. The notable examples include alloys based on the Mg–Gd, Mg–Gd–Nd, Mg–Gd–Y and Mg–Y–Nd systems [16–18]. Magnesium alloys can be broadly classified into five groups: (1) Mg–Al–Mn (with or without zinc or silicon), (2) Mg–Zn–Zr (with or without thorium), (3) Mg/RE/Zr (with or without zinc or silver), (4) Mg–Th–Zr (with or without zinc), and (5) Mg–Li–Al [19]. Figure 2.1 shows the schematic of the scheme of the alloying used in case of the magnesium alloys. It is important, at this stage to appreciate the phase transformations occurring in magnesium alloys.

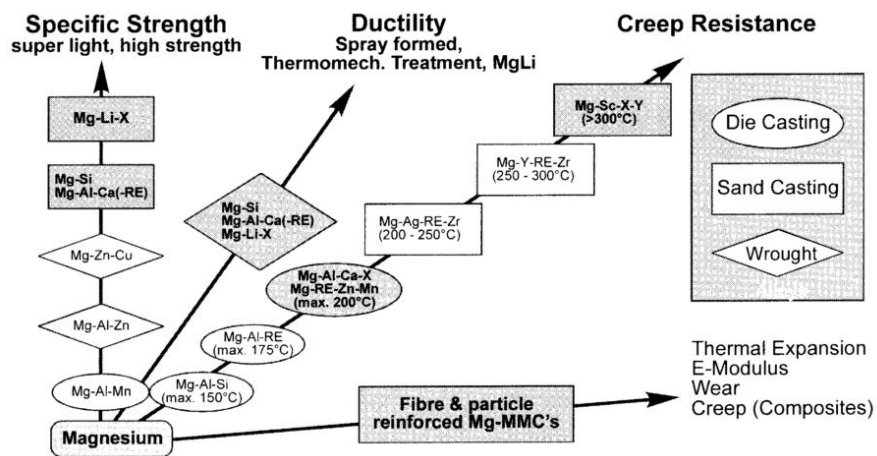


Figure 2.1: Schematic of the direction of alloy development for magnesium alloys [2].

Physical metallurgy of magnesium alloys is dominated by one of the key features that it has hexagonal lattice structure (with $c/a = 1.624$) and its atomic diameter (0.320 nm) is such that it enjoys favorable size factors with many solute elements [5]. Restriction in solid

solubility is often imposed because of differences in valency and because of the chemical affinity of the highly electropositive Mg with elements like tin and silicon, which enables the formation of stable compounds [5]. Example of elements which are widely differing and are present in commercial alloys are aluminum, silver, zinc, yttrium, cerium, zirconium and thorium [20]. Besides the cadmium and magnesium system which form a continuous series of solid solutions, the binary phase diagrams of magnesium rich sections show peritectic and more commonly the eutectic systems [5]. Table 2.1 shows the solubility data for binary magnesium alloys.

Table 2.1: Values of solubility for binary Mg alloys [20]

Element	Solid Solubility		
	At.%	Wt.%	System
Lithium	17.0	5.5	Eutectic
Aluminium	11.8	12.7	Eutectic
Silver	3.8	15.0	Eutectic
Yttrium	3.75	12.5	Eutectic
Zinc	2.4	6.2	Eutectic
Neodymium	~1	~3	Eutectic
Zirconium	1.0	3.8	Peritectic
Manganese	1.0	2.2	Peritectic
Thorium	0.52	4.75	Eutectic
Cerium	0.1	0.5	Eutectic
Cadmium	100	100	Complete SS
Indium	19.4	53.2	Peritectic
Thallium	15.4	60.5	Eutectic
Scandium	~15	~24.5	Peritectic
Lead	7.75	41.9	Eutectic
Thulium	6.3	31.8	Eutectic
Terbium	4.6	24.0	Eutectic
Tin	3.35	14.5	Eutectic
Gallium	3.1	8.4	Eutectic
Ytterbium	1.2	8.0	Eutectic
Bismuth	1.1	8.9	Eutectic
Calcium	0.82	1.35	Eutectic
Samarium	~1	~6.4	Eutectic
Gold	0.1	0.8	Eutectic
Titanium	0.1	0.2	Peritectic

Of the varying range combinations of intermetallic compounds, the frequent structures are [5]:

Table 2.2: Mg-Zn crystallographic data for the phases present in the phase diagram of Mg-Zn [22]

Phase	Composition wt% Zn	Space Group
(Mg)	0 to 6.2	$P6_3/mmc$
(Mg ₇ Zn ₃)	53.6	$Immm$
(MgZn)	74.0	...
(Mg ₂ Zn ₃)	80.1	$C2/m$
(Mg Zn ₂)	84 to 84.6	$P6_3/mmc$
Mg ₂ Zn ₁₁	93.7	$Pm\bar{3}$
(Zn)	99.9 to 100	$P6_3/mmc$

Table 2.3: Mg-Al crystallographic data for the phases present in the phase diagram of Mg-Al [22]

Phase	Composition wt% Zn	Space Group
(Al)	0 to 17.1	$Fm\bar{3}m$
β (Al ₃ Mg ₂)	36.1 to 37.8	$Fd\bar{3}m$
R	39	$R\bar{3}$
γ (Al ₁₂ Mg ₁₇)	42 to 58.0	$I\bar{4}3m$
(Mg)	87.1 to 100	$P6_3/mmc$

2.2 Magnesium alloys

2.2.1 Alloys based on Mg-Al system

The binary system of Mg-Al formed the basis for early magnesium casting alloys. At a temperature of 437°C, aluminium exhibits the maximum solid solubility (12.7%), which decreases to near 2% at room temperature. The formation of the β phase Mg₁₇Al₁₂ in the as cast condition, usually occurs around the grain boundaries. Solution treatment or annealing at temperatures of ~430°C usually leads to the dissolution of the all or a part of the β phase.

Subsequent quenching and aging can impart significant precipitation hardening. However, aging can result in transformation of the supersaturated solid solution directly to a coarsely dispersed, equilibrium precipitate β without the appearance of Guinier-Preston (GP) zones or intermediate precipitates. Alloys of the Mg-Al system are generally used in the as cast condition given its relatively poor response to ageing [20]. The addition of 1% Ca improves creep strength of Mg-Al alloys [23] but makes them susceptible to hot cracking. Creep properties are also improved by decreasing the aluminium content and introducing silicon [24–26].

2.2.2 Alloys based on Mg-Zn system

Age hardening is usually shown by binary Mg-Zn alloys. However, they form coherent GP zones and semi-coherent intermediate precipitates (see table 2.4). These alloys are generally not amenable to grain refinement. They are not used for commercial applications given their susceptibility to micro-porosity [20].

2.2.3 Alloys based on Mg-RE system

Magnesium forms a solid solution with a large number of rare earth elements. Simple eutectic is shown by the magnesium rich regions of the respective binary systems. The alloys have cored α grains surrounded by grain boundary networks, in the as cast condition. As the result of aging, precipitation occurs within the grains. These alloys usually show good creep resistance which can be attributed to the strengthening because of the precipitate formation and also due to the presence of grain boundary phases which inhibits grain boundary sliding [5,20,27].

2.2.4 Wrought Mg based alloys

Wrought alloys are mainly manufactured by extrusion, rolling and press forging at elevated temperatures in the range of 300-500°C. Broadly, wrought alloys can be divided into two groups depending on the presence or absence of zirconium [20]. AZ31 (Mg-3Al-1Zn-

0.3Mn) is a commonly known and widely used sheet and plate alloy. It has good combination of ductility, strength and also corrosion resistance [5]. In terms of higher strength alloys such as ZK61 (Mg-6Zn-0.7Zr), AZ81 (Mg-8Al-1Zn-0.7Mn) and ZCM711 (Mg-6.5Zn-1.25Cu-0.75Mn) are available, which have strength/weight ratio comparable to the strong wrought aluminium alloys. ZM21 (Mg-2Zn-1Mn) is known to be the lowest cost extrusion alloy of magnesium as it can be extruded at high speeds [4].

Table 2.4: Probable precipitation processes in magnesium alloys [21].

Mg-Al	SSSS	→	β ($Mg_{17}Al_{12}$) bcc (143m, $a = 1.06$ nm); (0001) _a plate/lath
Mg-Al-Ca	SSSS	→	ordered G.P. zones → C15 (Al_2Ca) hcp $a = 0.556$ nm monolayer (0001) _a disc fcc, Fd3m $a = 0.802$ nm (0001) _a plate
Mg-Zn	SSSS	→	G.P. zones → β'_1 (Mg_2Zn_7) monoclinic, B/2m $a = 2.60$ nm $b = 1.43$ nm $c = 0.52$ nm $\gamma = 102.5^\circ$ [0001] _a rod → β'_2 ($MgZn_2$) hcp, P6 ₃ /mmc $a = 0.52$ nm $c = 0.86$ nm (0001) _a plate → β (MgZn) monoclinic $a = 1.61$ nm $b = 2.58$ nm $c = 0.88$ nm $\beta = 112.4^\circ$
Mg-Zn-Al [§]	SSSS	→	G.P. zones → i → Φ and/or T icosahedral or approximant diamond shape Φ : orthorhombic, Pbcn $a = 0.90$ nm $b = 1.70$ nm $c = 1.97$ nm (0001) _a lath T: bcc, Im $\bar{3}$ $a = 1.40$ nm
Mg-Sn(-Zn)	SSSS	→	β (Mg_5Sn) fcc (Fm $\bar{3}m$, $a = 0.68$ nm), (0001) _a and $\{11\bar{2}2\}$ _a plate/lath, [0001] _a rod and polygon
Mg-Ca-Zn	SSSS	→	ordered G.P. zones → η' ($MgCaZn$) → η ($Mg_3(Ca,Zn)$) hcp, P6 ₃ /mmc $a = 0.556$ nm monolayer (0001) _a disc hcp, P6 ₃ /mmc $a = 0.56$ nm $c = 1.04$ nm (0001) _a plate hcp, P6 ₃ /mmc $a = 0.62$ nm $c = 1.01$ nm (0001) _a plate
Mg-Nd	SSSS	→	ordered G.P. zones → β^* (Mg_3Nd) → β' (Mg_7Nd) → β_1 (Mg_5Nd) → β ($Mg_{12}Nd$) zig-zag shape $d = 0.37$ nm* hcp, D0 ₁₉ $a = 0.64$ nm $c = 0.52$ nm hexagonal prism orthorhombic $a = 0.64$ nm $b = 1.14$ nm $c = 0.52$ nm lenticular shape fcc, Fm $\bar{3}m$ $a = 0.74$ nm $\{10\bar{1}0\}$ _a plate tetragonal, I4/mmm $a = 1.03$ nm $c = 0.59$ nm [0001] _a rod
Mg-Nd-Zn	SSSS	→	ordered G.P. zones → γ^* ($Mg_5(Nd,Zn)$) → γ (possibly $Mg_5(Nd,Zn)$) hcp $a = 0.556$ nm monolayer (0001) _a disc hcp, P6 $\bar{2}m$ $a = 0.55$ nm $c = 0.52$ nm (0001) _a plate fcc, possibly Fm $\bar{3}m$ $a = 0.70$ nm plate on irrational plane β_2 ($Mg_{11}Nd_5$) tetragonal, I4/m $a = 1.47$ nm $c = 1.04$ nm
Mg-Gd(-Y)	SSSS	→	ordered G.P. zones → β^* (Mg_5Gd) → β' (Mg_7Gd) → β_1 (Mg_5Gd) → β (Mg_5Gd) zig-zag shape $d = 0.37$ nm* hcp, D0 ₁₉ $a = 0.64$ nm $c = 0.52$ nm hexagonal prism orthorhombic $a = 0.65$ nm $b = 2.27$ nm $c = 0.52$ nm lenticular shape fcc, Fm $\bar{3}m$ $a = 0.73$ nm $\{10\bar{1}0\}$ _a plate fcc, Fm $\bar{3}m$ $a = 2.23$ nm $\{10\bar{1}0\}$ _a plate
Mg-Y	SSSS	→	β' (Mg_7Y) → β ($Mg_{24}Y_5$) orthorhombic $a = 0.65$ nm $b = 2.27$ nm $c = 0.52$ nm globular shape bcc, I43m $a = 1.13$ nm $\{10\bar{1}0\}$ _a or $\{31\bar{4}0\}$ _a plate
Mg-Y-Nd	SSSS	→	ordered G.P. zones → β^* (Mg_5Nd) → β' ($Mg_{12}YNd$) → β_1 ($Mg_5(Nd,Y)$) → β ($Mg_{14}Nd_2Y$) zig-zag shape $d = 0.37$ nm* hcp, D0 ₁₉ $a = 0.64$ nm $c = 0.52$ nm hexagonal prism orthorhombic $a = 0.64$ nm $b = 2.24$ nm $c = 0.52$ nm globular shape fcc, Fm $\bar{3}m$ $a = 0.74$ nm $\{10\bar{1}0\}$ _a plate fcc, Fm $\bar{3}m$ $a = 2.20$ nm $\{10\bar{1}0\}$ _a plate
Mg-Gd-Zn [#]	SSSS	→	γ^* ($Mg_{70}Gd_{15}Zn_{15}$) → γ' ($MgGdZn$) → γ ($Mg_{12}GdZn$) ordered hcp, P6 $\bar{2}m$ $a = 0.56$ nm $c = 0.44$ nm (0001) _a plate hcp, P3m1 $a = 0.32$ nm $b = 0.78$ nm (0001) _a plate ordered hcp, 14H $a = 1.11$ nm $c = 3.65$ nm (0001) _a plate
Mg-Y-Zn	SSSS	→	I_2 stacking fault (0001) _a plane → γ' ($MgYZn$) → γ ($Mg_{12}YZn$) hcp, P3m1 $a = 0.32$ nm $c = 0.78$ nm (0001) _a plate ordered hcp, 14H $a = 1.11$ nm $c = 3.65$ nm (0001) _a plate
Mg-Y-Ag-Zn	SSSS	→	G.P. zones → γ^* → γ' → $\gamma + \delta$ monolayer (0001) _a disc ordered hcp, P6 $\bar{2}m$ $a = 0.56$ nm $c = 0.45$ nm (0001) _a plate hcp, P3m1 $a = 0.32$ nm $c = 0.78$ nm (0001) _a plate γ : ordered hcp, 14H $a = 1.11$ nm $c = 3.65$ nm (0001) _a plate δ : fcc, Fd $\bar{3}m$ $a = 1.59$ nm

[§]Precipitation process is not well studied; * d is separation distance of columns of RE atoms; [#]low Gd:Zn weight ratio and low Gd content.

Mg-Li wrought alloys have gained considerable interest owing to its applications in lightweight materials. Solid solubility of lithium in magnesium is high (see table 2.1). Extensive cold formability is possible in binary alloys with Li percentage greater than 11 owing to the desirable bcc structure [5]. Age hardening is also prominent in these alloys. They also tend to overage and soften at low temperatures due to the high mobility of lithium atoms and vacancies. Addition of aluminium can achieve greater stability in such alloys for example LA141 (Mg-14Li-1Al) [2]. These alloys are mostly used for advanced applications in space crafts and body armours.

2.3 Crystallographic orientation and its representation

Orientation of a grain or crystallite is defined as the minimum rotation required to coincide the crystal coordinate axes with the global coordinate axes [28]. The convention for deciding global coordinate system varies with the processing route. For example, in case of a rolled sheet, rolling direction (RD), transverse direction (TD) and normal direction (ND) constitute the global system. There are three different ways of representing an orientation:

1. Euler Angles: $(\varphi_1, \varphi, \varphi_2)$
2. Miller Indices: $(hkl)\langle uvw \rangle$
3. Axis-Angle Pair: $\langle uvw \rangle \theta$

Euler angles are achieved in three rotations $(\varphi_1, \varphi, \varphi_2)$. In Bunge notation, the first rotation φ_1 is around the Z-axis or ND, φ being a rotation around the transformed X-axis, while φ_2 is defined by a rotation around the modified Z-axis (see figure 2.3) [28,29]. The Euler angles $(\varphi_1, \varphi, \varphi_2)$ are typically used as an orientation parameter. The orientation space is cyclic, self-contained and completely described by:

$$0 \leq \varphi_1 < 2\pi, 0 \leq \varphi < \pi, 0 \leq \varphi_2 < 2\pi$$

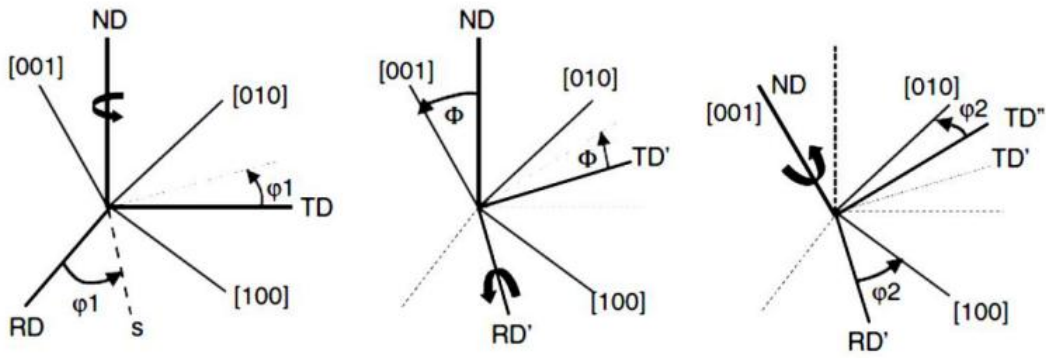


Figure 2.3: Schematic representation of Euler angles using Bunge notation [29].

Miller indices represent the orientation in terms of the combination of a specific crystallographic plane and a crystallographic direction in it. The third way of representing an orientation is to define an axis $\langle uvw \rangle$ around which the said crystallite has to rotate at a specified angle, say θ , so as to coincide with the global reference system.

Representation of crystallographic texture started in form of pole figures [28,29]. Pole figures are obtained by stereographic projection of specific plane normal. It essentially shows an intensity distribution of such poles with respect to the global reference systems such as RD, TD and ND. Though this is an important way of representing texture, it only gives a qualitative idea about the orientation distribution. The other way of representation is inverse pole figure (IPF). IPF is angular distribution of a chosen specimen direction with respect to the crystal coordinate system. In an inverse pole figure, the axes of the projection sphere are aligned with crystal directions. The inverse pole figure can help in visualizing the certain type (for example: axi-symmetric texture of a drawn wire) of textures [28–30].

A more complete and accurate description of the texture distribution is possible using ODF (orientation distribution function) [28]. An ODF is derived from four or five pole figure data or from discrete/local orientation measurements using mathematical techniques such as series expansion, etc. The ODF is generally defined as the volume fraction of grains with a certain orientation \mathbf{g} .

$$\frac{dV_g}{V} = f(\mathbf{g})d\mathbf{g} \quad (1)$$

where V is the sample volume and dV_g the volume of all crystallites with the orientation \mathbf{g} in the angular spread $d\mathbf{g}$. The orientation \mathbf{g} is usually identified using the three Euler angles.

The Euler angles is hence described as the transition from the sample reference frame to the crystallographic reference frame for each individual grains. The distribution of the large set of Euler angles from the grains in a polycrystal can be described by the ODF [30].

Individual single crystal properties and the parameters characterizing the polycrystalline state decide the properties of the crystalline materials. Crystallographic texture (occurrence of preferred orientations of the grains) plays an important role in determining the mechanical and physical properties [28,29]. Crystalline materials can undergo texture evolution during processes such as casting, thermal mechanical processing, deformation, welding as well as heat treatment. Materials behave isotropically if all possible orientations occur with equal frequency and hence orientation dependence on properties will vanish. If such a case arises, where all crystals are aligned similarly, the polycrystalline material behaves as a single crystal material. One example of this case is the occurrence of “Goss $\{110\}\langle 001 \rangle$ texture” in transformer steel [30]. More commonly, preferred orientation is classified as “deformation texture” and “recrystallization or annealing texture”. As this thesis deals with textures in hexagonal magnesium (Mg), subsequent paragraphs introduce textures in hexagonal materials.

2.4 Texture analysis in hexagonal materials

Textures in hexagonal metallic materials have gained interest in the recent past [10,31–34]. The interests are primarily focused on Zirconium, Titanium and Magnesium. It needs to be noted that hexagonal metallic materials are mechanistically different from the relatively well-understood cubic metals. The former typically have lesser number of slip systems available and also has relatively easy activation of twinning [30,35,36]. Texture in hexagonal materials is usually represented by $\{hkil\}\langle uvw \rangle$ which indicate that the $\{hkil\}$ planes of the concerned grains lie parallel to the sheet plane, whereas their $\langle uvw \rangle$ direction points parallel to the rolling direction [28]. The characteristic texture in HCP materials, in the Bunge convention is shown in table 2.5.

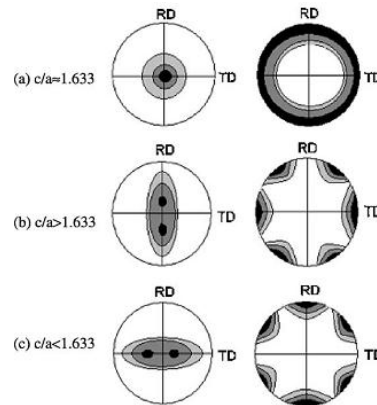
Table 2.5: Characteristic texture components in HCP materials [30].

Texture characteristics in HCP materials (Bunge system)

Texture component	Constant ϕ_2 ($^\circ$)	ϕ ($^\circ$)	ϕ_1 ($^\circ$)
Basal fiber $\{0001\}$	0–60	0	0–90
Basal fiber $\{hkil\}$	$[2\bar{1}\bar{1}0] [hki0]$	$[0001] [hki\bar{l}]$	0–90
$\{0001\}(10\bar{1}0)$	0/60	0	0.60/0.60
$\{0001\}(11\bar{2}0)$	$\phi_2 + \phi_1 = 60$	0	$\phi_2 + \phi_1 = 60$
	0/30	0	0.90/0.60
Fiber $\{10\bar{1}0\}$	$\phi_2 + \phi_1 = 30$	0	$\phi_2 + \phi_1 = 30$
	30	90	0–90
$\{10\bar{1}0\}(0001)$	30	90	90
$\{10\bar{1}0\}(11\bar{2}0)$	30	90	0
Fiber $\{11\bar{2}0\}$	0/60	90	0–90
$\{11\bar{2}0\}(0001)$	0/60	90	90
$\{11\bar{2}0\}(10\bar{1}0)$	0/60	90	0

2.4.1 Texture components in hexagonal materials

Based on the c/a ratio, rolling textures in hexagonal metallic materials can be categorized into three groups [30]. This is shown in figure 2.4. For ideal c/a ratio (≈ 1.633) (example: Mg, Co) basal poles concentrate in symmetry around ND. $[10\bar{1}0]$ and $[11\bar{2}0]$ directions are randomly distributed around the basal plane. For c/a ratio > 1.633 (example: Zn, Cd) the position of the maximum basal pole intensity is tilted by ± 15 to 25° from ND (normal direction) towards the RD (rolling direction), with $[11\bar{2}0]$ direction aligned towards RD. For c/a ratio < 1.633 (example: Zr, Ti, Hf, Be) the position of the maximum basal pole intensity is tilted to ± 20 to 40° from ND towards TD, $[10\bar{1}0]$ direction being aligned toward the rolling direction.



(0002) pole figure (10 $\bar{1}0$) pole figure

Figure 2.4: Simulated rolling texture ((0002) and (10 $\bar{1}0$) poles) in hexagonal closed packed metals with c/a ratio: (a) ~ 1.633 , (b) > 1.633 and (c) < 1.633 [30].

Further, ideal pole figures for some important texture components of hexagonal magnesium are summarized in figure 2.5.

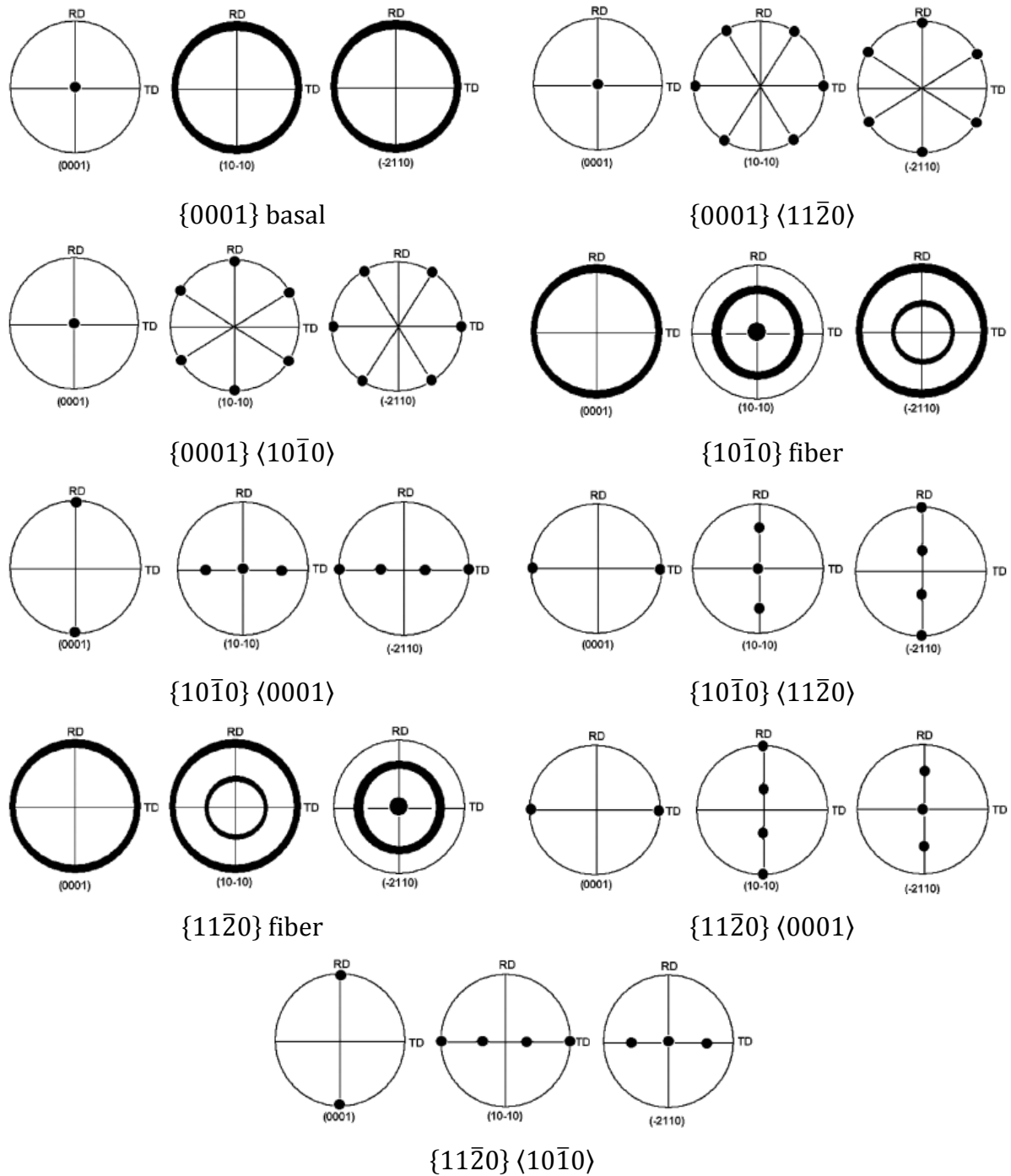


Figure 2.5: Ideal pole figures of some important texture components for Mg ($c/a = 1.624$) [30].

Often a family of orientations is represented as fiber texture [28,30,37]. For example, a combination of a set of same crystallographic plane with all possible crystallographic

directions can be represented as $\{0001\}$ fiber and $\{hkil\}$ fiber texture, see figure 2.6. Both deformation and recrystallization textures may exhibit such fiber textures.

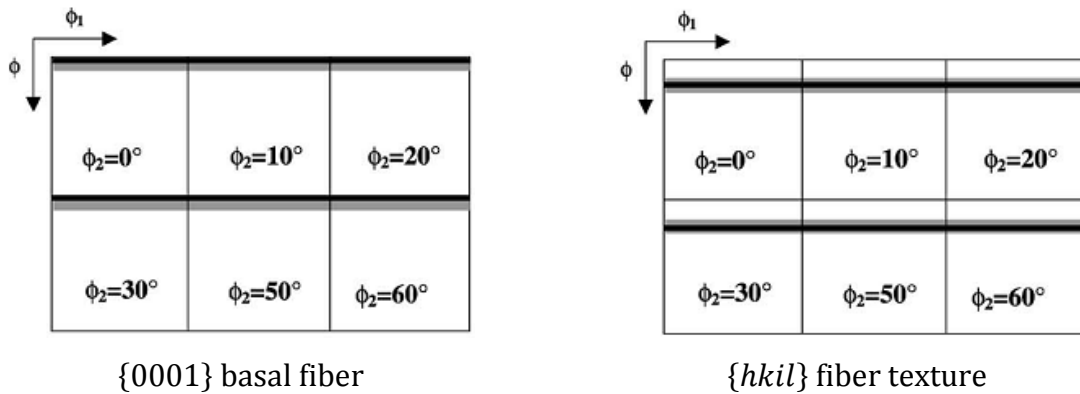


Figure 2.6: Ideal ODF positions for some low index orientation of the hexagonal closed pack crystalline structure [30].

For this thesis, the important textures are the so-called shear texture [38–41]. They are defined in terms of the crystallographic plane $\{hkl\}$ and direction $\langle uvw \rangle$, aligned with the shear plane and shear direction. In a friction stir welding (introduced later) the shear plane and direction are not simply related to the sample geometry, but might be expected to be approximately parallel to the pin surface, or nugget flow lines. Typical shear texture observed in a processed zone in a friction stir welded AZ61 magnesium alloy at different locations is shown in figure 2.7. FSP texture developments in magnesium are discussed in further details latter in this literature review.

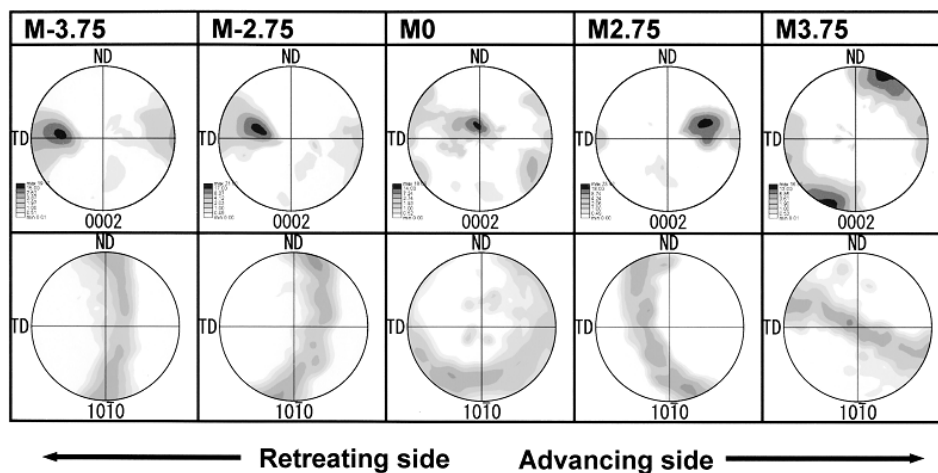


Figure 2.7: $\langle 0002 \rangle$ and $\langle 10\bar{1}0 \rangle$ pole figures at various locations at the advancing and retreating side of a friction stir welded magnesium alloy AZ61 [38].

2.5 Introduction to friction stir welding/processing

Friction stir welding (FSW) is a solid-state joining technique invented at The Welding Institute (TWI), UK in 1991 [42,43]. FSW is a severe plastic deformation technique which involves a non-consumable rotating tool consisting of a specially designed pin and a shoulder [42,44–46], which is being inserted between the edges of the plates to be welded till the point when the shoulder touches the workpiece. The tool is then traversed along the joint with a constant translational speed and a very high rotational speed. Friction heating plasticize the material [47] and leads to its movement from the front to the rear side, thus producing a sound solid state joint. The schematic of the FSW assembly is shown in figure 2.8.

FSW is usually said to be a major development in the field of metal joining in the past decade. FSW is a “green” technology since it is environment friendly and energy efficient. It can be used to join high strength aerospace alloys and other metallic alloys that are hard to weld using the conventional welding techniques [43,48–52].

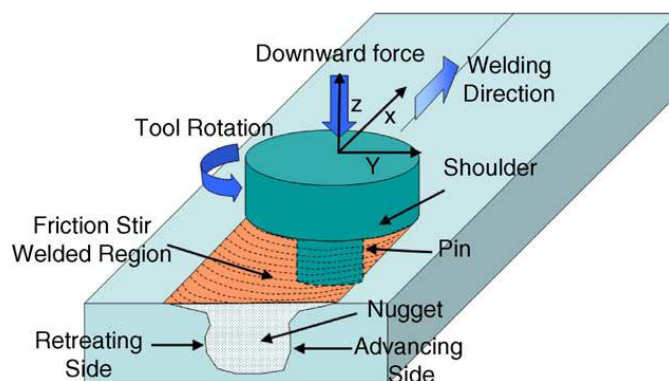


Figure 2.8: Schematic drawing of FSW [42]

Recently, friction stir processing (FSP) [53] based on the basic principles of FSW [42,43] was developed for microstructural modification. In contrast to FSW, FSP involves a rotating tool with pin and shoulder which is inserted in a single piece of material, for local modification in microstructure which enables specific property enhancement. Moreover, FSP can be used for fabrication of surface composites and homogenization of powder metallurgy (PM) aluminum alloys, metal matrix composites, and cast aluminum alloys [54]. FSW/P

technique can be helpful in making magnesium alloys more viable for the industrial applications [1,2,5,55].

During the process, the tool rotates as well as translates, which forces the surrounding material to flow around the tool. This movement fills the cavity in the rear of the tool. The material undergoes severe level of plastic deformation and also thermal exposure. This leads to development of very fine grained microstructure [56–60] and significant texture changes [38–40,54,61–63] in the weld or stir zone. As FSW/FSP does not involve any solidification, the solidification problems associated with conventional welding techniques (eg. fusion welding, TIG welding etc.) are not seen and this helps in better retention of baseline mechanical properties.

Various processing techniques such as thermo-mechanical treatment (TMT), torsion under compression, multi-axial alternative forging (MAF), equal channel angular pressing (ECAP) and accumulative roll bonding (ARB) can be done for severe plastic deformation of materials for enhancing mechanical properties [64–66]. Compared to other techniques, FSP has many advantages. First, the source of heat during FSP is friction and plastic deformation, which means that, it is an energy efficient and green technique without producing any radiation, deleterious gas and noise. Second, FSP is a solid state, short route processing technique which can achieve microstructural refinement, densification, and homogeneity [56,67]. Third, microstructure and hence the mechanical properties of the processed region can be controlled accurately by optimizing the FSP parameters, tool design and rate of cooling/heating [44,58,68,69]. Fourth, depth of processed zone can be controlled in FSP which is difficult to achieve in other metal working techniques [70]. Fifth, FSP do not cause any change in the size or the shape of the processed components [53].

FSP is now emerging as a very effective processing technique which can provide localized modification of microstructure and properties. In a short time since its invention, many applications have emerged in the field of processing, fabrication and synthesis of metallic materials.

2.5.1 Microstructural evolution during friction stir processing

The softening or the restoration mechanisms (both static and dynamic) during thermomechanical processing has been widely studied [37,71–73]. However, the recent advances in the production of ultrafine grains through severe plastic deformation have led to renewed interests on this topic [74–77]. This is important as our understanding of both deformation and associated softening/restoration remains largely empirical under complex strain modes. In this section, relevant knowledge on FSW/FSP microstructural evolution has been collated. This is important, as the focus of the thesis (especially the third chapter) is on the microstructural evolution during FSP of magnesium. In this section knowledge on the subject [41,56,78–83] is collated, in an effort to identify possible ‘gaps’ in our present understanding.

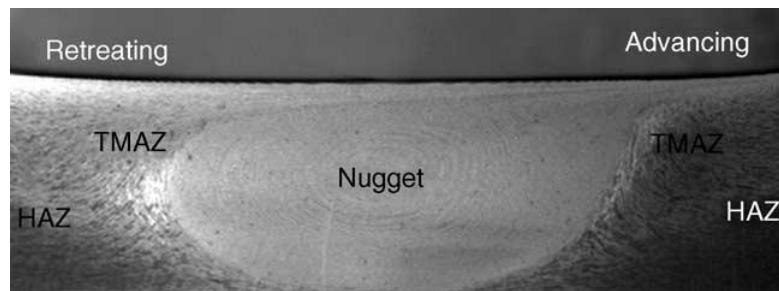


Figure 2.9: Cross-sectional profile showing the different zone in FSP of 7075Al-T651 [70].

As shown in figure 2.9, typical FSW/FSP microstructures have three distinct regions [53,70,84–87]. First is the nugget zone or the stir zone (SZ), which is strongly affected by the rotation of the tool. This region experiences large plastic strains (10^1 to 10^2). Peak temperatures are usually highest (0.6 to 0.95 T_M , T_M being the homologous temperature). The nugget temperature and temperature profiles are affected by the material properties, processing conditions and tool design. The upper portion of the nugget experiences deformation as well as heating from the tool pin and the shoulder. The second region is the thermo-mechanically affected zone (TMAZ). This is subjected to lesser strain and strain rates and consequently lower temperatures. This region usually has the patterns of grain distortion, indicating shearing through plastic flow [83]. The latter is shown in figure 2.10(a). Fragmentation and formation of fine and equiaxed grains near the interface of SZ and TMAZ

occur due to the grain distortion [86,88,89]. The last and the third region is the heat affected zone. This zone only experience thermal cycle and no deformation.

Two parameters are really significant for FSW/FSP: they are tool rotation rate and tool transverse speed [42]. The effect of the grain size in the stir zone as the function of tool rotation speed is shown in figure 2.10(b) [88]. The rotation of tool results in stirring or mixing, while translation enables material movement from the front to the back of the pin. Higher tool rotation generates higher temperatures from frictional heating and more intense stirring and mixing. However, heating may not increase monotonically with increase in tool rotation speed as the coefficient of friction may vary at the interface with tool rotation rate.

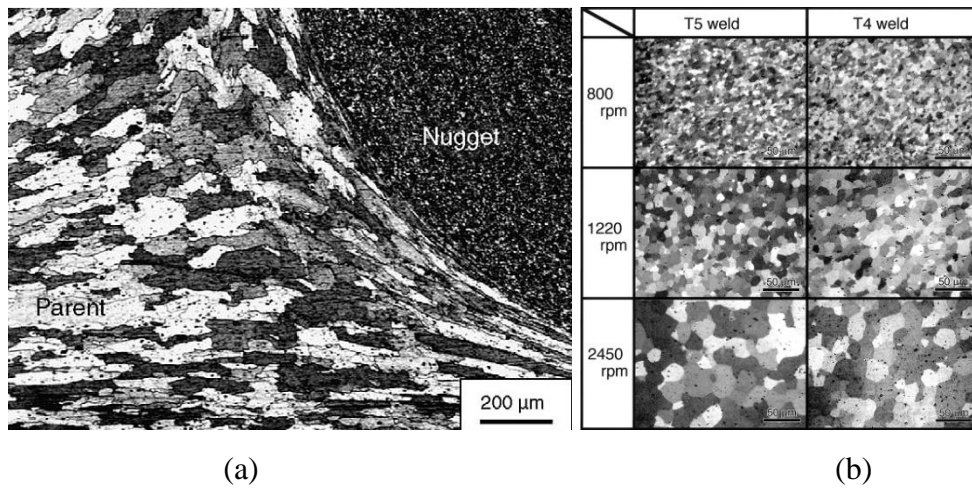


Figure 2.10: a) Microstructural evolution in the thermo-mechanically affected zone in FSP 7075Al [83] and (b) optical microstructures in the stir zones in the welds of Al alloys 6063-T5 and T4 [88].

Degree of deformation and peak temperatures during the thermal cycle of FSW/FSP increase for a higher tool rotation rate or a higher ratio of tool rotation speed/transverse speed [90]. Given the basics of recrystallization, the increase in deformation during the processing will result in reduction in the recrystallized grain size. However, the increase of peak temperature will lead to formation of coarser recrystallized grains and may also result in grain growth. Figure 2.11 shows the peak temperatures achieved at various positions with increasing rotation speed and also for various alloy systems [42].

Apart from tool rotation and translational, tool tilt or the angle of spindle with respect to the workpiece surface is also an important process parameter. A suitable tilt of the spindle towards trailing direction ensures that the shoulder of the tool holds the stirred material by threaded pin and move material efficiently from the front to the back of the pin [42,52,53].

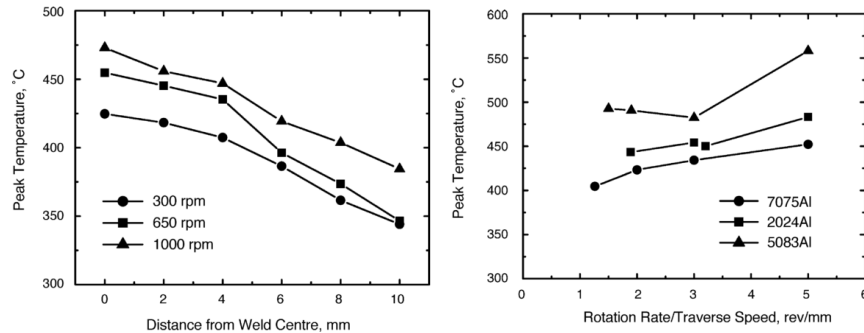


Figure 2.11: Effect of FSP parameters and alloy systems on peak temperature [42].

The majority of the microstructural characterization work has been primarily done while focusing on the characterization of the final microstructure when the tool has passed the concerned regions. In other words, the material underwent thermal and deformation cycle during the processing and has also seen the post-FSP cooling. Relatively ‘limited’ research has been done on capturing the actual microstructure during the processing which can explain the basic microstructural mechanisms operating during FSW/FSP [41,81,91]. These are summarized in the paragraphs below.

Fonda *et al.* [41] used the stop-action friction stir welding of Al-Li 2195 alloy to freeze the in-situ deformation field which surrounds the FSW tool. Analysis of the freeze in structure reveals interesting details on grain structure evolution during the processing.

Figure 2.12 shows the schematic of the processing and the section of the plane that was cut to characterize the microstructural evolution. It was observed that the bands of refined grains developed ahead of the fully refined regions, which reflected varying relative stabilities of the original grain orientation to the applied deformation. Simple shear deformation field led to the formation of fine sub-grains, in which greater misorientation eventually developed to produce the refined grains observed adjacent to the tool. These regions displayed typical fcc shear texture. The primary mechanism of grain fragmentation appeared to be subdivision

induced by the deformation and dynamic recovery, without the occurrence of dynamic recrystallization.

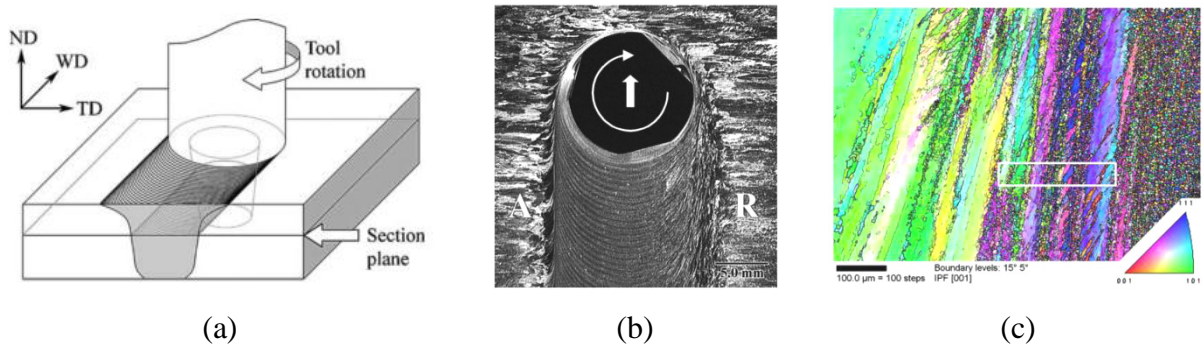


Figure 2.12: (a) Schematic of the stop-action friction stir weld. The sample axis (plate-normal direction (ND), welding direction (WD) and transverse direction (TD)) are also shown. b) Plane view of the section. c) Grain evolution ahead of the tool on the advancing side of the tool [41].

Another interesting piece of work by Prangnell and Heason [91] showed that the equiaxed grain structure typical of FSP/FSW develops by first shearing of the original coarse grain structure to thin circumferential bands. Then, the equiaxed grains develop at the high angle boundaries between such layers. Deformation structures were ‘frozen’ by stopping the tool and immediately quenching the work piece (see figure 2.13). The ‘frozen’ weld keyhole was sectioned through, which allowed the microstructure development to be observed directly which leads to the formation of the ultrafine-grained nugget zone. It was shown that the grain fragmentation process was driven by the grain subdivision at the colder periphery of the deformation zone of the tool and the geometric effects of strain. This led to the reduction of the overall high angle boundary spacing with the increase in deformation. Moreover, thermally activated high angle grain boundary migration also plays an important role. The grain structure in the stir zone was found to be equiaxed and it tends to coarsen in the thermal wake of the tool (see figure 2.14).

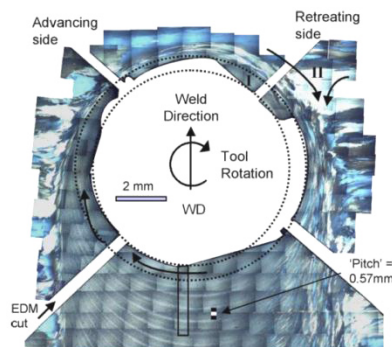


Figure 2.13: Top view of the stop action technique used to freeze the structure [91].

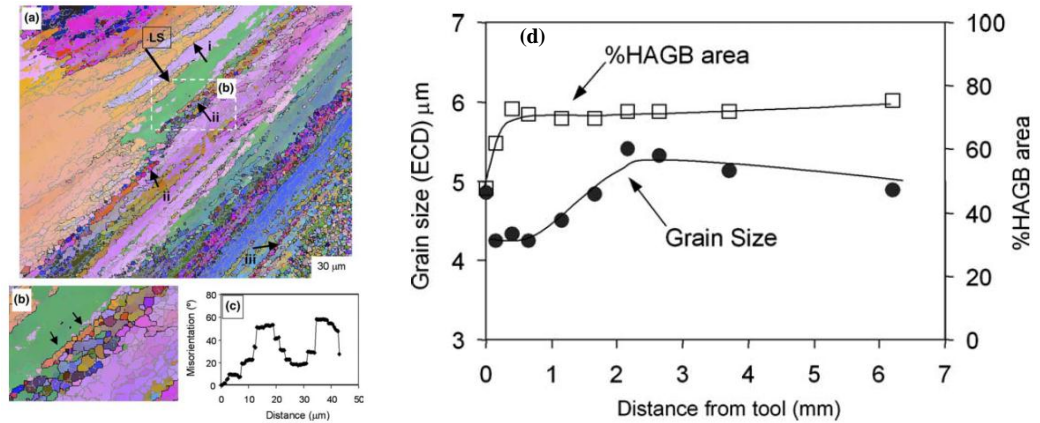


Figure 2.14: (a) EBSD map from ahead of the tool on the advancing side of the weld, showing a grain splitting into deformation bands with two alternating orientations (c) Misorientation profile. (d) Average grain size as a function of distance behind the tool taken along weld centerline [91].

Further Su *et al.*[81] investigated the microstructural evolution in 7075-T6 Al plate by immediately quenching the workpiece using methanol and dry ice, after the rotating tool was quickly lifted. The microstructures were further analyzed using Transmission Electron Microscopy (TEM). The schematic of the positions where TEM samples were prepared and very fine grains formed in the zone is shown in figure 2.15. TEM micrographs at various regions are shown in figure 2.16.

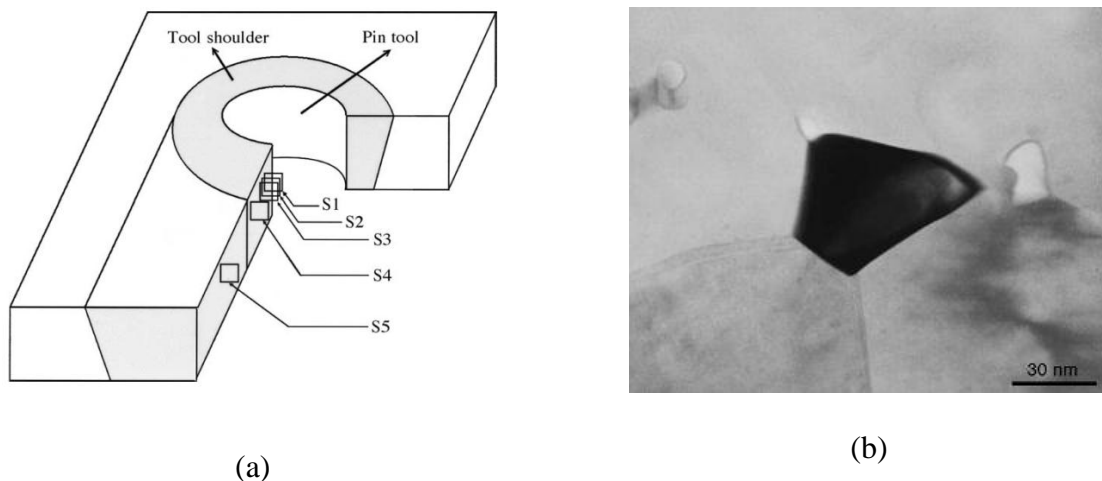


Figure 2.15: a) Schematic of the regions where TEM samples were prepared, b) formation of very fine grains in the processed region [81].

It was observed that the microstructural evolution during FSW/FSP of Al alloys results from various mechanisms operating during the process, which include discontinuous dynamic recrystallization, introduction of dislocations, dynamic recovery and continuous dynamic recrystallization. New grains form at the region close to the pin tool by discontinuous dynamic recrystallization, in which large numbers of nuclei are formed in the deformed microstructure. Very small grains are formed by the grain boundary migration of these high densities of dislocations. The recrystallized grains grow with the subsequent thermal-mechanical deformation, with the further addition of dislocations.

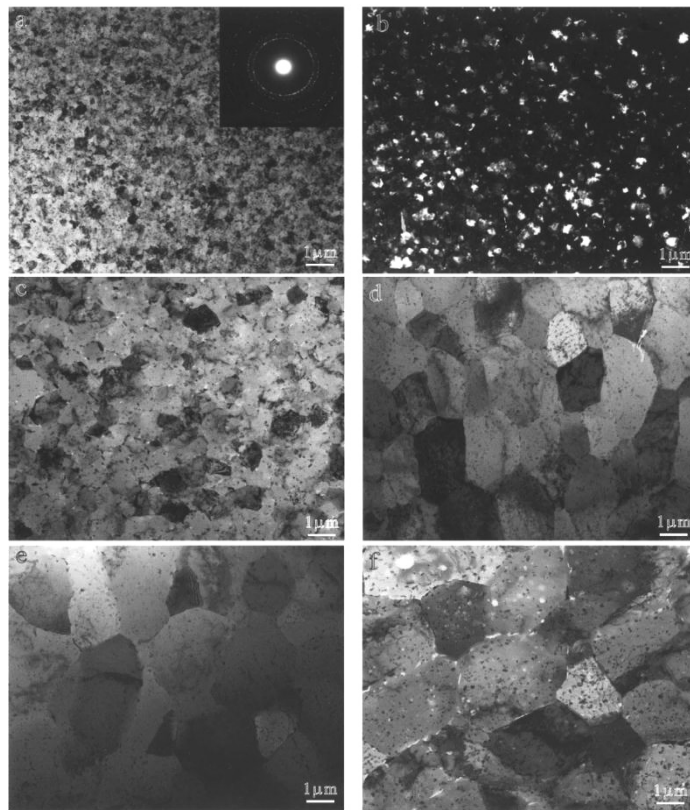


Figure 2.16: TEM micrographs of the different regions of the friction stir processed 7075 Al alloy; (a) S1 with the SAD pattern, (b) a dark-field image from S1, (c) S2, (d) S3, (e) S4 and (f) S5 [81].

Dynamic recovery is the governing mechanism for the further deformation. Continuous dynamic recrystallization leads to the formation of high angle boundaries from the sub-grains formed from dynamic recovery. Because of the heterogeneous nature of the deformation, the evolution of grains was different, as final grain structure contained a range of grain sizes. The

microstructure evolution suggested that the final structure is a function of tool design, processing parameters and also, cooling rate [81].

Microstructural evolution in the metals with hexagonal crystal structure is less clear, with a limited number of slip systems available as well as their propensity for mechanical twinning. Among the hexagonal systems, the behavior of magnesium alloys during FSW/FSP has been studied the most [50,58,61,92–100]. As seen in the cubic systems, it has been observed that FSW/FSP leads to significant grain refinement in these systems as well [38,61,82,92,95,98,101–105]. The stir zone has typically nearly equiaxed grains [62,92,95,104,106] at the center with much lesser presence of twins [107], which indirectly indicates the high temperature during FSW/FSP. Microstructure in the stir zone seemed to be recrystallized in appearance. The stir zone is also characterized by the presence of relatively high density of dislocations [95,107]. It should be noted that microstructural evolution during FSW/FSP of magnesium alloys and, therefore, the actual mechanism remains unclear.

Woo *et al.* [61] examined microstructure, chemical composition and hardness in an FSP AZ31B Mg alloy. They found no major differences in the chemical composition or hardness in the severely deformed SZ compared to the HAZ and BM, given the observed refinement in the grain size. Figure 2.17 shows the typical optical micrographs at various regions of the FSP zone for AZ31 Mg alloy.

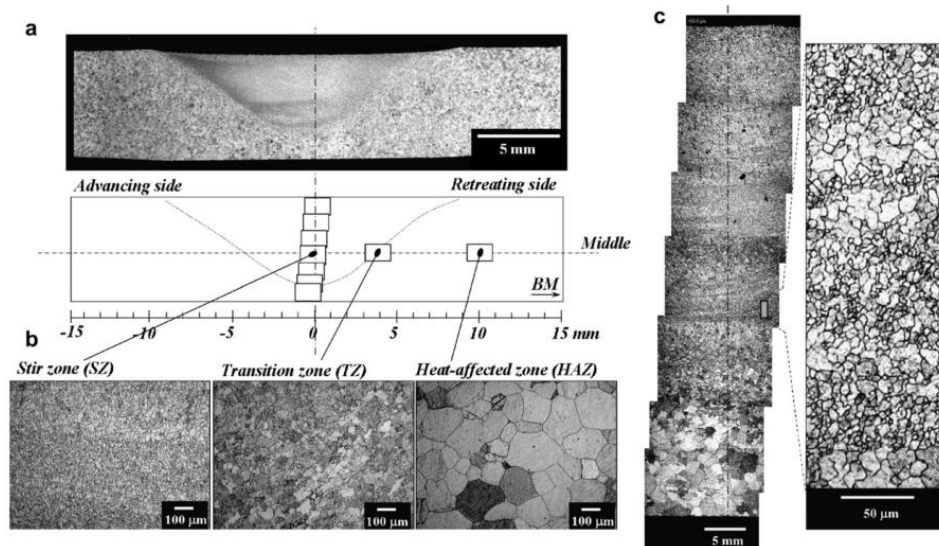


Figure 2.17: Optical micrographs of the AZ31B Mg alloy under FSP: (a) cross-sectional macrostructure; (b) microstructure of the various regions namely SZ, TZ and HAZ; and (c) microstructure through the thickness [61].

Afrin *et al.* [59] examined the important thermo-mechanically affected zone (TMAZ), which exhibited equiaxed grains. Also, smaller grain sizes were observed in the stir zone at a higher welding speed due to a lower heat input. Commin *et al.* [52] observed increase in the heat generation and subsequent grain growth due to increasing shoulder diameter or tool rotation speed or decreasing welding speed. Suhuddin *et al.* [99] observed that the material flow during friction stir welding of AZ31 magnesium is a very complex process associated mainly with basal slip. Development of grain structure was dictated by the texture evolution and also involved $\{10\bar{1}2\}$ twinning, geometrical effects of strain and limited discontinuous recrystallization. Figure 2.18 shows the evolution of the structure just behind and ahead of the tool and corresponding regions marked. The grain structure was closely associated with the texture development near the tool and grain convergence was induced by formation of a strong texture, thus increasing grain size and low angle boundary fraction. It was also verified that the material flow in the upper part of the friction stir weld was significantly affected by the tool shoulder.

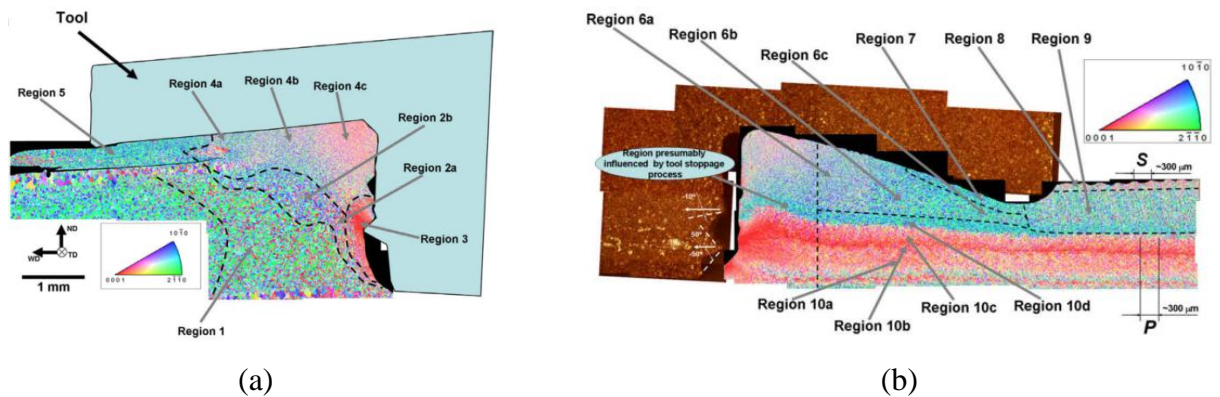


Figure 2.18: EBSD map taken ahead the tool keyhole (a) and behind the tool keyhole and (b) ahead of the tool [99].

Venkateswarlu *et al.* [108] investigated the effect of the overlapping ratio (0, 0.5 and 1) and the different shoulder diameters on the mechanical properties and formability of the friction stir processed (FSP) Mg AZ31B alloy. It was observed that the overlapping ratio of 1 showed better mechanical properties and formability than others and shoulder diameter of 18 mm produced superior properties. Recently, Mironov *et al.* [109] studied microstructure evolution (see figure 2.19) of FSP AZ31 magnesium alloy in a wide range of welding temperatures and found that the grain structure development gets significantly influenced by the formation of a very strong $\{0001\}\langle hwtv \rangle$ B-texture. Due to the limitations imposed by

this texture and the inherent symmetry of the HCP crystal structure, it was found that grain-boundary misorientation was extensively lowered during deformation. Production of ultrafine grain structure (few hundred nanometers) in Mg–Al–Zn alloy by friction stir processing has also been achieved by using specially designed rapid heat sinks [58,110].

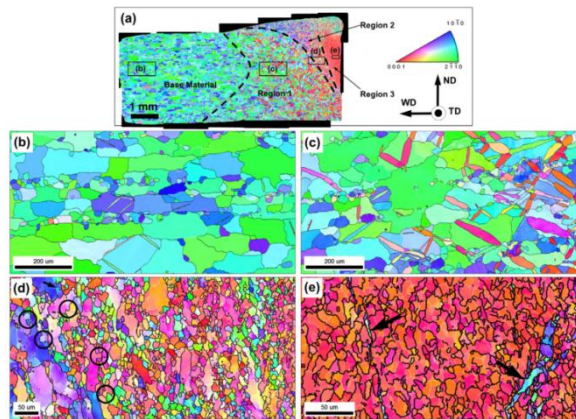


Figure 2.19: Microstructure evolution at relatively high welding temperature: (a) the composite EBSD map showing grain structure developed ahead of the welding tool in the stop-action experiment with selected areas shown at higher magnifications in (b)–(e) [109].

Because of the residual strain present in the regions of the nugget which are close to the pin, they are difficult to characterize using electron backscatter diffraction because of the poor pattern quality. This reinforces the steep strain and strain rate present in these locations. Replication of the thermomechanical cycle of FSW/FSP can be done by the tool plunge and extraction experiments followed by static annealing.

There have been debates on the plausible mechanisms operating during FSP viz. dynamic recovery, continuous dynamic recrystallization and grain boundary sliding [41,79,83,91]. Plastic deformation and high temperature generated in the stirred zone during FSW/FSP leads to recrystallization and modification of texture. Precipitate dissolution and coarsening occurs within and around the stirred zone.

The resultant microstructure in the stir zone is influenced by the nucleation and growth of the dynamic recrystallized grains [73]. Processing parameters, material chemistry, tool geometry, workpiece temperature, vertical force/pressure and rate of cooling affect the size of the recrystallized grains in the stir zone. Grain size and hence the mechanical properties of a

metallic material can be tailored in FSP by varying the processing parameters. Generally, the microstructure observed in FSP is obtained on the transverse section of the workpiece after the tool has passed. As described above, only few studies have looked into the “quick-stop” and tool extraction techniques to freeze the structure during the processing. Such studies gave new insights into the mechanisms of microstructure evolution and also highlighted that a combination of models is necessary to explain the different microstructures obtained in the processed zone.

2.5.2 Texture evolution during friction stir processing

Texture evolution during FSW/FSP has also been widely studied [31,38–41,54,62,63,78,96,99,105,111–123].

FSP significantly affects the texture of the parent pre-processed material and is shown to vary with the location in the processed zone [38]. Decade old studies on FSW/FSP textures by Field *et al.* [40] acknowledged that during FSW/FSP, the strain mode is ‘tortuous’. Presence of sharp spatial gradients was also reported. It was also suggested that the FSW texture developments in aluminum can be explained in terms of material flow. The observed texture could be used in estimation of the flow field during the processing. Center region of the weld and along the advancing side of the tool through the thickness of the plate showed the most severe textural gradients. Further, study of Fonda and Bingert [112] revealed significant differences in the crystallographic texture across TMAZ/HAZ regions of 2519 Al that were primarily due to macroscopic rigid-body rotations of the grains. Kang *et al.* [39] suggested that the microstructure and micro texture of the material near the stir zone is influenced by rotational behavior of tool pin. Also, Cho *et al.* [118] suggested that texture in the stir zone was random due to the weakness of the shear texture, which is induced by phase transformation that occurs in the stir zone during the processing.

Texture evolution in case of magnesium alloys have been usually characterized by the development of a very strong basal texture [38,63,99,124]. Park *et al.* [38] investigated distribution of microtexture in a friction-stir-welded magnesium alloy AZ61. The flow of material was found to be mainly by the shear deformation along the pin column surface during the processing. Since magnesium has hcp crystal structure, the slip deformation mainly

occurred on the basal (0002) plane. The distribution of slip planes in the welded zone of Mg alloys can be more easily located than the Al alloys (having larger number of slip systems). Microtexture analysis suggested that the nugget shape and the onion ring structure in the stir zone are related to the existence of the elliptical trace surface of the (0002) basal plane texture formed during FSW (see figure 2.20).

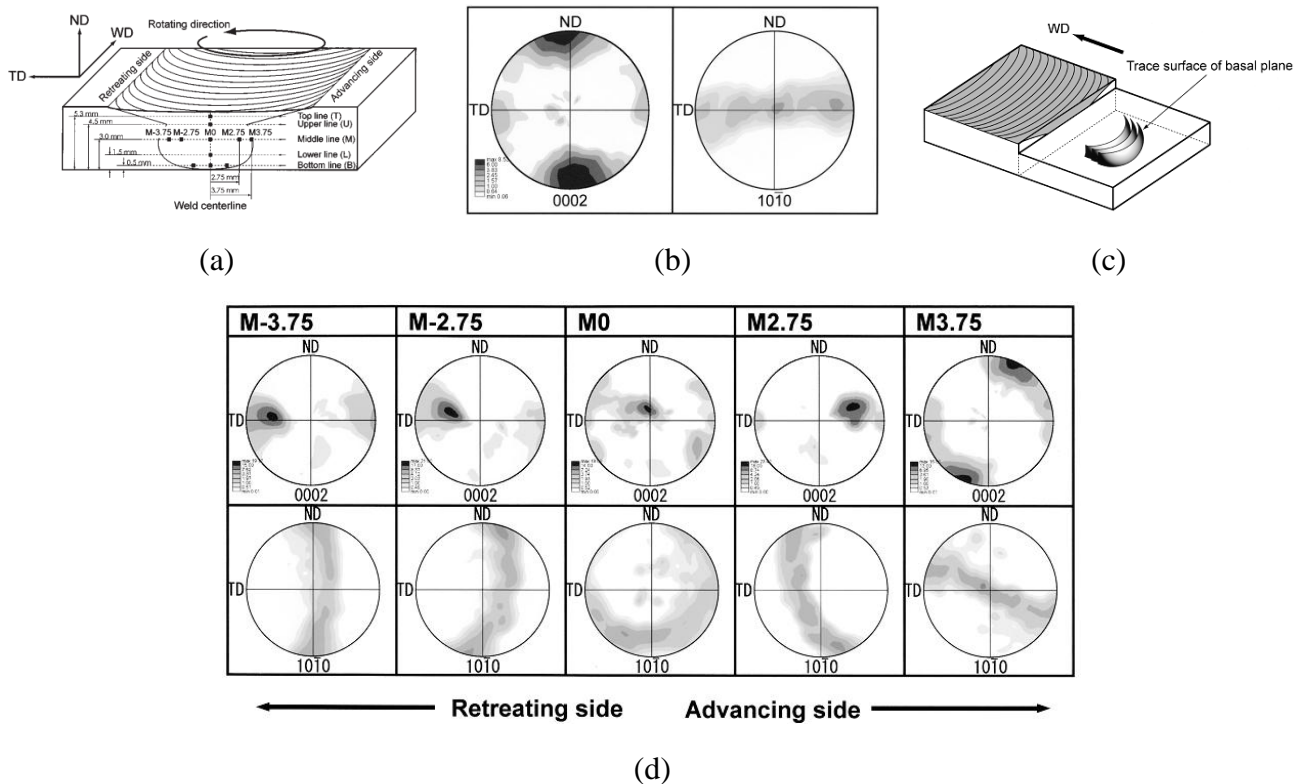
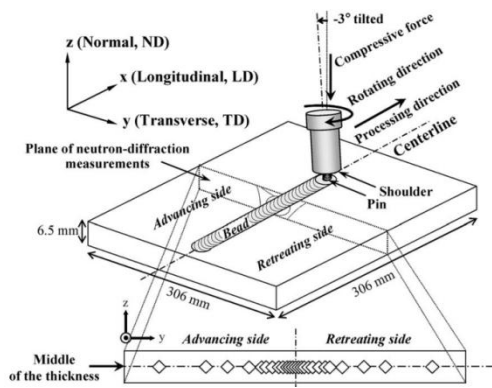
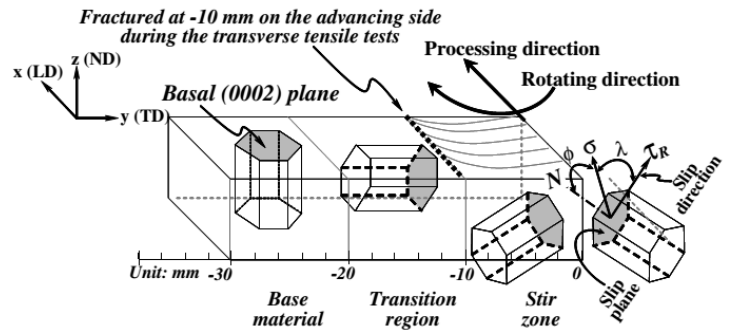


Figure 2.20: a) Schematic illustration of selected areas for analysis of microtexture, b) $\langle 0002 \rangle$ and $\langle 10\bar{1}0 \rangle$ pole figures of the base material. c) $\langle 0002 \rangle$ and $\langle 10\bar{1}0 \rangle$ pole figures along the middle line (as indicated in (a)) [38].

Woo *et al.* [63] showed significant texture variations between the transition region and stir zone of the AZ31B magnesium alloy plate. Tensile behaviour of the longitudinal samples (along the friction stir processing direction) including mainly the stir zone showed significant increase in the elongation and showed decrease in the tensile strength when compared to the base alloy. This was correlated to the drastic texture variations in the zone. Also, location of fracture in the samples was correlated to incompatible boundary between the transition region and the stir zone of FSP (see figure 2.21).



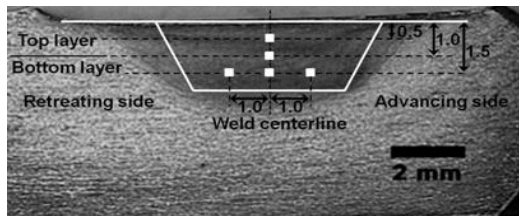
(a)



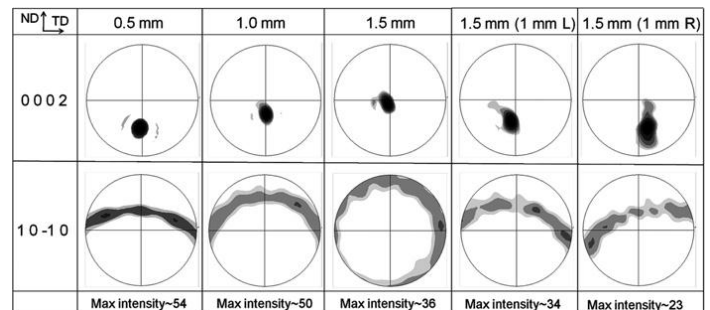
(b)

Figure 2.21: a) Schematic of the friction-stir processing, b) basal tracing from the base material, transition region, to stir zone on the advancing side of the FSP Mg plate [63].

Further, Yuan *et al.* [105] showed depth dependent basal texture in the stir zone. As the depth increased from 0.5 to 1.5 mm, the basal pole tilted from 37° to 86° with respect to the normal direction of the plate surface (figure 2.22).



(a)



(b)

Figure 2.22: (a) Cross section of the processed zone with tool profile indicated, (b) (0002) and (10 $\bar{1}$ 0) poles of FSP AZ31 material measured at different locations as shown in (a) [105].

The stir zone showed significant anisotropy in tensile behavior, with high tensile yield strength and high ductility, but having lower uniform strain in the transverse direction than in the processing direction. Basal plane slip dominated tensile deformation in the processing

direction; however, pyramidal $\langle c + a \rangle$ slip dominated the deformation in the transverse direction.

In a recent study, Chowdhury *et al.* [121] studied the microstructure, texture and tensile properties of friction stir welded AZ31B-H24 Mg alloy with varying tool rotational rates and welding speeds. The parent material had a strong crystallographic texture, with the basal planes (0002) largely parallel to the sheet plane and $\langle 11\bar{2}0 \rangle$ direction aligned in the RD. After processing, basal planes in the stir zone slightly tilted towards the TD and slightly inclined towards RD, due to the intense shear plastic flow near the pin surface (see figure 2.23). The prismatic planes $(10\bar{1}0)$ and pyramidal planes $(10\bar{1}1)$ formed mainly fiber-like textures.

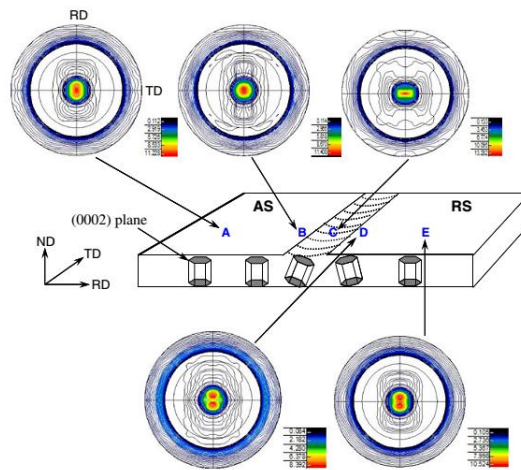


Figure 2.23: Basal (0002) pole figures from the top surface of a FSW joint made at a welding speed of 5 mm/s and tool rotational rate of 1000 rpm at different locations [121].

Yuan *et al.* [120] studied microstructural and texture evolution during one pass and two pass friction stir processing of as-cast AZ91 alloy. It was found that the FSP eliminated porosity and refined the grain size to 2.8 and 0.5 μm for one-pass and two-pass runs, respectively, however, it also lead to a strong basal fiber texture. Figure 2.24 shows the pole figure of the as cast, one pass and two pass conditions.

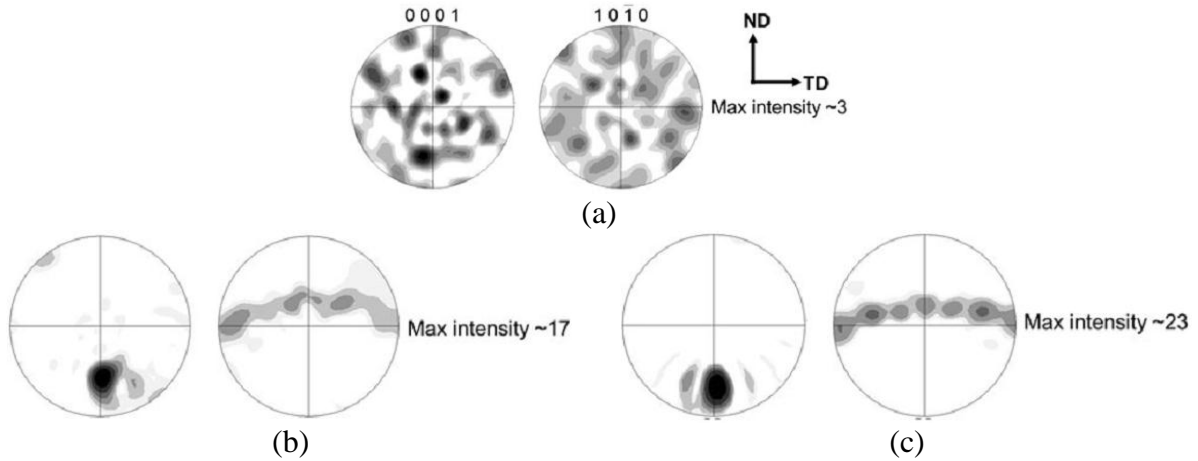


Figure 2.24: (0002) and (10 $\bar{1}$ 0) pole figures of AZ91 in (a) as-cast, (b) one-pass FSP and (c) two-pass FSP [120].

Further, Wang *et al.* [62] suggested that the high schmid factor of around 0.3 observed in the friction stir processed samples of AZ31 Mg alloy was responsible for the low parameters observed in the Hall-Petch relationship and hence have a weak grain size dependence. Bhargava *et al.* [96] showed fine grained structure and higher tensile strength and ductility for multiple-pass FSP compared to single pass FSP. FSP caused anisotropy in tensile properties with a higher level of anisotropy in multiple pass. The texture evolution during the friction stir process caused the {10 $\bar{1}$ 0} prismatic planes to be aligned for easy slip during tests in the transverse direction which lead to a good combination of ductility and strength.

2.5.3 Texture simulation during friction stir processing

Texture simulation using viscoplastic self-consistent (VPSC) methodology for polycrystal and velocity gradients can be done for friction stir welding/processing [113,114,116,123]. Velocity gradient can be predicted along the streamlines of the flow field during processing. In an Eulerian frame of reference, the velocity of a material particle, u , in a flow field is given by

$$u_i = \frac{\partial x_i}{\partial t} \quad (1)$$

where x is the position of the particle and t is the time. The velocity gradient, L , can be calculated by taking the spatial gradient of the velocity field:

$$L = \frac{\partial u_i}{\partial x_j} \quad (2)$$

The motion at the macroscopic scale can be correlated to the crystal scale by considering the extended Taylor hypothesis [125] in which the individual crystals can be expected to undergo the macroscopic velocity gradient. This approximation is reasonable for the case of the high symmetry crystals and large strains. Since crystals are assumed to deform solely by crystallographic slip and elastic effects are neglected, the crystal velocity gradient can be decomposed into a rigid lattice rotation and shearing along slip systems:

$$L = L^c = \Omega + \sum_{\alpha} \dot{\gamma}^{\alpha} T^{\alpha} \quad (3)$$

Where Ω is the lattice spin, $\dot{\gamma}^{\alpha}$ is the shear strain rate on the slip system α and T^{α} is the Schmid factor. Also, $T^{\alpha} = b^{\alpha} \times n^{\alpha}$, with b^{α} , the slip direction, and n^{α} , the slip plane normal for slip system α . A viscoplastic constitutive relation, given below, can be used to correlate the shear strain rate on a slip system to the resolved shear stress:

$$\dot{\gamma}^{\alpha} = \dot{\gamma}_0 \frac{\tau^{\alpha}}{\hat{\tau}} \left| \frac{\tau^{\alpha}}{\hat{\tau}} \right|^{(1/m-1)} \quad (4)$$

where m is the rate sensitivity, $\hat{\tau}$ is the slip system hardness (this is assumed to be identical for all slip systems), and $\dot{\gamma}_0$ is a reference strain rate. The resolved shear stress on the slip system (α) can be obtained as the projection of the crystal stress onto the slip system:

$$\tau^{\alpha} = P^{\alpha} \cdot \sigma^{c'} \quad (5)$$

where $P^{\alpha} = \text{sym}(T^{\alpha})$ and $\sigma^{c'}$ is the deviatoric crystal stress. Combining the symmetric part of the crystal velocity gradient in Eq. (3) with Eqs. (4) and (5) can give an expression for the crystal stress :

$$\sigma^{c'} = C^c [D^{c'}] \quad (6)$$

where the stiffness C^c is defined as:

$$C^{c-1} = \sum_{\alpha} \frac{\dot{\gamma}_0}{\hat{\tau}^{\alpha}} \left| \frac{\tau^{\alpha}}{\hat{\tau}} \right|^{(1/m-1)} P^{\alpha} \times P^{\alpha} \quad (7)$$

and $D^{C'}$ is the crystal deviatoric deformation rate. The skew part of the crystal velocity gradient in Eq. (3) yields an expression for the lattice spin:

$$\Omega = W - \sum_{\alpha} \dot{\gamma}^{\alpha} Q^{\alpha} \quad (8)$$

where W is the macroscopic spin, and $Q^{\alpha} = skew(T^{\alpha})$.

Cho *et al.* [113,114] predicted texture evolution in 304 stainless steel using the velocity gradients along streamlines of the flow field together with a model for polycrystal plasticity. Texture varied greatly with position (see figure 2.25). This implied that the mechanical properties also will vary strongly across the weld zone.

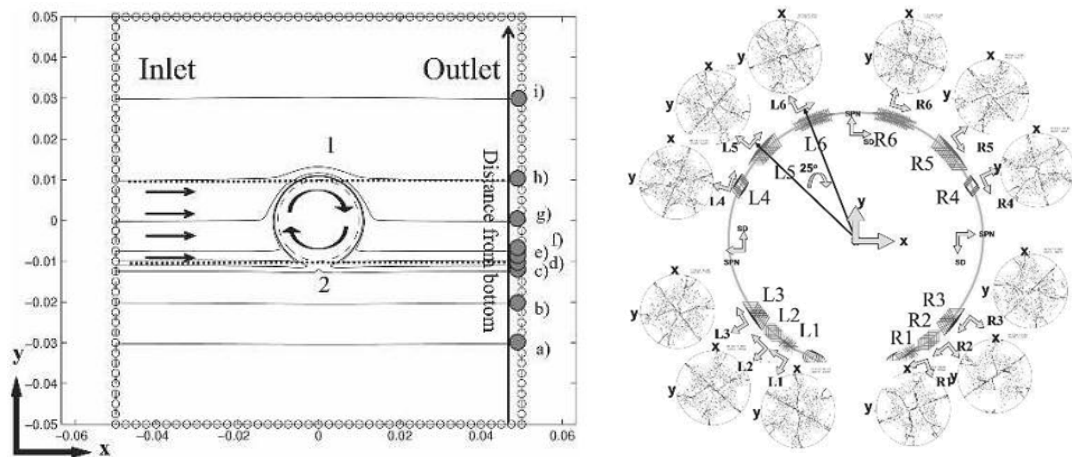


Figure 2.25: Streamline plot at various locations of FSW. Region 1 indicates the retreating side and region 2 indicates the advancing side. Nine streamlines are indicated from (a) through (i). Also shown, is the (111) pole figure for the transition regions and stagnation point along the longest streamline [114].

Cho *et al.* [123] used three-dimensional thermomechanical simulation by utilizing an Eulerian finite volume method under the steady state condition for the case of a 409 ferritic stainless steel and compared the simulated results with the experimentally measured temperature histories during FSW and the microstructural changes after FSW. Using viscoplastic self-consistent approach for polycrystal, texture evolution was predicted along the streamlines taking the velocity gradients into account.

2.5.4 Effect of quenching medium during friction stir processing

Friction stir processing/welding can generate nano-sized grains; however, the high temperatures encountered during the stirring process can stimulate the grains to grow further. Hence, maintaining smaller grain sizes is an important aspect associated with FSP parameters. Applications of coolant mediums have emerged as a plausible solution. Effect of the quenching medium during FSP on the resulting microstructure has been investigated in the past [58,69,110,126]. Ultrafine-grained (UFG) microstructures with an average grain size of 100-300 nm are achieved in solution-hardened AZ31 alloy prepared by friction stir processing equipped with a rapid heat sink [58,110]. The mean hardness of the UFG region reached twice as high as that of the AZ31 matrix (figure 2.26).

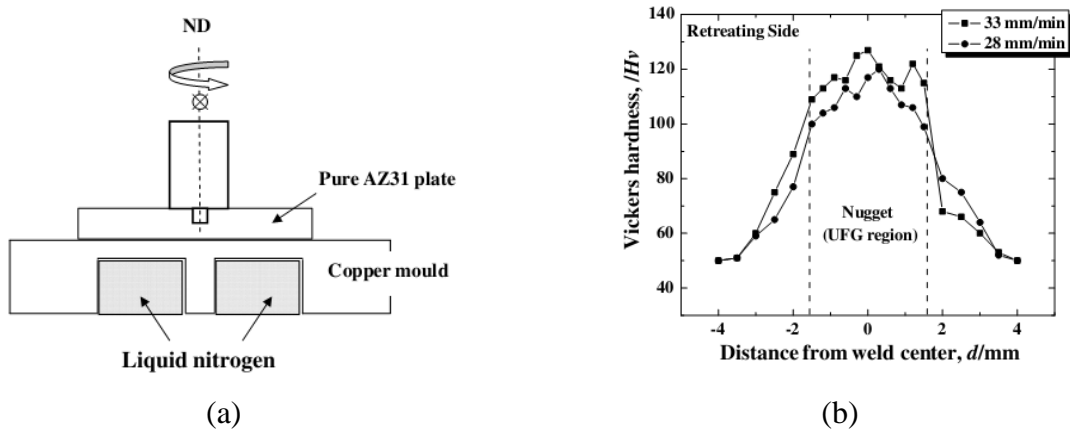


Figure 2.26: (a) Schematic of the cooling system used, (b) Micro hardness profile measured on cross-sectional planes for the FSP AZ31 alloy [58]

The mechanism for the formation of ultra-fine (nano-sized) grains using the two pass FSP done using heat sink is shown in figure 2.27. The grain size can be refined up till 85 nm using heat sink. The highest micro hardness reported is three times higher than the parent AZ31 matrix. Highly strained regions as well as dislocation walls, sub-grains and recrystallized grains are introduced, mainly via continuous dynamic recrystallization (CDRX), during the first pass.

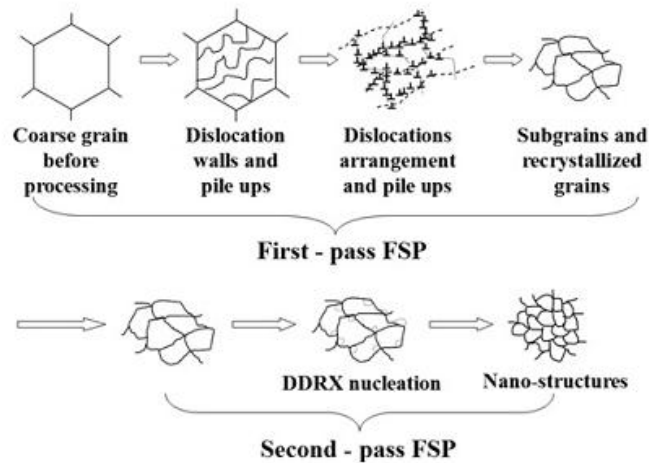


Figure 2.27: Schematic showing the grain refinement process of the two pass FSP AZ31 Mg specimens [110].

Owing to the lower heat input, high total strain, high strain rate and abundant sites for nucleation, discontinuous dynamic recrystallization (DDRX) appears to be responsible during the second pass FSP. By changing the processing parameters and cooling rate, final microstructure, including grain size, grain boundary structure and dislocation density can be controlled. The fundamental understanding of evolution of nano crystalline grains makes it possible [110].

2.5.5 Finite element simulation of friction stir welding/processing

The properties of the welded material, rotation and translational speed affect the heat and mass flow during FSW/FSP. Complicated interactions occur simultaneously among the various physical variables involved, which affects the material flow, heating/cooling rate, and hence the microstructure and properties of the welded/processed regions. Finite element analysis has been used widely to study the thermal and material flow during FSW/FSP and hence to investigate the optimization of the processing parameters.

Many such attempts of numerical models coupled with experimental data has been reported in the past [127–135]. However, most of the early works focused on the models of the heat transfer. Frigaard *et al.* [84] developed a three dimensional numerical model for heat flow using the finite element method, and further validated it using the in situ temperature

measurements using thermocouple at specific time interval during FSW. Chao *et al.* [129] studied the FSW considering it as a heat transfer problem by inverse modelling into two boundary value problems: a steady state boundary value problem and a transient boundary value problem for the workpiece. They used the finite element method (FEM) and concluded that about $4/5^{\text{th}}$ of the mechanical work is dissipated as heat while $1/5^{\text{th}}$ is transported into tool. Later, Khandkar *et al.* [136] formulated a 3-D thermal model which can predict transient temperature distribution in FSW of aluminium alloys. Experimental measurement of torque was used to estimate the heat generation. By adjusting the bottom heat transfer coefficient, good agreement between the simulated temperature profile and experimentally observed values were reported. Further, Song and Kovacevic [133,137] developed a 3-D heat transfer model for FSW by using a moving coordinate system. It was concluded that preheating of the workpiece is beneficial to FSW. The above mentioned models were helpful in better understanding of the FSW. However, these models did not take care of the convective heat transfer due to the flow of material.

Later, Cho *et al.* [113,114] used a two-dimensional (2D) heat and material flow model to simulate the material flow, thermal response and the strain hardening during FSW of stainless steel. They observed that temperature in the advancing side is about 100K higher than that of the temperature observed in the retreating side. Ulysse [138] developed a 3-D viscoplastic model to model the temperature profile during FSW. The model predicted the changes in the temperature profiles with welding variables, although, it had some inconsistencies between the measured and computed temperatures. It was also observed that the pin forces increased with increasing welding speed. Further, Seidel and Reynolds [139] formulated a 2-D thermal model based on a laminar, viscous and non-Newtonian flow around a circular cylinder. This model, however, could not be directly used to validate experimental data such as forces on the pin, weld energy and torque owing to its simplified assumptions.

Colegrove and Shercliff [131,140,141] devised a 3-D heat and material flow model during the FSW of aluminum alloys using a commercial computational fluid dynamics (CFD) code, FLUENT. They examined changes in material and heat flow during FSW with the design and rake angle of the tool through coupled thermal/flow analysis considering heat generation by viscous dissipation. Further, Assidi *et al.* [142] completed the calibration of the friction model using the 3-D numerical results obtained with the developed arbitrary

Lagrangian–Eulerian formulation. They reported that the Coulomb’s friction model enables an excellent agreement with experimental results such as tool temperatures and forces.

Nandan *et al.* [134] reported results of a 3-D heat transfer and material flow during FSW of 6061 aluminum alloy, 304 austenitic stainless steel [130] and 1018 low carbon steel [135]. They studied cooling rates, temperature fields, and plastic flow fields by solving the equations for conservation of mass, momentum and energy in three dimensions. They also considered heat generation, non-Newtonian viscosity as a function of strain rate and temperature and temperature-dependent physical properties in the calculation. The computed temperatures were in good agreement with experimentally measured values. Later, Arora *et al.* [116] reported the computed strains and strain rates during FSW of 2524 aluminum alloy from a 3-D coupled viscoplastic flow and heat transfer model. Further, Arora *et al.* [143] devised an analytical model which can predict the velocity, torque and peak temperature during FSW. These studies, however, have not focussed on the changes in the microstructure, texture and the geometry of the FSW/FSPed region during the processing.

Yu *et al.* [144] developed a computational fluid dynamics (CFD) model to study the material flow and heat transfer during friction stir processing (FSP) in an AZ31B magnesium alloy, assuming non-Newtonian viscoplastic fluid and describing the material viscosity on temperature and strain rate. This was done for smooth and threaded pins (see figure 2.28).

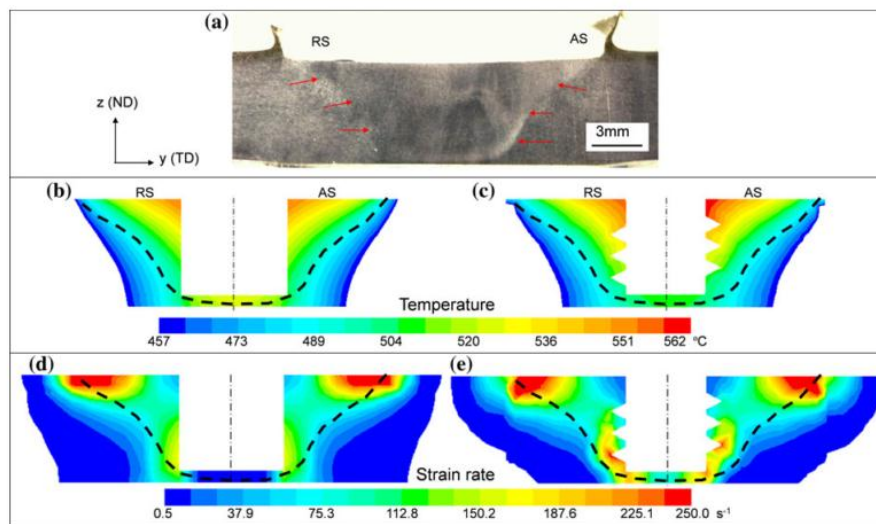


Figure 2.28: (a) Cross-section macrostructure of the processed zone. Contours of temperature (b) and (c), and contours of strain rate (d) and (e) for smooth pin and threaded pin, respectively, at a traveling time of 90 s. The red arrows in (a) and the black dashed lines in (b) through (e) mark the outline of the stir zone [144].

Further, Aljoaba *et al.* [126] studied a 3D CFD model to simulate FSP with and without coolant application and estimated the grain size of the processed material from the strain rate and Zener Holloman parameter. Figure 2.29 shows the temperature profile at a given coolant application rate with different rotational speeds.

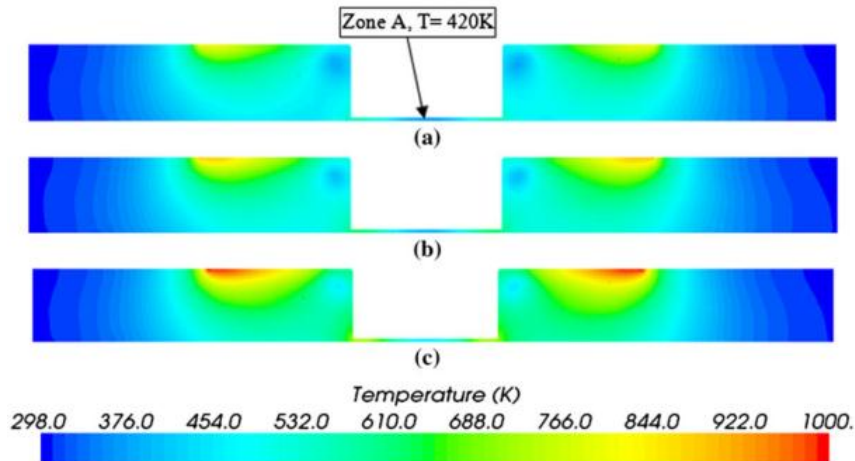


Figure 2.29: Simulated temperature distribution 1kg/s of coolant mass flow rate and at a rotational speed of a) 1000, b) 1200 and c) 1750rpm [126].

Finally, it can be outlined that severe plastic deformation and thermal exposure during FSW/FSP causes refinement of the parent structure, breakup of coarse dendrites and second-phase particles, dissolution of precipitates, closure of porosity, thereby creating a solid state fine and pore free structure. The successful applications of FSP in producing the fine-grained structure and surface composite, modifying the microstructure of nonhomogeneous materials, and synthesizing in-situ the composite/intermetallic compound have demonstrated that FSP is energy efficient, environment friendly, and versatile, and can be developed to be a generic metalworking technique that can provide localized modification and control of microstructures and texture in the near-surface layers of processed metallic components. With further research efforts and an increased understanding of the FSP process, an increasing number of applications will be found for FSP in the fabrication, processing, and synthesis of metallic materials. Although a number of challenges still exist, FSP offers very attractive possibilities for commercial success.

2.6 Introduction to twin roll casting

Given the magnesium alloys having good castability, machinability, recyclability, shielding capability, specific strength and stiffness [1,2], there has been large efforts of R&D on cast Mg alloys; however, R&D on wrought Mg alloys is rather limited. In particular, there is a lack of competitive Mg alloy sheet products, which are much needed for numerous weight-sensitive applications such as automotive body components. This is mainly due to the complexity of sheet production originating from the poor workability and low heat capacity of Mg alloys resulting in frequent intervening reheating procedures during hot rolling. As a result of this, manufacturing of Mg alloy sheets from direct chill (DC) cast ingots usually costs more than the steel and Al alloys. This prevents the wide-scale application of the Mg sheets in automobile industry [5,20].

Twin-roll casting (TRC) is an emerging manufacturing technology for producing metal sheets, strips or plates with much superior properties than the conventional ingot casting [145–148]. In this process, both casting and rolling is done in a single step, where the molten metal is fed between the gaps of internally cooled rolls, eventually leading to rapid solidification and hot deformation. Figure 2.30 shows the schematic of the twin roll casting process.

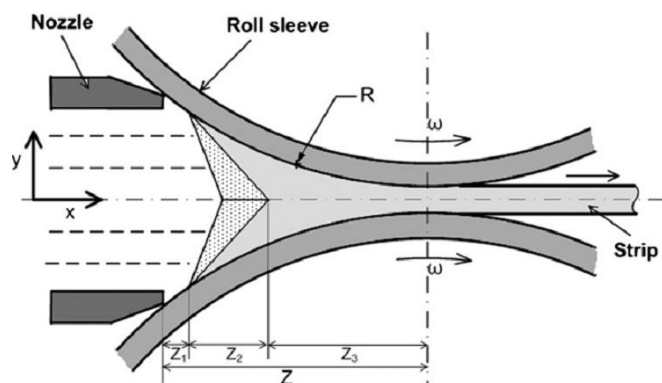


Figure 2.30: Schematic diagram of twin-roll casting process [149].

Twin-roll casting has shown to produce Mg alloy sheets having equivalent tensile properties to conventional ingot cast Mg alloys [150,151]. In this process, both casting and rolling is done in a single step, where the molten metal is fed between the gaps of internally cooled rolls, eventually leading to rapid solidification and hot deformation. TRC can produce thin Mg strips less than 10 mm in thickness compared to the conventional ingot casting

producing Mg slabs of over 300 mm in thickness. TRC is more economically viable since there is no need for subsequent rolling operation to produce the final products. In TRC, the solidification rate is much higher (10^2 to 10^3 K/s) compared to the conventional ingot casting (1~50 K/s). The fast solidification rate of TRC results in improving the homogeneity of microstructures, reducing segregation, enhancing precipitate nucleation within the matrix, increasing solid solubility and generating a distribution of fine precipitates [145]. TRC can produce near net shape products and hence can reduce the cost of production, thus, improving the commercial viability of Mg alloys in the automobile industry [152]. There are works being done on the microstructure study [147,150,153–159], modelling aspect [149,160,161] and also the thermal treatment [162] after TRC, however, the literature is limited.

2.7 Introduction to grain path envelope analysis

The growth path for any particle in a complex system can be defined as the variation of any of its geometrical state (for example: radius, for a spherical particle) with time during the microstructural transitions occurring. This piece of information of the particle can be used to sufficiently define the volume, surface area, topology and total curvature of the particle at any time. For the cases, when the shape remains same with time, however, the shape is complex; the ‘size’ of the particle can be defined by using any characteristic dimension.

If the shape and size both changes with times, then a two dimensional representation of the growth path can be deduced, which has a relationship between the particle shape and size. Most of the systems consisting of a nucleation and growth phenomenon are being expected to have heterogeneous distributions. Also, the particles, which may have nucleated at the same time, can follow different growth paths, which depend on the neighboring particles. In a given system, growth path is the curve associated with a nucleation. The growth path envelope of the system is defined as the continuum of the curves, which describe individually the geometric evolution of all the particles in a system.

Figure 2.31 summarizes the schematic growth paths for four cases of microstructural change. Figure 2.31(a) represents the case where the growth is size dependent, in other words, it depends on the size of the particle and not upon the time it nucleated and the time of observation of the particle. Figure 2.31(b) represents the case where growth is dependent on

the time of observation but not on the time when the particle nucleated or the size of the particle at the time of the observation. Figure 2.31 (c) shows the case where the growth rate of the particle depends on both the particle size and the time of observation. Figure 2.31(d) shows an example of a system where the growth paths of particles intersect. In this case, it is difficult to find out the history of a particle of size R to its origin and to calculate the time of its nucleation. Hence, this method will only be applicable to systems for which the individual growth paths do not cross each other.

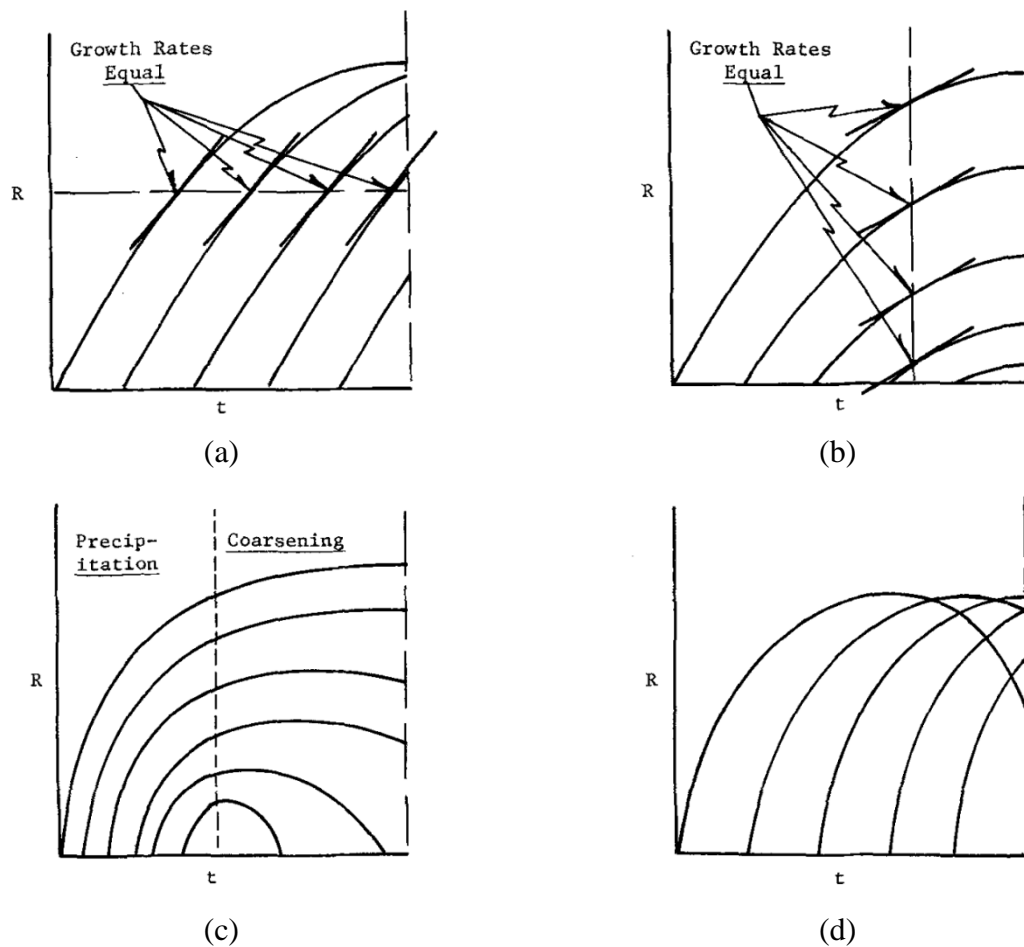


Figure 2.31: Schematic of the growth path envelopes for various microstructural changes: (a) growth rate size dependent only, (b) growth rate time dependent only (c) growth rate size and time dependent and (d) crossing growth paths [163].

Estimation of the size distribution of the particle is an important step in grain envelope analysis. Size distribution function is the number of particles, which exists in each of several size classes in the given system. A frequency function, $f(R, t)$, can be defined for a continuous distribution of sizes, where $f(R, t)dR$ is the fraction of all the particles in the system at time t

which lie in the size range of R to $R + dR$. A number density function $n_v(R, t)$ can hence be defined where $n_v(R, t)dR$ is the number of particles per unit volume in the system in the size range of R to $R + dR$. The two can be related by the following equation where $N_v(t)$ is the total number of particles in the system at time t [163].

$$n_v(R, t) = N_v(t)f(R, t) \quad (9)$$

Another function, $N_{v>}(R, t)$ can be defined, which is the number of particles per unit volume that are larger than size R at time t . The number frequency can be related to this function by the following expression where R_{max} is the size of the largest particles in the system at time t .

$$N_{v>}(R, t) = \int_R^{R_{max}} n_v(R, t)dR \quad (10)$$

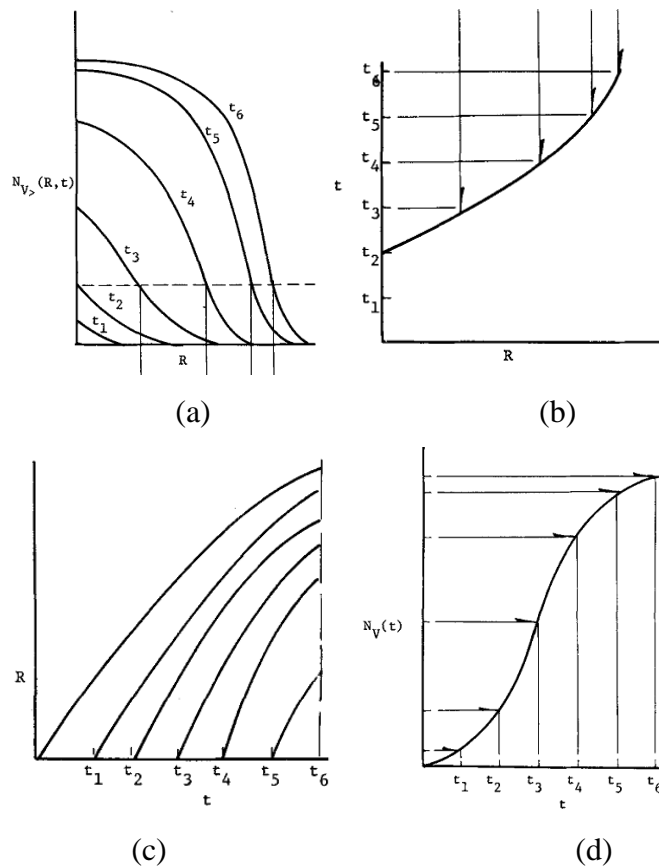


Figure 2.32: Illustration of the procedure for deducing the growth path envelope (c) and nucleation rates (d) from a representation of the evolution of particle size distribution (a) [163].

The assumption of growth paths not crossing against each other enables the tracking of growth path of a single particle. Supposing τ to be the time at which a particle nucleated, no matter when this particle is observed, the particles, which get nucleated before τ , will be larger than the concerned particle. If it is observed at time t with the size R , the number of particles with size greater than size R at time t will be equal to the number of particles which nucleated before time τ . Along the growth path of a particle, the number of particles that are larger will always be a constant, and it will be equal to the number of particles that nucleated before the concerned particle came into existence.

Thus, the common factor which identifies particles belonging to the same growth path in a series of observations of the size distribution of the structure is that the $N_{v>}(R, t)$ function is constant as shown in figure 2.32. Figure 2.32 shows the steps of estimating the growth envelope along a non-crossing grain growth path.

References

1. K. U. Kainer, Magnesium: Proceedings of the 6th International Conference Magnesium Alloys and Their Applications (2003).
2. B. L. Mordike and T. Ebert, Mater. Sci. Eng. A **302**, 37 (2001).
3. M. Easton, A. Beer, M. Barnett, C. Davies, G. Dunlop, Y. Durandet, S. Blacket, T. Hilditch, and P. Beggs, JOM **60**, 57 (2008).
4. K. U. Kainer, Magnesium – Alloys and Technology (2003).
5. I. J. Polmear, Mater. Sci. Technol. **10**, 1 (1994).
6. M. M. Avedesian and H. Baker, Magnesium and Magnesium Alloys-ASM Specialty Handbook (ASM International, The Materials Information Society, 1999).
7. S. E. Jensen and E. Nonbel, Description of the Magnox Type of Gas Cooled Reactor (MAGNOX) (1999).
8. S. R. Agnew, J. W. Senn, and J. A. Horton, JOM **58**, 62 (2006).
9. H. Yoshinaga and R. Horiuchi, Trans. JIM **4**, 1 (1963).
10. B. Hutchinson, Int. J. Mater. Res. **100**, 556 (2009).
11. J. Bohlen, M. R. Nürnberg, J. W. Senn, D. Letzig, and S. R. Agnew, Acta Mater. **55**, 2101 (2007).
12. S. R. Agnew and O. Duygulu, Mater. Sci. Forum **419-422**, 177 (2003).

13. S. R. Agnew and Ö. Duygulu, *Int. J. Plast.* **21**, 1161 (2005).
14. J. F. Nie, *Scr. Mater.* **48**, 981 (2003).
15. N. Stanford and M. R. Barnett, *Mater. Sci. Eng. A* **496**, 399 (2008).
16. J. F. Nie and B. C. Muddle, *Acta Mater.* **48**, 1691 (2000).
17. S. M. Zhu and J. F. Nie, *Scr. Mater.* **50**, 51 (2004).
18. X. Gao, S. M. He, X. Q. Zeng, L. M. Peng, W. J. Ding, and J. F. Nie, *Mater. Sci. Eng. A* **431**, 322 (2006).
19. T. V Padfield, *ASM Handb.* **9**, 801 (2004).
20. I. J. Polmear, *Light Alloys: Metallurgy of the Light Metals* (London, Arnold, 1995).
21. J.-F. Nie, *Metall. Mater. Trans. A* **43**, 3891 (2012).
22. *ASM Metals Handbook Volume 3 Alloy Phase Diagrams* (2010).
23. S. M. Zhu, B. L. Mordike, and J. F. Nie, *Mater. Sci. Eng. A* **483-484**, 583 (2008).
24. S. M. Zhu, M. A. Gibson, M. A. Easton, and J. F. Nie, *Scr. Mater.* **63**, 698 (2010).
25. M. S. Dargusch, S. M. Zhu, J. F. Nie, and G. L. Dunlop, *Scr. Mater.* **60**, 116 (2009).
26. S. M. Zhu, M. A. Gibson, J. F. Nie, M. A. Easton, and G. L. Dunlop, *Metall. Mater. Trans. A* **40**, 2036 (2009).
27. W.-F. Xu, Y. Zhang, J. R. TerBush, L.-M. Peng, W.-J. Ding, and J.-F. Nie, *Metall. Mater. Trans. A* **45**, 4103 (2014).
28. O. Engler and V. Randle, *Introduction to Texture Analysis Macrotecture, Microtexture and Orientation Mapping, Second Edi* (Taylor and Francis Group, 2010).
29. B. Verlinden, J. Driver, I. Samajdar, and R. D. Doherty, *Thermomechanical Processing of Metallic Materials, First Edition* (Pergamon Materials Series, 2007).
30. Y. Wang and J. Huang, *Mater. Chem. Phys.* **81**, 11 (2003).
31. A. P. Reynolds, E. Hood, and W. Tang, *Scr. Mater.* **52**, 491 (2005).
32. C. N. Tomé, P. J. Maudlin, R. A. Lebensohn, and G. C. Kaschner, *Acta Mater.* **49**, 3085 (2001).
33. H. T. Jeong and T. K. Ha, *J. Mater. Process. Technol.* **187-188**, 559 (2007).
34. A. Styczynski, C. Hartig, J. Bohlen, and D. Letzig, *Scr. Mater.* **50**, 943 (2004).
35. G. Proust, C. N. Tomé, and G. C. Kaschner, *Acta Mater.* **55**, 2137 (2007).
36. W. Xia, Z. Chen, D. Chen, and S. Zhu, *J. Mater. Process. Technol.* **209**, 26 (2009).
37. B. Verlinden, J. Driver, I. Samajdar, and R. D. Doherty, *Thermomechanical Processing of Metallic Materials, First Edition* (Pergamon Materials Series, 2007).
38. S. H. C. Park, Y. S. Sato, and H. Kokawa, *Metall. Mater. Trans. A* **34**, 987 (2003).
39. S. H. Kang, H. N. Han, K. H. Oh, J.-H. Cho, C. G. Lee, and S.-J. Kim, *Met. Mater. Int.* **15**, 1027 (2009).
40. D. P. Field, T. W. Nelson, Y. Hovanski, and K. V. Jata, *Metall. Mater. Trans. A* **32**, 2869

(2001).

41. R. W. Fonda, J. F. Bingert, and K. J. Colligan, *Scr. Mater.* **51**, 243 (2004).
42. R. S. Mishra and Z. Y. Ma, *Mater. Sci. Eng. R Reports* **50**, 1 (2005).
43. R. Nandan, T. Debroy, and H. K. D. H. Bhadeshia, *Prog. Mater. Sci.* **53**, 980 (2008).
44. K. Elangovan and V. Balasubramanian, *Mater. Des.* **29**, 362 (2008).
45. Y. N. Zhang, X. Cao, S. Larose, and P. Wanjara, *Can. Metall. Q.* **51**, 250 (2012).
46. G. Buffa, J. Hua, R. Shivpuri, and L. Fratini, *Mater. Sci. Eng. A* **419**, 381 (2006).
47. B. C. Liechty and B. W. Webb, *Int. J. Mach. Tools Manuf.* **48**, 1474 (2008).
48. F.-Y. Hung, C.-C. Shih, L.-H. Chen, and T.-S. Lui, *J. Alloys Compd.* **428**, 106 (2007).
49. A. H. Feng and Z. Y. Ma, *Scr. Mater.* **56**, 397 (2007).
50. L. Commin, M. Dumont, J.-E. Masse, and L. Barrallier, *Acta Mater.* **57**, 326 (2009).
51. V. Jain, W. Yuan, R. S. Mishra, G. Gouthama, and A. K. Gupta, *Mater. Sci. Forum* **702-703**, 64 (2011).
52. L. Commin, M. Dumont, J.-E. Masse, and L. Barrallier, *Acta Mater.* **57**, 326 (2009).
53. Z. Y. Ma, *Metall. Mater. Trans. A* **39**, 642 (2008).
54. J. M. Root, D. P. Field, and T. W. Nelson, *Metall. Mater. Trans. A* **40**, 2109 (2009).
55. A. A. Luo, *Mater. Sci. Forum* **419-422**, 57 (2003).
56. W. Yuan, S. K. Panigrahi, J.-Q. Su, and R. S. Mishra, *Scr. Mater.* **65**, 994 (2011).
57. J. J. Jeon, S. Mironov, Y. S. Sato, H. Kokawa, S. H. C. Park, and S. Hirano, *Metall. Mater. Trans. A* **44**, 3157 (2013).
58. C. I. Chang, X. H. Du, and J. C. Huang, *Scr. Mater.* **57**, 209 (2007).
59. N. Afrin, D. L. Chen, X. Cao, and M. Jahazi, *Mater. Sci. Eng. A* **472**, 179 (2008).
60. P. Asadi, M. K. Besharati Givi, and G. Faraji, *Mater. Manuf. Process.* **25**, 1219 (2010).
61. W. Woo, H. Choo, M. B. Prime, Z. Feng, and B. Clausen, *Acta Mater.* **56**, 1701 (2008).
62. Y. N. Wang, C. I. Chang, C. J. Lee, H. K. Lin, and J. C. Huang, *Scr. Mater.* **55**, 637 (2006).
63. W. Woo and H. Choo, *Scr. Mater.* **54**, 1859 (2006).
64. Y. Saito, H. Utsunomiya, N. Tsuji, and T. Sakai, *Acta Mater.* **47**, 579 (1999).
65. K. Matsubara, Y. Miyahara, Z. Horita, and T. G. Langdon, *Acta Mater.* **51**, 3073 (2003).
66. J. A. del Valle, F. Carreño, and O. A. Ruano, *Acta Mater.* **54**, 4247 (2006).
67. Z. Y. Ma, A. L. Pilchak, M. C. Juhas, and J. C. Williams, *Scr. Mater.* **58**, 361 (2008).
68. V. Manvatkar, A. De, L. Svensson, and T. DebRoy, *Scr. Mater.* **94**, 36 (2015).
69. F. Chai, D. Zhang, and Y. Li, *Materials (Basel)*. **7**, 1573 (2014).
70. R. S. Mishra and Z. Y. Ma, *Mater. Sci. Eng. R Reports* **50**, 1 (2005).

71. R. D. Doherty, D. A. Hughes, F. J. Humphreys, J. J. Jonas, D. Juul Jensen, M. E. Kassner, W. E. King, T. R. McNelley, H. J. McQueen, and A. D. Rollett, *Mater. Sci. Eng. A* **A238**, 219 (1997).
72. T. Sakai and J. J. Jonas, *Acta Metall.* **32**, 189 (1984).
73. F. J. Humphreys and M. Hatherly, *Recrystallization and Related Annealing Phenomenon*, Second Edition (Elsevier, 2004).
74. A. Azushima, R. Kopp, A. Korhonen, D. Y. Yang, F. Micari, G. D. Lahoti, P. Groche, J. Yanagimoto, N. Tsuji, A. Rosochowski, and A. Yanagida, *CIRP Ann. - Manuf. Technol.* **57**, 716 (2008).
75. H. K. Kim and W. J. Kim, *Mater. Sci. Eng. A* **385**, 300 (2004).
76. B. Li, S. Joshi, K. Azevedo, E. Ma, K. T. Ramesh, R. B. Figueiredo, and T. G. Langdon, *Mater. Sci. Eng. A* **517**, 24 (2009).
77. K. Edalati, T. Fujioka, and Z. Horita, *Mater. Sci. Eng. A* **497**, 168 (2008).
78. T. R. McNelley, S. Swaminathan, and J. Q. Su, *Scr. Mater.* **58**, 349 (2008).
79. K. V. Jata and S. L. Semiatin, *Scr. Mater.* **43**, 743 (2000).
80. J.-Q. Su, T. W. Nelson, R. Mishra, and M. Mahoney, *Acta Mater.* **51**, 713 (2003).
81. J.-Q. Su, T. W. Nelson, and C. J. Sterling, *Mater. Sci. Eng. A* **405**, 277 (2005).
82. W. Yuan and R. S. Mishra, *Mater. Sci. Eng. A* **558**, 716 (2012).
83. Z. Y. Ma, R. S. Mishra, and M. W. Mahoney, *Acta Mater.* **50**, 4419 (2002).
84. Ø. Frigaard, Ø. Grong, and O. T. Midling, *Metall. Mater. Trans. A* **32**, 1189 (2001).
85. M. W. Mahoney, C. G. Rhodes, J. G. Flintoff, W. H. Bingel, and R. a. Spurling, *Metall. Mater. Trans. A* **29**, 1955 (1998).
86. C. G. Rhodes, M. W. Mahoney, W. H. Bingel, R. a. Spurling, and C. C. Bampton, *Scr. Mater.* **36**, 69 (1997).
87. G. Liu, L. E. Murr, C.-S. Niou, J. C. McClure, and F. R. Vega, *Scr. Mater.* **37**, 355 (1997).
88. Y. S. Sato, M. Urata, and H. Kokawa, *Metall. Mater. Trans. A* **33**, 625 (2002).
89. K. Oh-Ishi and T. R. McNelley, *Metall. Mater. Trans. A Phys. Metall. Mater. Sci.* **35 A**, 2951 (2004).
90. Z. Yu, H. Choo, Z. Feng, and S. C. Vogel, *Scr. Mater.* **63**, 1112 (2010).
91. P. B. Prangnell and C. P. Heason, *Acta Mater.* **53**, 3179 (2005).
92. R. Xin, L. Sun, D. Liu, Z. Zhou, and Q. Liu, *Mater. Sci. Eng. A* **602**, 1 (2014).
93. D. U. Xinghao and W. U. Baolin, *Sci. China Ser. E Technol. Sci.* **52**, 1751 (2009).
94. P. Cavaliere and P. P. De Marco, *Mater. Sci. Eng. A* **462**, 393 (2007).
95. S. H. C. Park, Y. S. Sato, and H. Kokawa, *Scr. Mater.* **49**, 161 (2003).
96. G. Bhargava, W. Yuan, S. S. Webb, and R. S. Mishra, *Metall. Mater. Trans. A* **41**, 13 (2009).
97. A. H. Feng and Z. Y. Ma, *Acta Mater.* **57**, 4248 (2009).

98. C. J. Lee, J. C. Huang, and X. H. Du, *Scr. Mater.* **56**, 875 (2007).
99. U. F. H. R. Suhuddin, S. Mironov, Y. S. Sato, H. Kokawa, and C.-W. Lee, *Acta Mater.* **57**, 5406 (2009).
100. B. M. Darras, M. K. Khraisheh, F. K. Abu-Farha, and M. A. Omar, *J. Mater. Process. Technol.* **191**, 77 (2007).
101. R. Xin, D. Liu, B. Li, L. Sun, Z. Zhou, and Q. Liu, *Mater. Sci. Eng. A* **565**, 333 (2013).
102. A. Mohan, W. Yuan, and R. S. Mishra, *Mater. Sci. Eng. A* **562**, 69 (2013).
103. W. Yuan, R. S. Mishra, B. Carlson, R. Verma, and R. K. Mishra, *Mater. Sci. Eng. A* **543**, 200 (2012).
104. W. Xunhong and W. Kuaishe, *Mater. Sci. Eng. A* **431**, 114 (2006).
105. W. Yuan, R. S. Mishra, B. Carlson, R. K. Mishra, R. Verma, and R. Kubic, *Scr. Mater.* **64**, 580 (2011).
106. C. I. Chang, C. J. Lee, and J. C. Huang, *Scr. Mater.* **51**, 509 (2004).
107. J. Yang, B. L. Xiao, D. Wang, and Z. Y. Ma, *Mater. Sci. Eng. A* **527**, 708 (2010).
108. G. Venkateswarlu, D. Devaraju, M. J. Davidson, B. Kotiveerachari, and G. R. N. Tagore, *J. Mater. Des.* **45**, 480 (2013).
109. S. Mironov, T. Onuma, Y. S. Sato, and H. Kokawa, *Acta Mater.* **100**, 301 (2015).
110. C. I. Chang, X. H. Du, and J. C. Huang, *Scr. Mater.* **59**, 356 (2008).
111. J. A. Schneider and A. C. Nunes, *Metall. Mater. Trans. B* **35**, 777 (2004).
112. R. W. Fonda and J. F. Bingert, *Metall. Mater. Trans. A* **35**, 1487 (2004).
113. J.-H. Cho, D. E. Boyce, and P. R. Dawson, *Mater. Sci. Eng. A* **398**, 146 (2005).
114. J.-H. Cho and P. R. Dawson, *Metall. Mater. Trans. A* **37**, 1147 (2006).
115. R. S. Coelho, A. Kostka, H. Pinto, S. Riekehr, M. Koçak, and a. R. Pyzalla, *Mater. Sci. Eng. A* **485**, 20 (2008).
116. A. Arora, Z. Zhang, A. De, and T. DebRoy, *Scr. Mater.* **61**, 863 (2009).
117. N. T. Kumbhar, S. K. Sahoo, I. Samajdar, G. K. Dey, and K. Bhanumurthy, *Mater. Des.* **32**, 1657 (2011).
118. H.-H. Cho, S. H. Kang, S.-H. Kim, K. H. Oh, H. J. Kim, W.-S. Chang, and H. N. Han, *Mater. Des.* **34**, 258 (2012).
119. M. Abbasi, T. W. Nelson, and C. D. Sorensen, *Metall. Mater. Trans. A Phys. Metall. Mater. Sci.* **43**, 4940 (2012).
120. W. Yuan, S. K. Panigrahi, and R. S. Mishra, *Metall. Mater. Trans. A* **44**, 3675 (2013).
121. S. H. Chowdhury, D. L. Chen, S. D. Bhole, X. Cao, and P. Wanjara, *Metall. Mater. Trans. A* **44**, 41 (2012).
122. J. Young, D. Field, and T. Nelson, *Metall. Mater. Trans. A* **44**, 3167 (2013).
123. H.-H. Cho, S.-T. Hong, J.-H. Roh, H.-S. Choi, S. H. Kang, R. J. Steel, and H. N. Han, *Acta Mater.* **61**, 2649 (2013).

124. S.-H. Kim, B.-S. You, C. Dong Yim, and Y.-M. Seo, *Mater. Lett.* **59**, 3876 (2005).
125. G. I. Taylor, *Inst. Met.* **62**, 307 (1938).
126. S. Aljoaba, O. Dillon, M. Khraisheh, and I. S. Jawahir, *J. Mater. Eng. Perform.* **21**, 1141 (2011).
127. K. Mundra, T. DebRoy, and K. M. Kelkar, *Numer. Heat Transf. Appl. An Int. J. Comput. Methodol.* **Part A**, 115 (1996).
128. D. Kim, H. Badarinarayan, J. Kim, C. Kim, K. Okamoto, R. H. Wagoner, and K. Chung, *Eur. J. Mech. Solids* **29**, 204 (2010).
129. Y. J. Chao, X. Qi, and W. Tang, *J. Manuf. Sci. Eng.* **125**, 138 (2003).
130. R. Nandan, G. G. Roy, T. J. Lienert, and T. Debroy, *Sci. Technol. Weld. Join.* **11**, 526 (2006).
131. P. A. Colegrove and H. R. Shercliff, *Sci. Technol. Weld. Join.* **8**, 360 (2003).
132. X. He, F. Gu, and A. Ball, *Prog. Mater. Sci.* **65**, 1 (2014).
133. M. Song and R. Kovacevic, *Proc. Inst. Mech. Eng. Part B J. Eng. Manuf.* **217**, 73 (2003).
134. R. Nandan, G. G. Roy, and T. Debroy, *Metall. Mater. Trans. A* **37A**, 1247 (2006).
135. R. Nandan, G. G. Roy, T. J. Lienert, and T. Debroy, *Acta Mater.* **55**, 883 (2007).
136. M. Z. H. Khandkar, J. A. Khan, and A. P. Reynolds, *Sci. Technol. Weld. Join.* **8**, 165 (2003).
137. M. Song and R. Kovacevic, *Mach. Tools Manuf.* **43**, 605 (2003).
138. P. Ulysse, *Mach. Tools Manuf.* **42**, 1549 (2002).
139. T. U. Seidel and A. P. Reynolds, *Sci. Technol. Weld. Join.* **8**, 175 (2003).
140. P. A. Colegrove and H. R. Shercliff, *J. Mater. Process. Technol.* **169**, 320 (2005).
141. P. A. Colegrove and H. R. Shercliff, *Sci. Technol. Weld. Join.* **9**, 345 (2004).
142. M. Assidi, L. Fourment, S. Guerdoux, and T. Nelson, *Int. J. Mach. Tools Manuf.* **50**, 143 (2010).
143. A. Arora, T. Debroy, and H. K. D. H. Bhadeshia, *Acta Mater.* **59**, 2020 (2011).
144. Z. Yu, W. Zhang, H. Choo, and Z. Feng, *Metall. Mater. Trans. A* **43A**, 724 (2012).
145. D. Liang and C. B. Cowley, *JOM* **56**, 26 (2004).
146. P. D. Ding, F. S. Pan, B. Jiang, J. Wang, H. L. Li, J. C. Wu, Y. W. Xu, and Y. Wen, *Trans. Nonferrous Met. Soc. China (English Ed.)* **18**, s7 (2008).
147. L. L. Chang, J. H. Cho, and S. K. Kang, *Mater. Des.* **34**, 746 (2012).
148. G. S. Wang, H. S. Di, and F. Huang, *Trans. Nonferrous Met. Soc. China (English Ed.)* **20**, 973 (2010).
149. H. Zhao, P. Li, and L. He, *J. Mater. Process. Technol.* **211**, 1197 (2011).
150. S. S. Park, G. T. Bae, D. H. Kang, I. H. Jung, K. S. Shin, and N. J. Kim, *Scr. Mater.* **57**, 793 (2007).

151. K.-H. Kim, J. G. Lee, G. T. Bae, J. H. Bae, and N. J. Kim, *Mater. Trans.* **49**, 980 (2008).
152. S. S. Park, W. J. Park, C. H. Kim, B. S. You, and N. J. Kim, *JOM* **61**, 14 (2009).
153. H. Zhao, L. J. He, and P. J. Li, *Trans. Nonferrous Met. Soc. China (English Ed.)* **21**, 2372 (2011).
154. S. S. Park, Y. S. Oh, D. H. Kang, and N. J. Kim, *Mater. Sci. Eng. A* **448-451**, 352 (2007).
155. H. Z. Li, H. T. Liu, Z. Y. Liu, H. H. Lu, H. Y. Song, and G. D. Wang, *Mater. Charact.* **88**, 1 (2014).
156. M. Slámová, M. Karlík, F. Robaut, P. Sláma, and M. Véron, *Mater. Charact.* **49**, 231 (2002).
157. M. Masoumi, F. Zarandi, and M. Pegguleryuz, *Mater. Sci. Eng. A* **528**, 1268 (2011).
158. N. Tang, M. P. Wang, H. F. Lou, Y. Y. Zhao, and Z. Li, *Mater. Chem. Phys.* **116**, 11 (2009).
159. Y. Wang, S. B. Kang, and J. Cho, *J. Alloys Compd.* **509**, 704 (2011).
160. Z. Liu, S. Xing, P. Bao, N. Li, S. Yao, and M. Zhang, *J. Mater. Sci. Technol.* **26**, 461 (2010).
161. C. A. Santos, J. A. Spim, and A. Garcia, *J. Mater. Process. Technol.* **102**, 33 (2000).
162. P. Málek, K. Turba, M. Slámová, and I. Drbohlav, *Mater. Charact.* **59**, 1046 (2008).
163. R. T. Dehoff, *Metall. Trans. A* (1971).

Chapter 3

Microstructural origin of friction stir processed zone in a magnesium alloy

3.1 Abstract

This study involved edge regions of a friction stir processed (FSP) magnesium alloy (AZ31). Interleaved structures of ultra-fine, of few hundred nanometers, and coarser grains, several microns, were noted. Very short thermal anneals coarsened the former: generating typical micron-sized FSP grains. A model of microstructural development through grain boundary sliding of the ultra-fine grains was proposed. This model explains weaker texture in such grains and the fact that Mg-FSP shear texture did not change by successive passes.

3.2 Introduction

Friction stir welding (FSW) [1], developed in 1991 by The Welding Institute (TWI), has gained prominence over the last two decades. Friction stir processing (FSP), which is a variation of FSW, can be used for microstructure and texture modifications of monolithic metals and alloys [2]. Although, FSW/FSP have been put into practical applications, the underlying mechanisms for microstructural evolution, are still debated [3–10]. Severe plastic deformation plus static/dynamic aspects of annealing (namely: recovery, recrystallization and grain coarsening [11]) are typically attributed to the formation of equiaxed grains of several microns in size.

There are interesting examples of ‘freezing’ the original (FSP/FSW) stir zone microstructures. Fonda *et al.* [5] and Prangnell and Heason [6] performed quenching experiments on AA 2195: stopping the tool and immediately quenching the workpiece, but with tool still embedded. The section studied [5,6] was parallel to the sample surface, and microstructures were investigated ahead as well as behind the rotating tool. Original grains were sheared into thin layers circumferential to the tool, with micron-sized equiaxed grains developing at grain boundaries between the sheared grains. As the tool approached this mixed structure, the fine grain regions completely consumed the sheared grains. A striking observation of extremely fine grains during FSP of AA 7075 was made by Su *et al.* [7]. The sample was very rapidly quenched, with *the tool being extracted* just before the quenching (in dry ice and methanol). TEM observations, on sections parallel to the tool axis, revealed presence of ultra-fine (100-400 nm) grains next to the original tool surface. The grains coarsened visibly as the relative distance from the tool surface increased: 0.8 and 1.5 micron average grain sizes at respective distances of 0.3 and 3 mm. Considering the time involved in the tool movement, these distances correspond to 0.15 and 1.5 s respectively. This study [7] clearly showed extensive post-deformation grain coarsening.

Magnesium alloys, even with micron-sized grains, are known to exhibit high strain rate superplasticity. For example, AZ31 with an average grain size of 16 micron was reported [12] to demonstrate 160% elongation during 673 K 10^{-2} s⁻¹ tensile tests. Given the micron-sized grains and the very high strain rates of the FSP, it would seem unlikely that grain boundary sliding/superplasticity could be occurring. However, if the ultra-fine grains, as reported by Su

et al. [7], are present during FSP, bands of such grains could be undergoing faster deformation with strain concentration. The mechanism for this postulated higher strain rate would seem to be that of superplasticity [13], with grain boundary sliding accommodated slip and/or diffusion. Such flow, unlike dislocation slip as the dominant shear process, leads to lower evolution of texture [12]. The model of fine-grained superplasticity, at the shear rates and operating temperatures of FSP and FSW, is much more plausible if the operating grain size is in few hundred nanometers than if it is an order of magnitude larger. The hypothesis of FSP occurring, after nanometer-sized equiaxed grain structure has been produced by the mechanisms described by [5,6], would fit with the surprising observation by earlier work [14] that the relatively weak shear texture developed by the first FSP pass was not strengthened by subsequent passes. In order to gain more insights into this idea, detailed study on the microstructure of the Mg-FSP was carried out.

3.3 Experimental methods

The present study investigated the grain structures at the edge of the stir zone. Such a region should have had the fastest cooling and is hence expected to undergo little post-deformation thermal coarsening. Hot rolled (6 mm thickness) AZ31 magnesium alloy (chemical composition listed in table 3.1) was friction stir processed using a conical tool. AISI 4143 tool (of Rockwell ‘C’ hardness of 55) had a shoulder diameter of 18 mm, with 6 and 4 mm as the upper and lower diameter of the conical section respectively. A tilt angle of 3° (with respect to the vertical axis), rotational and translational speeds of 1200 RPM and 100 mm/min were used. The processing [14] was done in the ambient condition. Small samples were taken from the edge region of the processed zone. These were on the advancing side and near the edge of the earlier tool passage. This region was strategically selected: as it had highest cooling rate and expected tool passage was for the shortest time duration. Thus the microstructures of the edge regions are expected to mimic a “self quenching” experiment. A combination of micro-focus X ray diffraction (μ FXrD), optical microscopy (OM), electron backscattered diffraction (EBSD), transmission electron microscopy (TEM) and pico-hardness were used for detailed characterization. Standard metallography, with sub-micron colloidal silica polish, was employed. All samples were ion-milled (Ar^+ ion in a GatanTM PECS 682) at 6 keV with 70° tilt. A BrukersTM D8 Discover, with micro-source (~50 μm spot size) and area detector (Vantec 500TM), was used for μ FXrD. Optical microstructures were

obtained from a ZeissTM Axio Imager unit. EBSD measurements were made on a FeiTM Quanta 3d-Feg (field emission gun) SEM (scanning electron microscope) and TSL EDAXTM EBSD system. Pico hardness was measured, at identified regions, with HysitronTM PI 87 system operated at 100 μ N load. For site-specific TEM sample preparation, a similar SEM with a Kleindiek nanotechnikTM in-situ system was used. For the details of the TEM sample preparation, the reader may refer [15]. TEM observations were made on FEITM Tecnai G2 T20 TEM at 200 keV operating voltage.

Table 3.1: Chemical composition (in wt% alloying elements) of the AZ31 Magnesium alloy [14].

Mg	Al	Zn	Mn	Ca	Si	Cu
Bal.	2.5-3.5	0.6-1.4	0.2-1.0	0.04	0.1	0.01

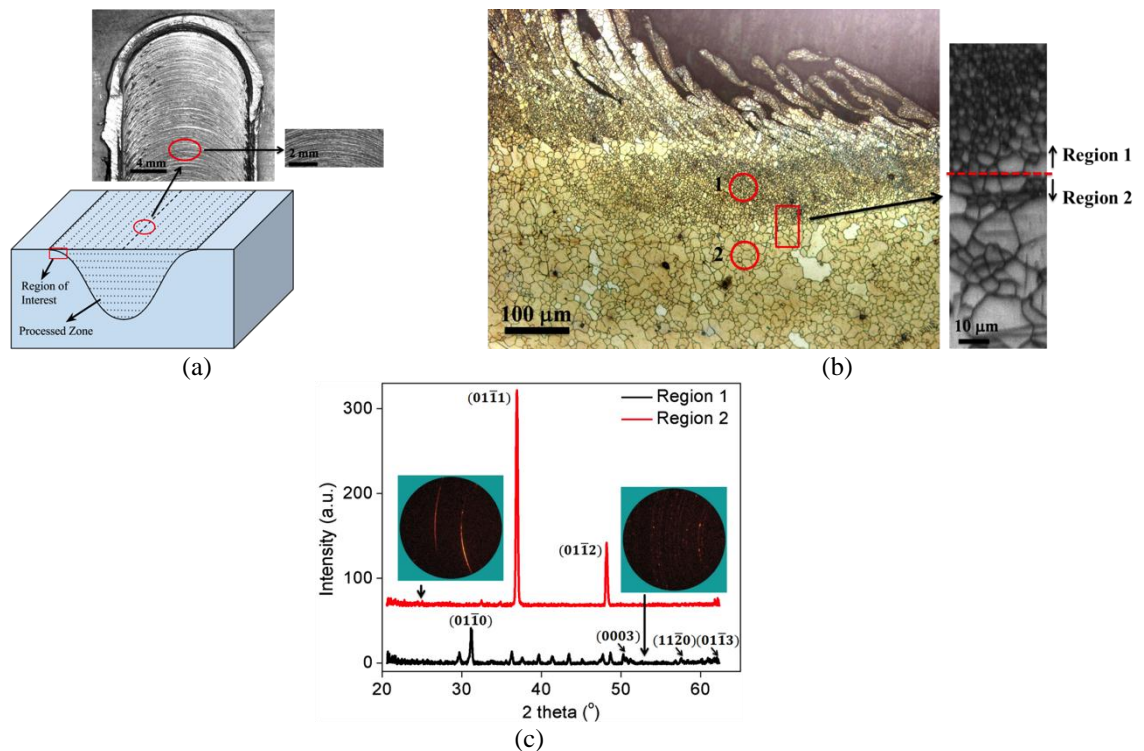


Figure 3.1: a) Schematic and top view of the friction stir processed zone. Region of interest is highlighted. b) Optical micrograph of the edge region showing presence of fine (region 1) and coarse (region 2) grains. Corresponding EBSD, in image quality (IQ) map, shows visible difference in the grain size. c) μ FXrD, in both two and one dimensional representation, for the regions 1 and 2.

3.4 Results and discussion

Figure 3.1a shows the schematic of the processed zone and the region of interest where further characterization was performed. Stereo micrographs captured the appearance of wavy irregular surface: the so-called onion rings [16]. It is to be noted that an onion ring spacing of 100/1200 mm/revolution (or 83 μm) is expected. A similar value was estimated from the stereo-images. Optical microstructure, figure 3.1b, revealed further details. Similar to a typical machining operation, the structure indicated chip formation. It also showed presence of coarse (region 2) and fine (region 1) grains. This was revealed effectively in the EBSD. Peak profiles of the region 1 (fine grains) were broader but with multiple peaks, while coarser grains (region 2) appeared to contain fewer peaks of sharper profiles. The fine and coarse grains co-existed or even interleaved (especially at the edge of a FSP specimen). This appears to be somewhat similar to the mixed microstructures reported in the aluminum studies previously discussed [5,6]. The mixed microstructure is shown in the EBSD map of figure 3.2a. Bands of ultra-fine grains typically had lower image quality (IQ), see figure 3.2b. IQ represents the number of detected Kikuchi bands. Increased inelastic scattering from the presence of dislocations or grain boundaries is known [17] to reduce the IQ. Bands of the low IQ ultra-fine grain also had higher misorientations. This is shown in figure 3.2c as a map of kernel average misorientation or KAM values. Average misorientation between any pixel point and its neighbors (six in case of the hexagonal grid used) is considered as KAM, provided any of these misorientations do not exceed 5° . It was clear, see figure 3.2d, low IQ (ultra-fine grained) regions had significantly higher KAM with large standard deviations around the estimated KAM distributions. It needs to be noted that both low/high IQ (ultra-fine/coarse grains) had qualitatively similar textures: typical location dependent shear texture [14] of the FSP/FSW. They, however, had significant quantitative differences in texturing. The latter was estimated as texture index ($\int f(g)^2 dg$ where $f(g)$ is the ODF intensity) [18] values. Respective texture indices were only 8 for the ultra-fine (370 nm average grain size) and nearly double (15) for the coarse (5195 nm) grain structures (figure 3.2e).

Further characterization of the regions were attempted by site specific TEM [15] and pico-hardness. As shown in figure 3.3a, the low IQ regions appeared as strain localizations. These contained very fine grains (average grain size of 200 nm). They often had grain interior dislocation substructures and almost always shared high angle boundaries with their

immediate neighbors. The latter became apparent through the selected use of convergent beam Kikuchi. Grain boundary misorientations exceeding 15° were estimated through TSL-ACT™. Finally site-specific pico-indentations showed a much higher hardness (700-920 MPa) of the low IQ fine grained regions than their coarse grained counterparts (250-700 MPa), see figure 3.3b. The higher hardness reflects the mechanical properties at room temperature. At the elevated temperatures of FSP, however, the ultra-fine grains should be able to deform more easily by grain boundary sliding [13,19].

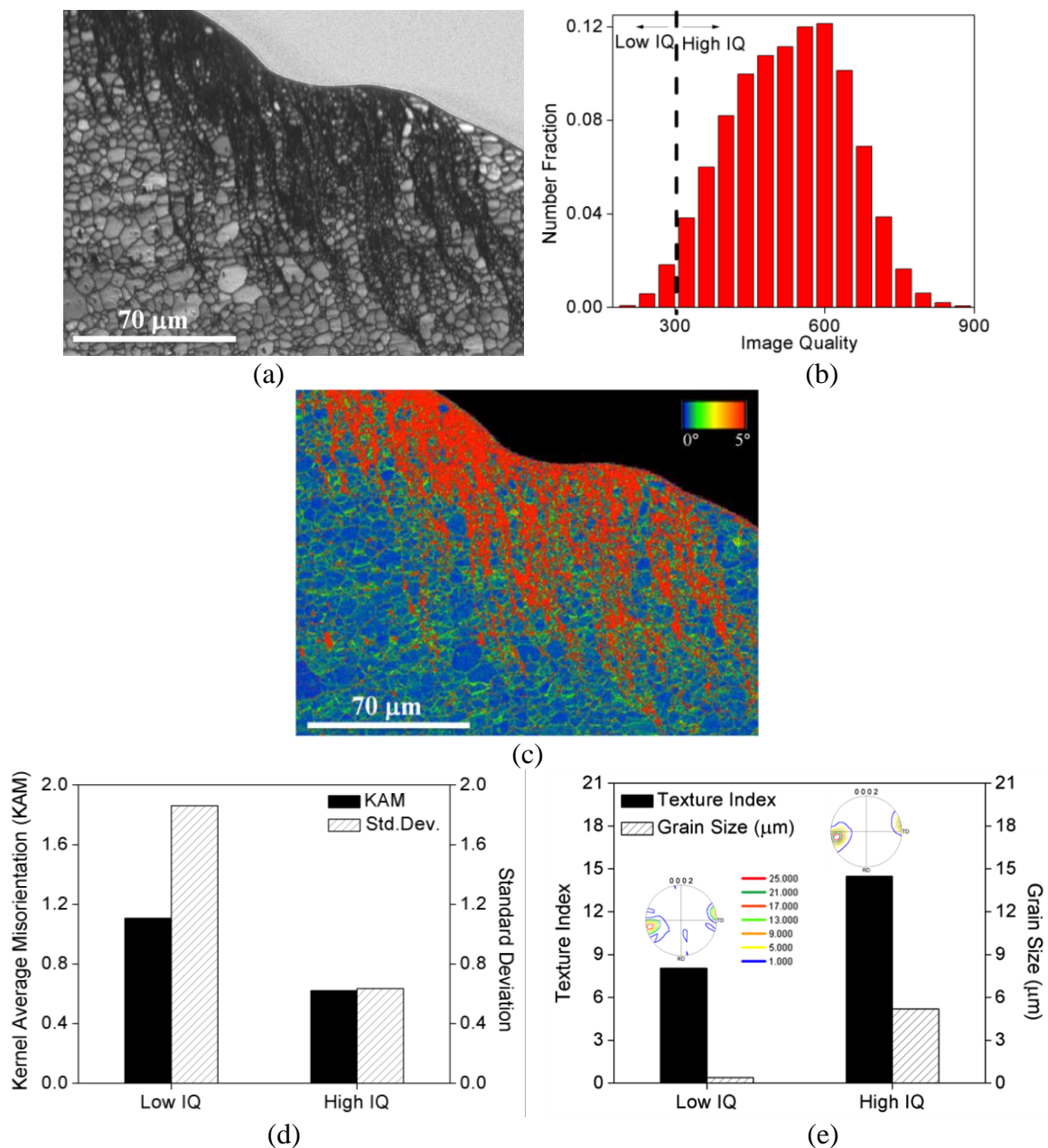


Figure 3.2: a) EBSD image quality (IQ) map showing co-existence of the fine-coarse interleaved grain structures. b) Fine grains typically had low (<300) IQ. c) They also had

higher misorientation: as shown in the map of kernel average misorientation (KAM). d) Average KAM values, and the standard deviations of the KAM distributions, are indicated for the low and high IQ regions. e) Also included are the texture index ($\int f(g)^2 dg$ where $f(g)$ is the ODF intensity) and average grain size of the respective regions.

In order to test the idea that the ultra-fine, few hundred nanometer, grains (figure 3.3a) could rapidly coarsen, brief thermal anneals were carried out. Controlled thermal treatments were given to the apparent bi-modal grain structures in a DIL805A/D™ dilatometer. Even few seconds annealing (at 623 K and 723 K), and fast quenching, showed visible competitive coarsening. Su *et al.* [7], as noted above, observed very rapid grain coarsening in their observation of the ultra-fine grains seen immediately behind the rotating tool. This is a different process from the coarsening observed here in a mixture of ultra-fine and coarser grains. However, both studies indicate that post-coarsening microstructural observations hide the original grain structure present in the rapidly deforming regions during FSP/FSW.

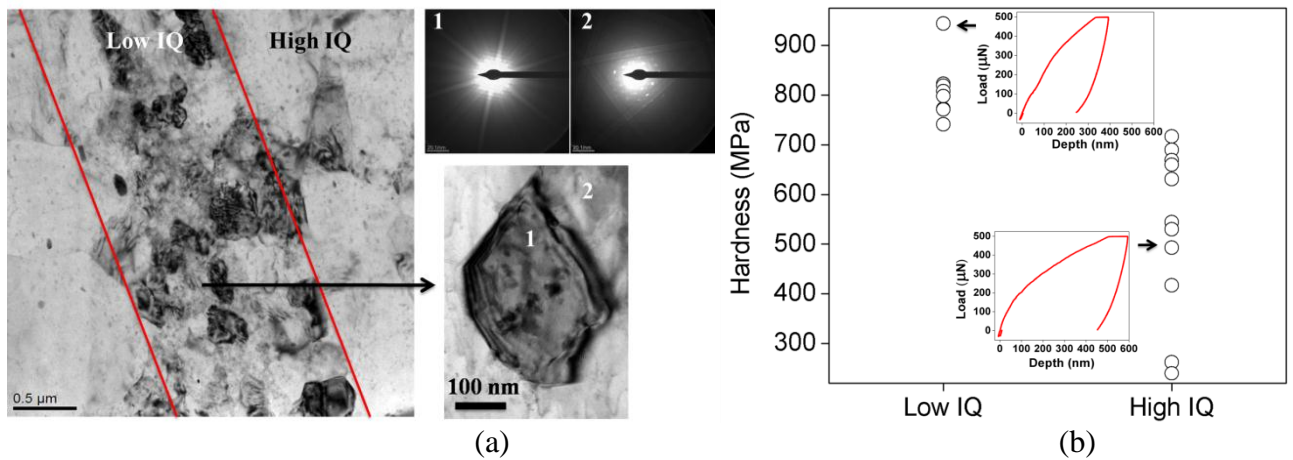


Figure 3.3: a) Site specific transmission electron microscopy of the low-high IQ or fine-coarse interleaved structure (as in figure 3.2a). Low IQ regions appeared (marked with appropriate straight lines) as possible strain localizations in TEM imaging. It contained grains of few hundred nm. These were almost always surrounded by high angle boundaries (as indicated by transmission Kikuchi diffractions). (b) Pico-hardness of the low and high IQ regions.

3.5 Conclusions

On the basis, of the analysis of prior studies, notably [5–7,14] it is proposed that:

- i) As shown by Fonda *et al.* [5] and Prangnell and Heason [6], the equiaxed grain structure typical of FSP/FSW develops by first shearing of the original coarse grain structure to thin circumferential bands. Then the equiaxed grains develop at the high angle boundaries between such layers.
- ii) However, it is proposed that the 2-4 μm grain size of these equiaxed grains result from rapid grain coarsening from much smaller equiaxed grains during either unquenched FSP or even slower quenching with the tool in place. Both Su *et al.* [7] and the present study find grains of an order of magnitude smaller than those usually reported [5,6].
- iii) If the grains are only a few hundred nanometers in size, then even with the high strain rates of FSW/FSP the deformation may be accommodated by grain boundary sliding. Thus grain boundary sliding or superplasticity becomes a potential FSP/FSW deformation mechanism.
- iv) This model for superplastic deformation in FSW/FSP is supported by the texture measurement reported here and in the earlier study [14], where it was found that successive FSP passes did not strengthen the shear texture.
- v) Mixed microstructures of aluminum FSP [5,6] showed fine grain structures surrounded by un-recrystallized bands. This is in contrast with the interleaved ultra-fine and coarse grained structures observed in the Mg-FSP. This difference is likely to reflect the greater ease of dynamic recrystallization in Mg than in Al alloys [11].

It is of course clear that this new hypothesis requires much more detailed evaluation before it can be acceptable as a viable model for microstructure development during FSP/FSW. Such studies will, for example, need to study rapid quenching during FSP as carried out by Su *et al.* [7], with tool withdrawal before quenching to give as fast a cooling rate as possible. This needs to be combined with the sectioning methods of Fonda *et al.* [5] and Prangnell and Heason [6]: to look at section parallel to the surface, ahead of as well as behind the rotating tool. They are required for both aluminum and magnesium alloys.

References

1. R. S. Mishra and Z. Y. Ma, *Mater. Sci. Eng. R Reports* **50**, 1 (2005).
2. Z. Y. Ma, *Metall. Mater. Trans. A* **39**, 642 (2008).
3. T. R. McNelley, S. Swaminathan, and J. Q. Su, *Scr. Mater.* **58**, 349 (2008).
4. K. V. Jata and S. L. Semiatin, *Scr. Mater.* **43**, 743 (2000).
5. R. W. Fonda, J. F. Bingert, and K. J. Colligan, *Scr. Mater.* **51**, 243 (2004).
6. P. B. Prangnell and C. P. Heason, *Acta Mater.* **53**, 3179 (2005).
7. J. Q. Su, T. W. Nelson, and C. J. Sterling, *Mater. Sci. Eng. A* **405**, 277 (2005).
8. K. Oh-ishi, A. P. Zhilyaev, and T. R. McNelley, *Metall. Mater. Trans. A* **37A**, 2239 (2006).
9. U. F. H. R. Suhuddin, S. Mironov, Y. S. Sato, H. Kokawa, and C. W. Lee, *Acta Mater.* **57**, 5406 (2009).
10. J. Q. Su, T. W. Nelson, R. Mishra, and M. Mahoney, *Acta Mater.* **51**, 713 (2003).
11. F. J. Humphreys and M. Hatherly, *Recrystallization and Related Annealing Phenomenon*, Second Edition (Elsevier, 2004).
12. R. Panicker, A. H. Chokshi, R. K. Mishra, R. Verma, and P. E. Krajewski, *Acta Mater.* **57**, 3683 (2009).
13. M. F. Ashby and R. A. Verrall, *Acta Mater.* **21**, 149 (1973).
14. A. Tripathi, A. Tewari, N. Srinivasan, G. M. Reddy, S. M. Zhu, J. F. Nie, and I. Samajdar, *Metall. Mater. Trans. A* Submitted.
15. R. M. Langford and C. Clinton, *Micron* **35**, 607 (2004).
16. S. H. C. Park, Y. S. Sato, and H. Kokawa, *Metall. Mater. Trans. A* **34**, 987 (2003).
17. A. J. Schwartz, M. Kumar, and B. L. Adams, *Electron Backscatter Diffraction in Materials Science*, Second Edition (2000).
18. O. Engler and V. Randle, *Introduction to Texture Analysis Macrotexture, Microtexture and Orientation Mapping*, Second Edition (2010).
19. T. G. Langdon, *Metall. Trans. A* **13**, 689 (1982).

Chapter 4

Microstructural evolution during multi-pass friction stir processing of a magnesium alloy

4.1 Abstract

A commercial magnesium alloy was processed through multi-pass and multi-directional (unidirectional, reverse and transverse tool movements) friction stir processing (FSP). Based on the FSP location, the dominant prior-deformation basal texture was shifted along the arc of a hypothetical ellipse. The patterns of deformation texture developments were captured by visco-plastic-self-consistent (VPSC) modeling with appropriate velocity gradients. The simulated textures, however, had two clear deficiencies. The simulations involved shear strains of 0.8-1.0: significantly lower than those expected in the FSP. Even at such low shear, the simulated textures were significantly stronger. Microstructural observations also revealed presence of ultra-fine grains with relatively weak crystallographic texture. Combinations of ultrafine grain superplasticity followed by grain coarsening were proposed as the possible mechanism for the microstructural evolution during FSP.

4.2 Introduction

Though recent years have seen increasing interest [1–4] in magnesium (Mg) alloys, their applications remain ‘limited’ [2–5]. Restricted formability of Mg has been the key issue [4,6–8]. Plastic deformation, and hence formability, of hexagonal metallic materials strongly depends on the crystallographic orientations [9–11]. Availability of only basal slip limits the room temperature ductility and formability of Mg alloys [6]. It also restricts possible modifications to deformation textures under an imposed strain mode [12–14]. Conventional thermo-mechanical processing, namely plane strain compression (PSC) and recrystallization annealing [12,13,15–17], fails to alter the strong basal (0002) texture. It needs to be noted that near-basal texture is undesirable for Mg formability [9–11].

Ductility and hence formability improvements in magnesium were sought through alloying with rare earth metal(s) [18–20], warm working [21,22] and special forming techniques with non-PSC strain mode [23–27]. Severe plastic deformation, equi-channel angular extrusion [23] and friction stir processing (FSP) [28,29], are examples of such non-PSC processing with clear possibilities of deformation texture modifications.

FSP was developed from FSW (friction stir welding) [30,31]. In FSP/FSW, an appropriate [29,32–39] rotating tool provides localized deformation. The deformation is expected to be simple shear [40,41]. The microstructural refinement is caused by the imposed deformation or velocity gradient [31,42,43]. Heating of the work piece, from friction during plastic deformation [28,44], is also important. The temperature in the work-piece is expected to determine [29,31,45] the magnitude and mechanisms of microstructural refinement. For example, use of appropriate heat sinks was reported [46] to create sub-micron or even nanometer sized ultra-fine grains. There have been debates [40,47–49] on the possible roles of shear deformation, dynamic recrystallization and recovery in FSP.

In a recent publication [50], the presence of ultra-fine (200 nm) grains during Mg FSP was shown (Chapter 3). Even a brief thermal treatment was shown to coarsen such grains to several microns in size. The coarser grains were softer and had stronger texture. It was proposed that the large FSP-shear was accommodated by grain boundary sliding of the ultrafine grains, while post-FSP grain coarsening defined the final micron-sized grain

structures and the crystallographic texture. Two arguments were used to support the proposed model of ultrafine grain superplasticity: (i) ultra-fine grains had very weak texture and (ii) Mg-FSP shear texture did not change with successive passes. The experimental evidence for (i) was provided in reference [50], while the present manuscript investigates (ii) and deliberates on a possible model for FSP/FSW microstructure evolution.

4.3 Experimental methods and simulation details

4.3.1 Experimental methods

Commercial AZ31 (chemical composition listed in table 3.1) was provided in the hot rolled condition. This was then subjected to friction stir processing (FSP). The tool and work-piece geometries are shown in figure 4.1a. AISI 4143 tool steel (Rockwell 'C' hardness of 55) was used as the tool material. The tool (see figure 4.1a) had a shoulder diameter of 18 mm, followed by a conical pin with 6 and 4 mm as the upper and lower pin diameters respectively. The FSP tool was tilted at approximately 3° with respect to vertical axis, and was given respective rotational and linear speeds of 1200 RPM and 100 mm/min. Though literature [24,51] on Mg FSW provides 500-700 RPM and 3.4-5.9 mm/s speed, our initial trials achieved consistent and defect-free processing at these parameters. Multi-pass FSPs were performed, without any significant time gap and with essentially 100% overlap on the previous processed region. Though most of these FSPs were conducted in air, a few FSPs were also performed under water. The latter was essential in capturing the possible role of post-FSP grain coarsening. Processing parameters were otherwise kept identical for all the FSPs. Figures 4.1b, 4.1c and 4.1d describe the tool movements (unidirectional, reverse and transverse) and the sampling strategy. Two types of samples were studied. Samples from 2 ± 2 mm from the top surface were taken at locations (figure 4.1b) p1-p5, covering the advancing to retreating side. The distance from the top was maintained to minimize the role of the pin-shoulder. Additional cross-sectional samples were also obtained at advancing side (AS1/AS2), center (C1-C3) and retreating side (RS1/RS2), see figure 4.1b.

Mounted samples were prepared for metallography. Paper polishing was followed by sub-micron diamond and colloidal silica polishing in an automatic polisher: StruersTM Tegrapol. Final polishing was obtained through argon ion in a GatanTM PECS-682 system

operated at 6 keV. For optical microstructures, acetic picral solution (4.2 g picric acid, 20 ml distilled water, 50 ml ethanol and 10 ml acetic acid) was used. For EBSD (electron backscattered diffraction) and X-ray texture, instead of chemical etching plasma cleaning (Gatan™ Solaris) was employed.

Optical microstructures were obtained in a Zeiss™ Axio Imager microscope. The microstructures were analyzed in Image-J™ [52] for grain aspect ratio measurements. As in Eq. (1), grain sizes were measured at different (0°, 45°, 90°, 135°) tilt angle θ (figure 4.1b) for AS2(p1), RS2(p5) and C(p3) for all pass conditions. A_θ represents grain size aspect ratio at tilt angle θ .

$$A_\theta = 4D_\theta \left(\sum_{\theta=0}^{\theta=135} D_\theta \right)^{-1} \quad \text{where } \theta = 0, 45, 90, 135 \quad (1)$$

D_θ is the average grain size measured at a particular tilt angle θ . θ values were taken at 0°, 45°, 90° and 135°.

EBSD measurements were made in a FEI™ Quanta 3D-FEG (field emission gun) SEM (scanning electron microscope) and EDAX-OIM™ EBSD system. Areas of 500 μm by 500 μm were scanned at 0.5 μm step size at different locations (figure 4.1b) of the respective FSP passes (1-4 pass). Beam and video conditions were kept identical between the scans. For data analysis, EBSD data with confidence index (CI: scale of 0-1) greater than 0.1 were taken. CI is the statistical measure of accuracy in automated indexing [53].

For representation of EBSD scans, inverse pole figure (IPF) [54] maps were used. EBSD data were further analyzed for grain size determination. A grain was considered as a region bound by a continuous boundary above 5° misorientation. Assuming circular geometry, grain sizes were estimated. Quantification of in grain misorientation was made using grain average misorientation (GAM). GAM represents average point-to-point misorientation inside a grain. Mathematically, it is defined by Eq. (2) where $(g_i - g_j)$ is the misorientation between two neighboring points of a grain and N is the total such number of possible pairs of neighboring points inside a grain.

$$\text{GAM} = \frac{1}{N} \sum_{i,j} (g_i - g_j) \quad (2)$$

Macro-texture measurements were done at different locations using Panalytical™ X'Pert PRO MRD system. Four incomplete (to a tilt angle of 85°) pole figures (0002), (011̄2), (011̄3), and (112̄4) were measured and plotted using MTEX [55,56]. The relative strength of the crystallographic texture through FSP was quantified as texture index, a scalar parameter indicating relative anisotropy [54].

$$\text{Texture Index (TI)} = \int f(g)^2 dg \quad (3)$$

where $f(g)$ is the ODF intensity and dg is the imposed orientation spread. Site-specific TEM samples were prepared on the focused ion beam system, using a methodology described elsewhere [57]. A FEI™ Tecnai G2-T20 TEM was used at 200 keV operating voltage.

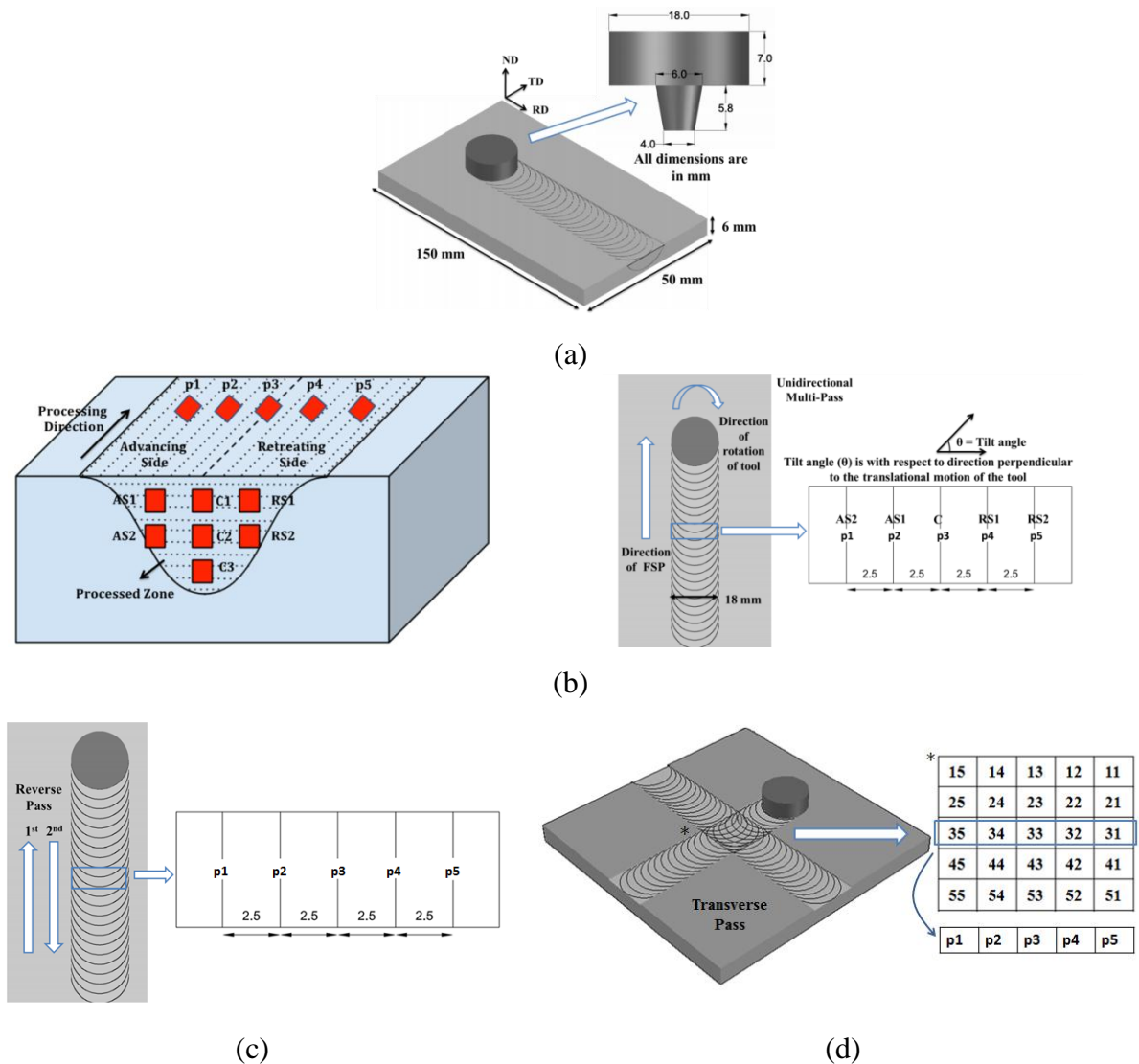
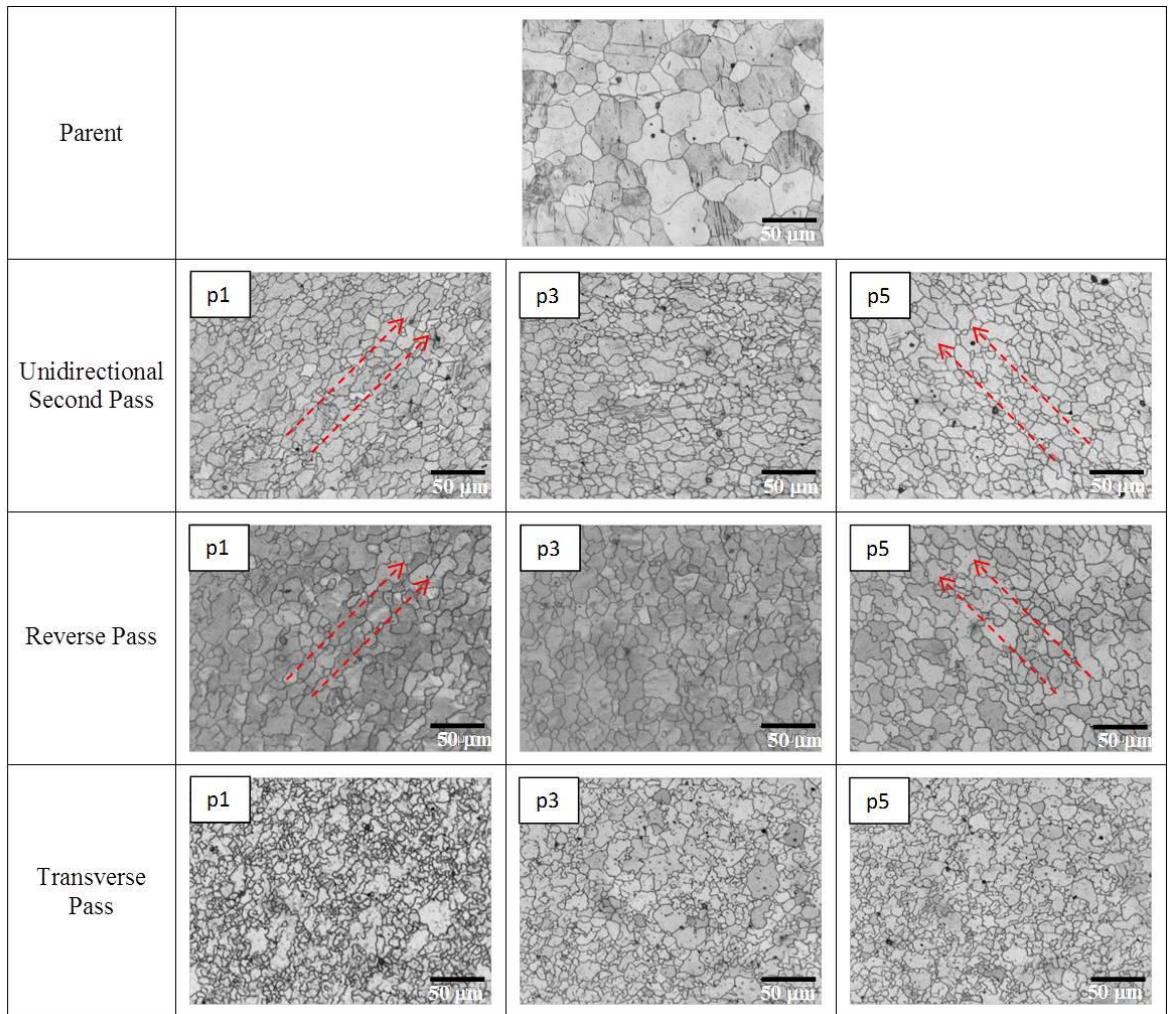
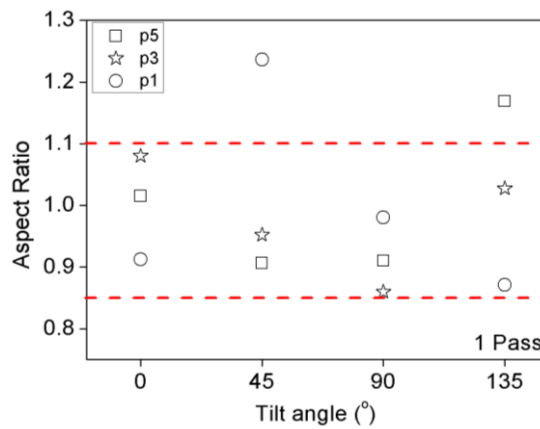


Figure 4.1: Schematic of (a) FSP (friction stir processing) plate and tool. Schematics of multi-pass FSP under (b) unidirectional, (c) reverse and (d) transverse tool movements. In (b)-(d) different locations (p1 to p5) of the FSP (used for characterization) are indicated.

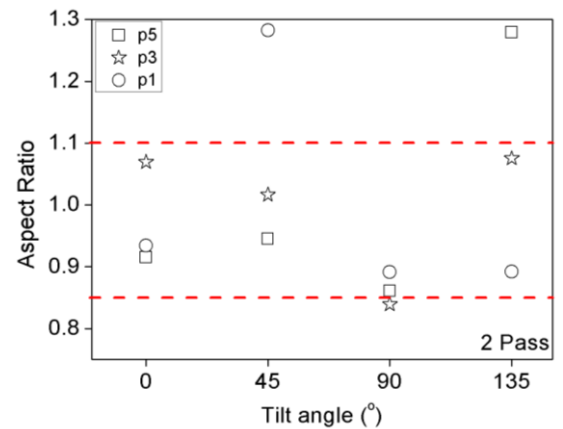
also indicates tilt angle θ for morphological representation; and locations AS (advancing side), RS (retreating side).



(a)



(b)



(c)

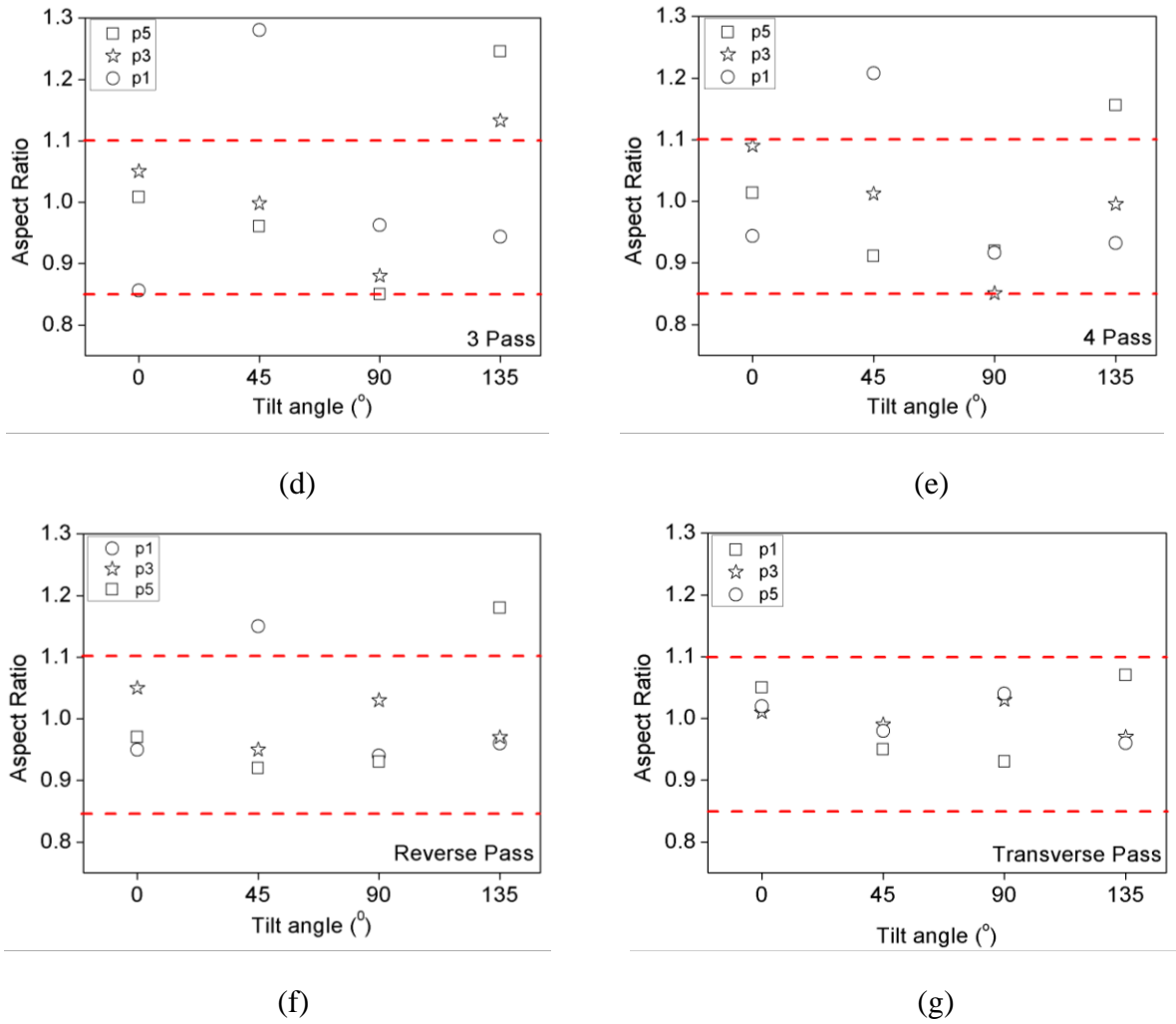


Figure 4.2: (a) Optical micrographs at three different locations (p1, p3 and p5) of the second (unidirectional), reverse and transverse pass FSP. Parent structure is also shown. Aspect ratio (eq. (1)) at different tilt angles (θ : as in figure 4.1b) for different FSP locations for unidirectional (b) first, (c) second, (d) third and (e) fourth pass FSP. Also included are aspect ratios for (f) reverse and (g) transverse tool movements.

4.3.2 Texture simulations

To gain qualitative insights into the nature of the local shears existing at the advancing and retreating sides, a polycrystal plasticity visco plastic self consistent (VPSC) model [58] was used for the prediction of FSP textures. The experimental texture of the sheet before the FSP was descrittized into 500 distinct orientations and were used as input into the VPSC model. The deformation was assumed to be accomodated by basal $\{0001\}\langle 11\bar{2}0 \rangle$, prismatic

$\{10\bar{1}0\}\{11\bar{2}0\}$ and pyramidal $\{11\bar{2}2\}\{11\bar{2}3\}$ slip modes. Critical resolved shear stress (CRSS) values of 9.76 MPa and 12.54 MPa [59] were used for basal and non-basal slip systems respectively. These were selected to represent the material behavior at temperature of 573K (300°C). It is to be noted that temperature measurements, with embedded thermocouples, had shown similar temperatures in the FSP stir zone [44]. Deformation twinning was not considered. No work hardening was considered. The simulations were run using the $n_{eff} = 10$ interaction. Various velocity gradients were imposed when simulating textures at different FSP locations. Further details is given in the later section: results (4.4.2.2 Deformation texture simulations).

4.4 Results

4.4.1 Microstructural evolution

Figure 4.2 collates observations on conventional metallography. As shown in figure 4.2a, FSP led to clear refinement in grain size. The prior-FSP grain size of 46 μm was refined to 7-12 μm after the FSP. Though no clear trend(s) in grain size was apparent with FSP pass, tool movement or location; FSP appeared to enforce morphological texture. As shown in figure 4.2a, grains appeared morphologically oriented in the p1 and p5 locations of unidirectional (figure 4.1b) as well as reverse (figure 4.1c) tool movements. However, no such preference appeared in p3 or under transverse (figure 4.1d) FSP. Grain aspect ratios were calculated (using Eq. (1)) at different tilt angles (θ). As in figure 4.2(b-g), almost all aspect ratios existed within a band of 0.85 to 1.10. Such grains can be approximated as equiaxed. The only exceptions were for $\theta = 45^\circ$ at p1 and $\theta = 135^\circ$ at p5, corresponding to unidirectional and reverse tool movements. Thus these were the FSP locations, independent of the number of FSP passes, where clear morphological orientations were identified. They also coincide with expected [41,60–62] patterns of metal flow. As shown subsequently in this manuscript, relative differences in metal flow or local velocity gradients were critical in establishing the location dependent evolution of crystallographic texture.

Further details on microstructural developments, characterized through EBSD, are summarized in figures 4.3 and 4.4. Figure 4.3 not only confirms the earlier observation on

grain size refinement, it also points out the presence of bimodal grain sizes in several FSP locations. This point is further described later in this manuscript. Figure 4.4 quantifies two aspects of the microstructural evolution. As in figure 4.4a, 48 μm prior-FSP average grain size was refined to 4-12 μm average grains. Grain average misorientation (GAM) also increased (figure 4.4b) from 0.45 to 0.63. However, it is important to note that the so-called water quenched (FSP under water) sample had a significantly smaller grain size and higher GAM at all the FSP locations. The finer grain size under water cooled conditions is compatible with significantly reduced post-FSP grain coarsening. However the smaller grain size might have also resulted from a lower temperature in the metal during the deformation.

Post-FSP microstructures, even for the water quenched specimen, often had an interleaved structure of ultrafine grains (few hundred nanometer) and micron-sized coarser grains. High resolution EBSD and site-specific TEM sample shows this in figure 4.5. Ultrafine grains appeared to exist as strain localizations, and relatively coarser grains of several microns surrounded them.

4.4.2 Development of crystallographic texture

4.4.2.1 Experimental observations

The prior-FSP AZ31 was a textured material (see figure 4.6a). The FSP had two clear effects on the crystallographic texture evolution: pole shift and texture strength. These texture results are presented in this section. As shown in figure 4.6b, all the poles of the unidirectional second pass FSP appeared ‘shifted’. As in figure 4.6c, such ‘shifts’ were identical under progressive FSP passes, and also for FSP processing under water (water quenched). The relative pole shifts were in terms of ND-TD rotations. This is shown, schematically, in figure 4.6d. As shown in the figure, the pole shifts are best captured by the respective angles of R' and ϕ . The final textures did exist around the arc of a hypothetical ellipse (figure 4.6d). The experimentally observed values of R' and ϕ are summarized in table 4.1. As shown in the table, the pre-FSP values of R' of 0.07 were modified to 0.42-0.49. This was both location and pass independent. The ϕ values were, however, location dependent (but independent of the number of passes): 125-136° (for p1), 101-116° (for p2), 82-101° (for p3),

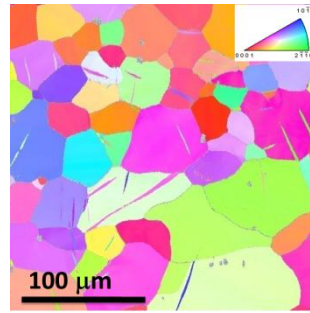
64-73 ° (for p4), and 40-53° (for p5). The relative pole shifts were also observed under reverse tool movement (see figure 4.7a). This was a mirror image of the unidirectional pole shifts. Under transverse tool movement, the picture of the pole shift was more complex (see figure 4.7a), but also evolved a clear pattern.

Table 4.1: Experimentally observed R' and ϕ values (figure 4.6) for the pole figures at different locations (see figure 4.1b)

R' (Normalized to 1.0), ϕ (°)	p1	p2	p3	p4	p5
0 Pass	0.07, 90	0.07, 90	0.07, 90	0.07, 90	0.07, 90
1 Pass	0.42, 125	0.42, 101	0.45, 82	0.44, 64	0.43, 42
2 Pass	0.45, 135	0.47, 116	0.49, 101	0.47, 73	0.47, 43
3 Pass	0.42, 126	0.44, 111	0.42, 97	0.45, 65	0.48, 40
4 Pass	0.42, 136	0.42, 108	0.43, 97	0.44, 73	0.45, 53

As described in Eq. (3), texture index provide a scalar representation of relative anisotropy. The prior-FSP material had a texture index of 13. This was reduced significantly by the FSP, see figure 4.7b. Without speculating on the location, pass or tool movement dependence of the texture randomization, it is worth noting that the so-called water quenched specimen, with the lowest grain coarsening, had the highest randomization of texture.

The measurements of bulk crystallographic texture thus showed a systematic pattern of pole shifts (figure 4.6 and figure 4.7a) and texture strength reduction (figure 4.7b). This was observed at p1-p5 (figure 4.1b): 2 ± 2 mm from the top surface, and also at the cross-section. As in figure 4.8, cross-sectional pole shifts were both location and depth dependent. The depth dependence was most pronounced along the centerline C1-C3. It needs to be noted that past research on Mg FSW had also reported [51,63] similar location and depth dependence of the basal texture. The striking feature of this study is on the consistency of the pole shifts: the fact that the observations did not change with number passes and the imposed cooling rate (as in the case water quenched sample). The systematic pole shifts were also noted (figure 4.7a) for different tool movements. Deformation texture simulations were conducted to capture the patterns of experimental texture developments.



(a)

Position	p1	p3	p5
Unidirectional Second Pass			
Reverse Pass			
Transverse Pass			

(b)

Figure 4.3: EBSD images, in inverse pole figure (IPF) notation, for (a) parent (prior FSP material), and (b) post-FSP different locations (p1, p3 and p5) after unidirectional second, reverse and transverse pass.

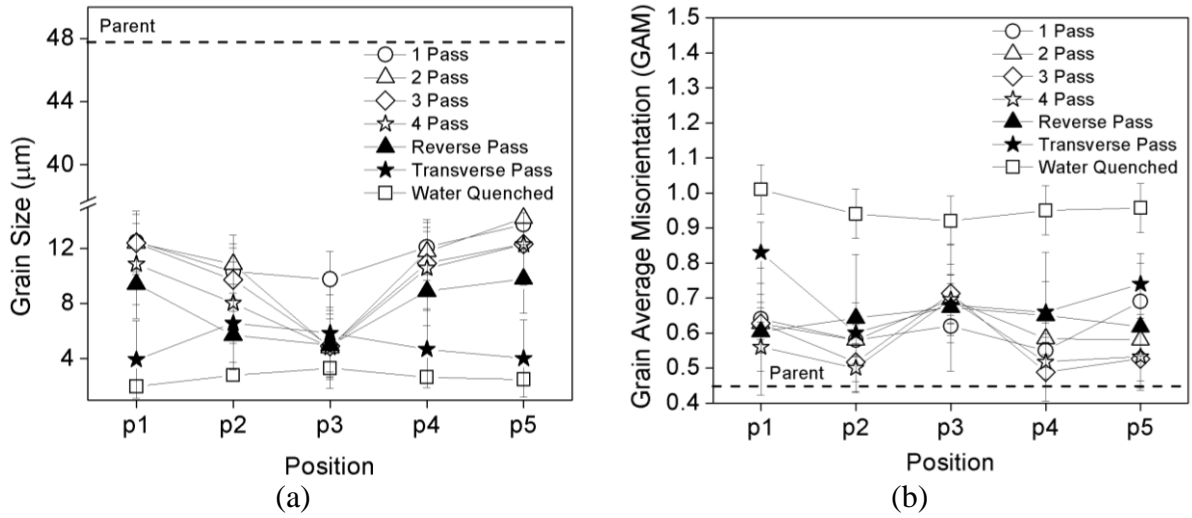


Figure 4.4: Average grain size and (b) grain average misorientation (GAM) at different locations (p1 to p5) after different FSP pass schedules (as in figures 4.1(b)-(d)). Respective values of prior-FSP parent material are shown as dotted line. The data from under water unidirectional 1 pass FSP (water quenched) are included in the figures. Error bars represent standard deviations from multiple EBSD scans.

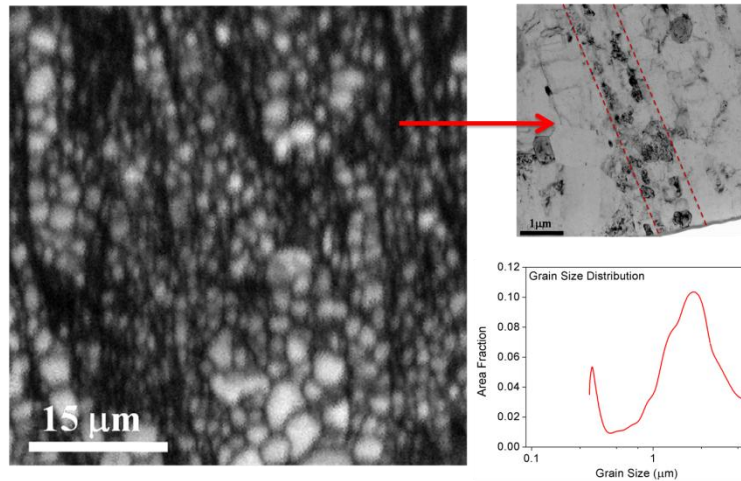


Figure 4.5: EBSD IQ (image quality) map showing bimodal grain size distribution (also included) in the processed zone. Transmission electron micrograph showing ultra-fine grains.

4.4.2.2 Deformation texture simulations

Velocity gradients play an important role in defining the texture developments during FSP or FSW [42,64–66]. The velocity of a particle, in a flow field on an Eulerian reference frame, is defined by the partial derivative of position with respect to time.

$$\mathbf{u} = \frac{\partial \mathbf{x}}{\partial t} \quad (4)$$

Velocity gradient is then derived by taking spatial gradient of the velocity field.

$$\mathbf{L} = \frac{\partial \mathbf{u}}{\partial \mathbf{x}} \quad (5)$$

The flow of the material around the tool during FSP is complex, and difficult to measure experimentally [67]. Past researchers [68,69] had computed the material flow numerically. Arguably, the approximated velocity gradients can be imposed and deformation texture developments explored through simulations [66]. More specifically, the velocity gradient can be written as combination of shearing along slip systems and a rigid lattice rotation.

$$\mathbf{L} = \mathbf{L}^c = \Omega + \sum_{\alpha} \dot{\gamma}^{\alpha} \mathbf{T}^{\alpha} \quad (6)$$

Where Ω is the lattice spin, $\dot{\gamma}^{\alpha}$ is the shear strain rate on the slip system α and \mathbf{T}^{α} is the Schmid factor for that slip system. The velocity gradient (\mathbf{L}) matrix can be decomposed into two parts, one symmetric part (\mathbf{D}) and another, skew symmetric part (\mathbf{W}).

$$\mathbf{L} = \mathbf{D} + \mathbf{W} \quad (7)$$

$$\begin{bmatrix} L_{11} & L_{12} & L_{13} \\ L_{21} & L_{22} & L_{23} \\ L_{31} & L_{32} & L_{33} \end{bmatrix} = \begin{bmatrix} D_{11} & D_{12} & D_{13} \\ D_{12} & D_{22} & D_{23} \\ D_{13} & D_{23} & D_{33} \end{bmatrix} + \begin{bmatrix} 0 & W_{12} & W_{13} \\ -W_{12} & 0 & W_{23} \\ -W_{13} & -W_{23} & 0 \end{bmatrix} \quad (8)$$

It is to be noted that the velocity profile and hence the velocity gradient is a complex function, with position vector as one of its variable [42]. The latter may change depending of

the relative position of the concerned point with respect to the tool. FSW texture developments were successfully attempted [65] using appropriate velocity gradients from a finite element material flow and simple shear as the strain mode.

The present study used VPSC model and imposed different velocity gradients on the parent prior-FSP texture. As summarized in figure 4.9, this resulted in clear pole shifts, and different R' and ϕ values (see table 4.2) on the simulated pole figures. Figure 4.10a shows the simulation results with two independent velocity gradients. These are given below as Eq.(9) and (10), approximating the respective velocity gradients for the advancing (p1) and retreating (p5) side of the unidirectional FSP.

$$\frac{\partial \mathbf{u}(\text{AS}, \text{p1})}{\partial \mathbf{x}} = \begin{pmatrix} 0 & -1 & -1 \\ 0 & 0 & 1 \\ 0 & 0 & 0 \end{pmatrix} \quad (9)$$

$$\frac{\partial \mathbf{u}(\text{RS}, \text{p5})}{\partial \mathbf{x}} = \begin{pmatrix} 0 & 1 & -1 \\ 0 & 0 & -1 \\ 0 & 0 & 0 \end{pmatrix} \quad (10)$$

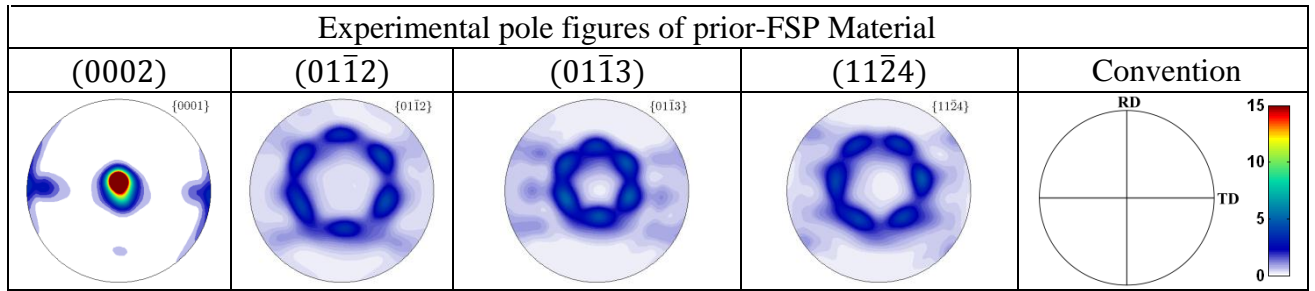
The simulated textures (see figure 4.10a) qualitatively captured the experimental (figures 4.6b and 4.6c) texture developments during multi-pass unidirectional FSP. It is important to note that both p1 and p5 had the same sign of L_{13} , while L_{12} and L_{23} were of opposite sign. These are consistent with expected [41,60–62] material flow on either sides of the tool. Appropriate velocity gradients also captured the pole shifts of the respective FSPs with reverse (figure 4.10b) and transverse (figure 4.10c) tool movements.

The VPSC model and appropriate velocity gradients thus captured, qualitatively, the location dependent pole shifts remarkably well. However, there were serious limitations. As summarized in figure 4.11, the pole shifts were best captured at a von Mises effective strain of 0.8-1.0. Higher strains increased the rotations further and the match with the experimental pole figures disappeared. This appears counter-intuitive as the expected [70] maximum shear in FSP may even approach 40. The simulations, even at the lower imposed shear strains, also led to significantly higher texturing. The simulated textures had 3-5 times the texture indices as that of the experimental ODFs (orientation distribution function).

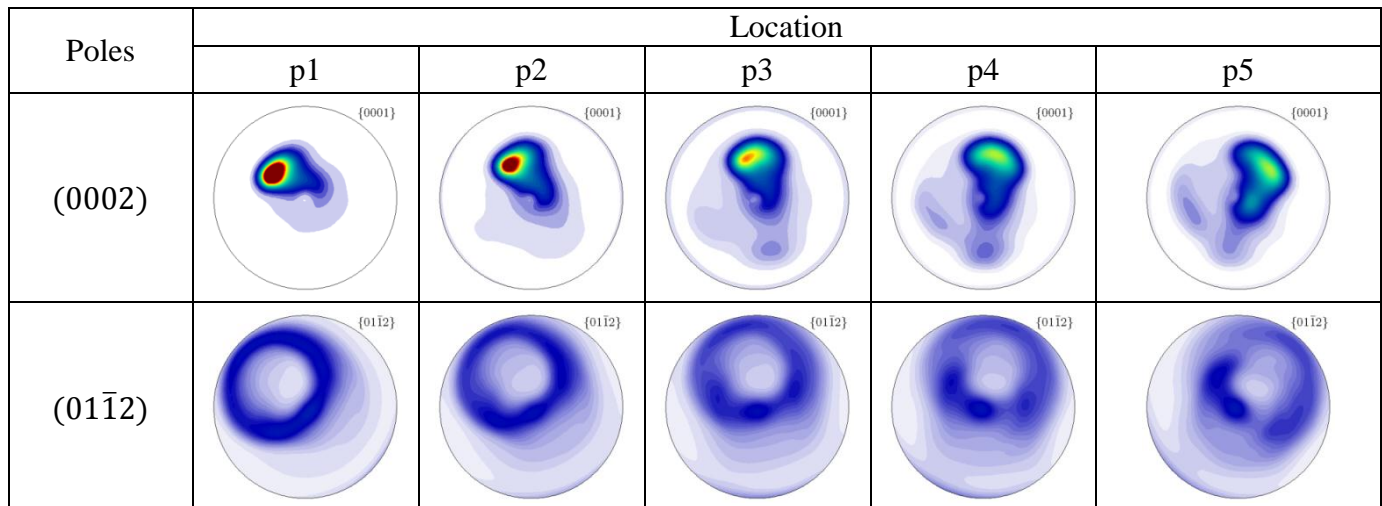
In the next section, deliberation on these results and their impact on the possible mechanisms of the microstructural developments during FSP are made.

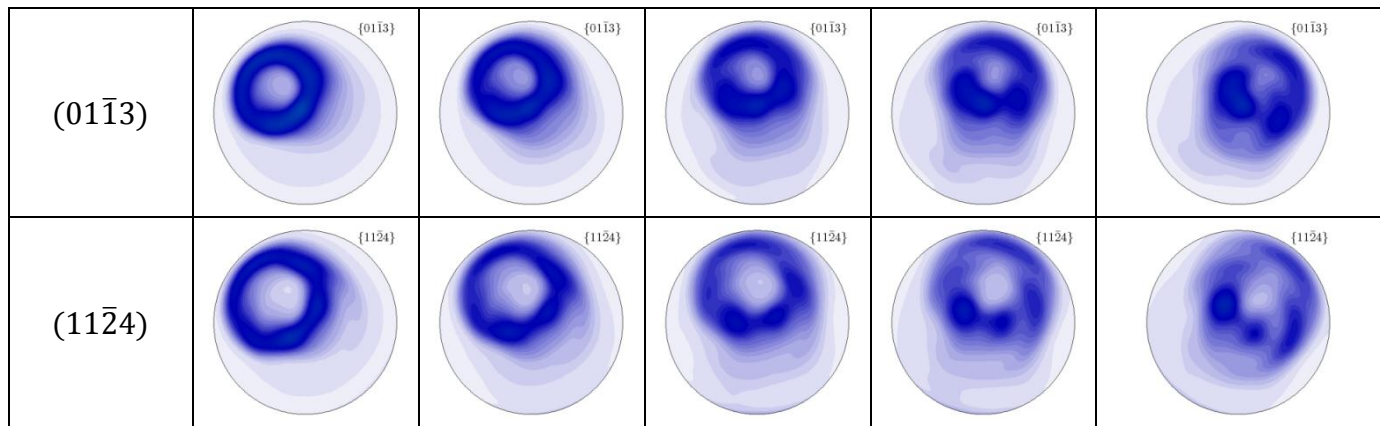
Table 4.2: R' and ϕ values of the simulated pole figures (see figure 4.9) with different velocity gradients and an effective von Mises strain ($\bar{\epsilon}$) of 1.0

R' and ϕ values	$\begin{pmatrix} 0 & -1 & 0 \\ 0 & 0 & 0 \\ 0 & 0 & 0 \end{pmatrix}$	$\begin{pmatrix} 0 & 1 & 0 \\ 0 & 0 & 0 \\ 0 & 0 & 0 \end{pmatrix}$
R'	0.24	0.24
ϕ	131	56
	$\begin{pmatrix} 0 & 0 & -1 \\ 0 & 0 & 0 \\ 0 & 0 & 0 \end{pmatrix}$	$\begin{pmatrix} 0 & 0 & 1 \\ 0 & 0 & 0 \\ 0 & 0 & 0 \end{pmatrix}$
R'	0.07	0.8
ϕ	90	90
	$\begin{pmatrix} 0 & 0 & 0 \\ 0 & 0 & -1 \\ 0 & 0 & 0 \end{pmatrix}$	$\begin{pmatrix} 0 & 0 & 0 \\ 0 & 0 & 1 \\ 0 & 0 & 0 \end{pmatrix}$
R'	0.10	0.12
ϕ	90	110

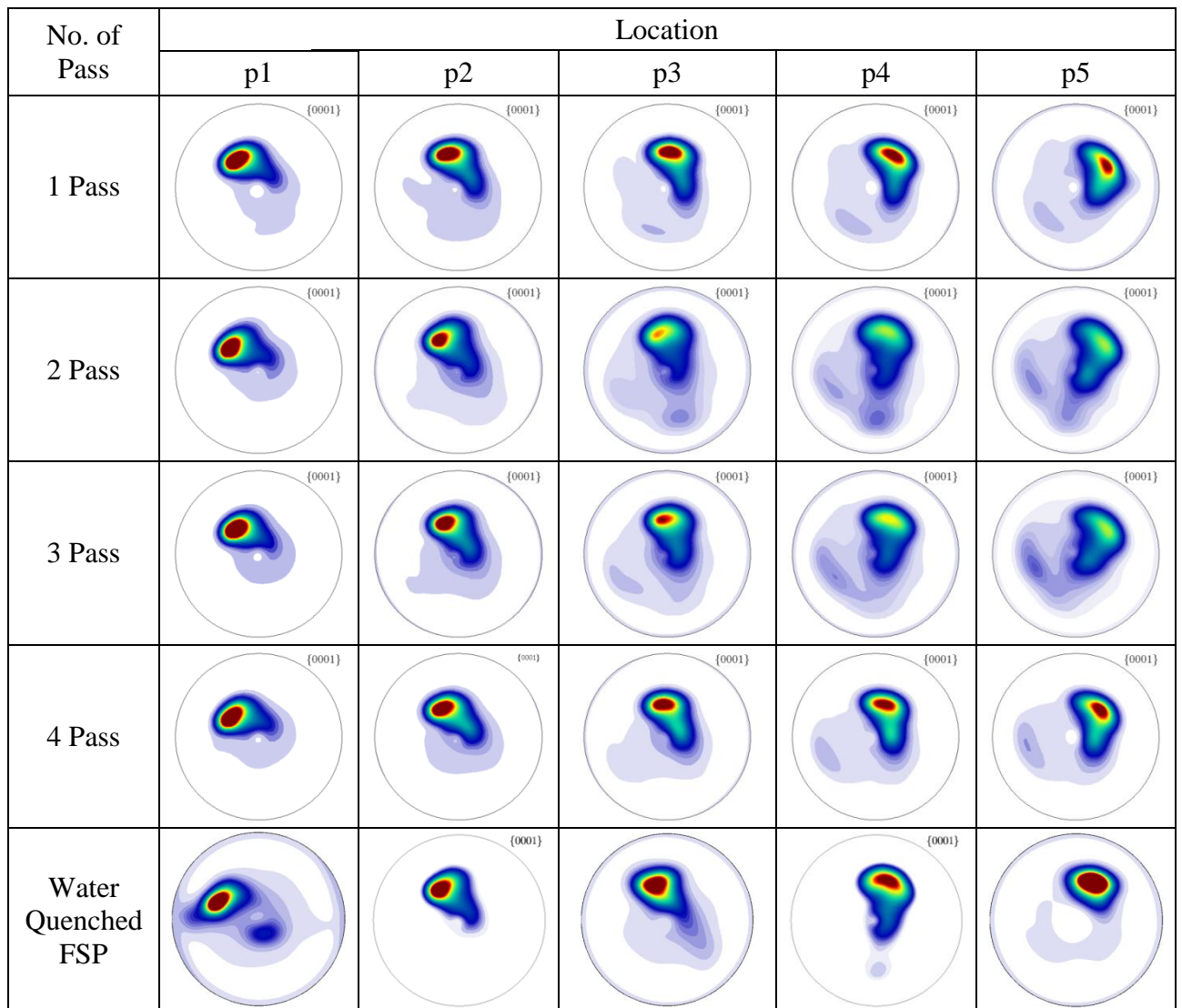


(a)





(b)



(c)

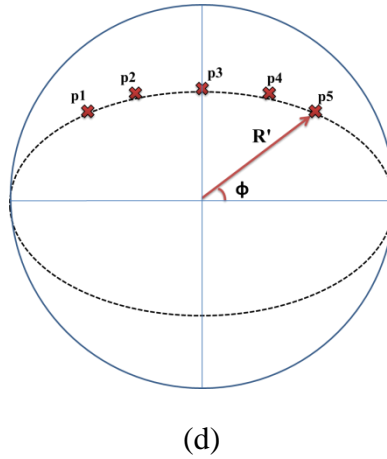


Figure 4.6: Experimental X-ray pole figures of (a) prior-FSP material and (b) at different locations (p1-p5, see figure 4.1b) after unidirectional 2nd pass FSP. In (b), (0002), (01 $\bar{1}$ 2), (01 $\bar{1}$ 3), and (11 $\bar{2}$ 4) pole figures are shown. (c) (0002) (or (0001)) X-ray pole figures at different locations (as in figure 4.1b) after 1-4 unidirectional FSP passes. (c) also includes pole figures from unidirectional 1 pass water quenched (process under water) specimen. Pole figure convention and contour levels (and in (a)) were kept identical. (d) Schematic of location dependent shift of the post-FSP pole figures (as in figures 4.6b and 4.6c).

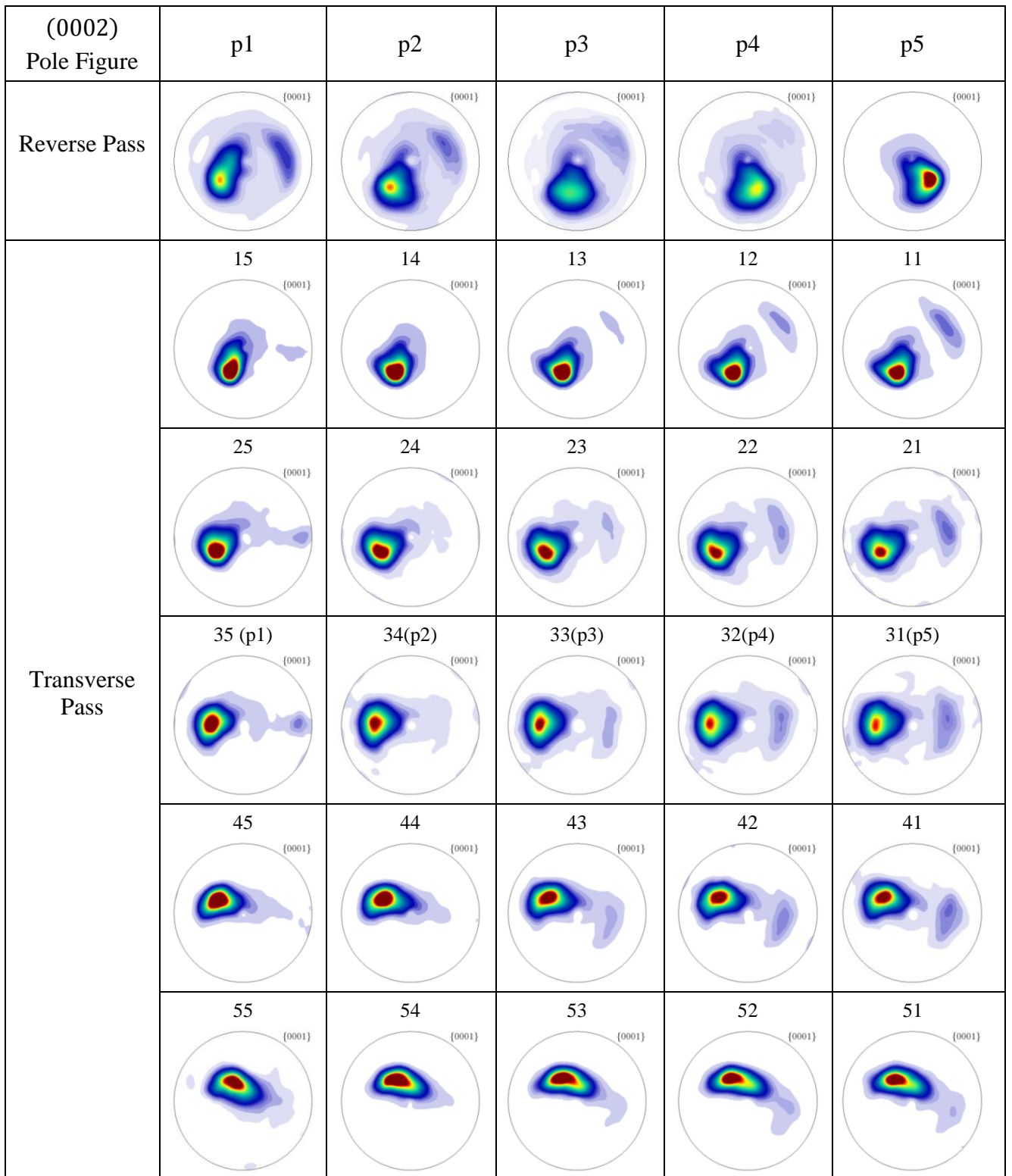
4.5 Discussion

Texture evolution during FSP or FSW has attracted significant scientific interests over last one and half decade. In a 2001 publication, Field *et al.* [41] recognized the presence of sharp spatial gradients in texture. The authors were forthcoming about the ‘tortuous deformation path’ and the fact that this is/was ‘not yet fully understood’. However, they identified aluminum FSW texture as different components of ideal fcc (face centered cubic) shear texture and discussed this in terms of material flow. Park *et al.* [63] showed that FSW of magnesium results in a shifted basal plane texture, whose trace became an ellipsoid. This is exactly what has been highlighted in figure 4.6 of the present study. Schneider and Nunes [71] described the metal flow in FSW as a combination of ‘straight-through’ and ‘maelstrom’ currents. While Fonda and Bingert [72] recognized macroscopic rigid-body rotations of the grains, the latter clearly did not account for the observed texture weakening. Cho *et al.* [64] related FSW texture evolution to the appropriate velocity gradients, and used coupled viscoplastic flow and heat transfer to model the deformation texture developments.

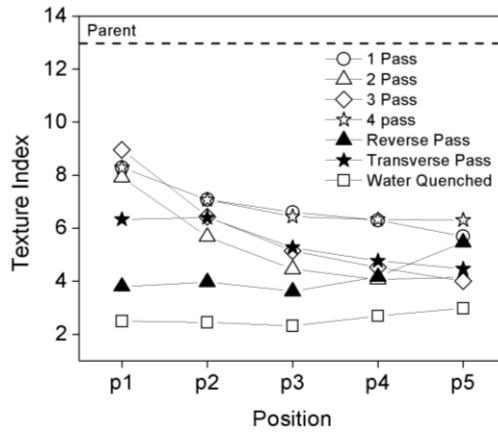
Cho and Dawson [65] also established the importance of local velocity gradients in texture development.

It is thus clear that FSP or FSW textures are attributed to simple shear [40,41], determined by local velocity gradients [64–66]. However, the shear and the corresponding rigid-body rotations may not account for the texture weakening [72]. Grain coarsening is certainly one source of the softening. This is seen in the so-called water quenched sample. This sample had finer grains (figure 4.4a) and higher misorientation (figure 4.4b). Though it also had a somewhat weaker, more random, texture (figure 4.7b), the pole-shifts (figure 4.6c) appeared almost identical. The observed pole-shifts were clearly dependent on the location and depth, but were independent of both the number of passes and the imposed cooling.

As the aim was to document, and then explain, location dependent texture evolution in FSP; observations were restricted to the ‘stir’ zone. However, it may be noted that the HAZ microstructure remained mostly unaffected by the processing: number of passes and the relative tool movement. The HAZ texture had a similar near basal to that of the parent pre-FSP material. Also the HAZ did not show any significant grain coarsening.

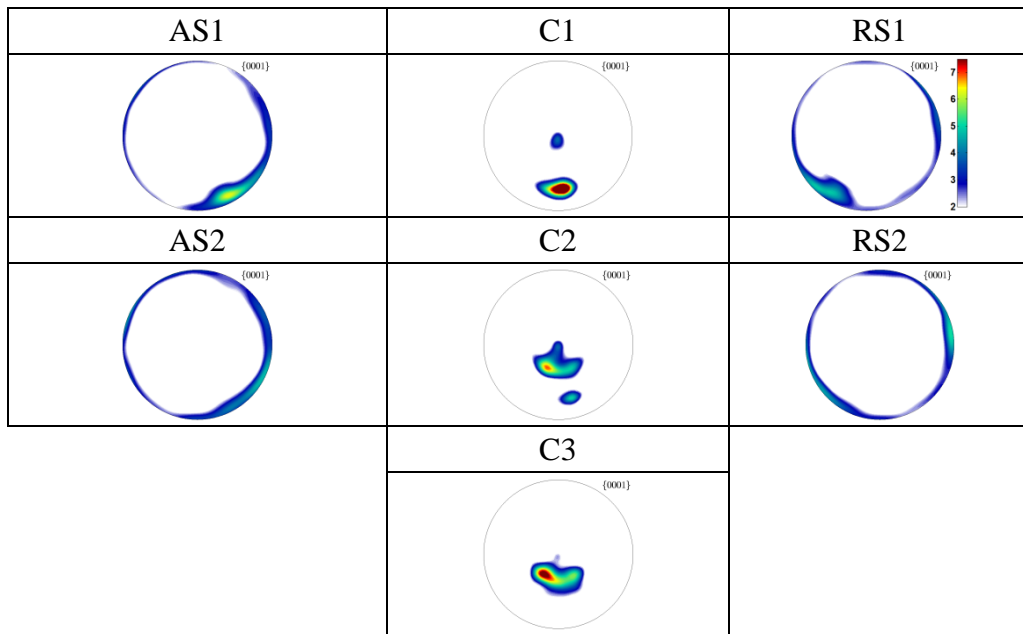


(a)

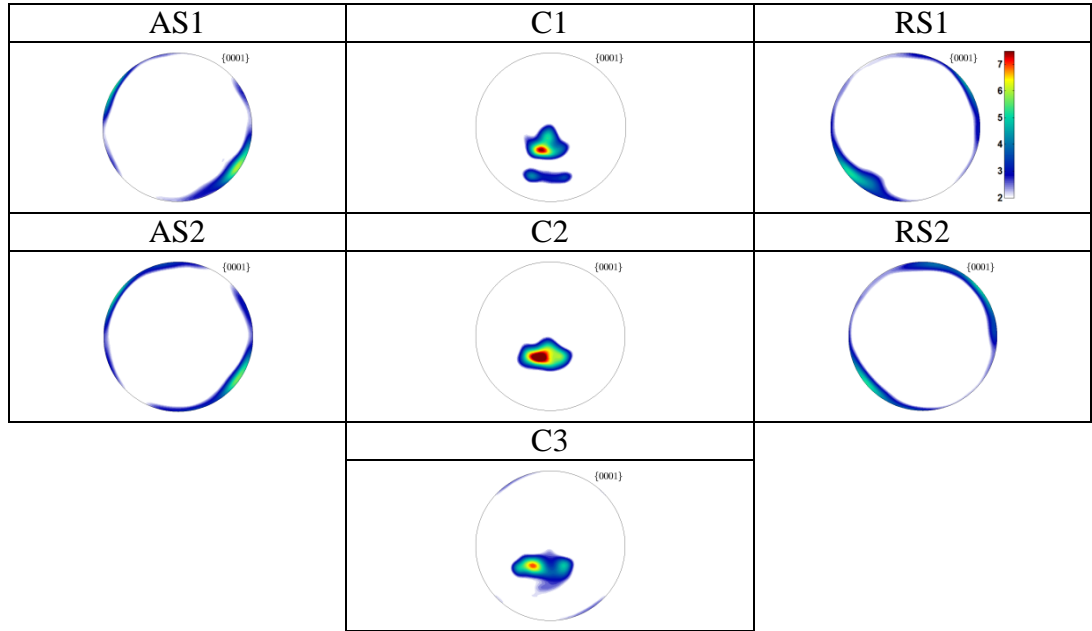


(b)

Figure 4.7: (0002) (or (0001)) X-ray pole figures at different locations (as in figure 4.1c and d) of reverse pass and transverse pass FSP. Pole figure convention and contour levels are same as in figure 4.6a. (b) Texture indices at different locations of the multi-pass and multi-direction FSP. (b) includes data from unidirectional 1 pass water quenched (process under water) specimen.



(a)



(b)

Figure 4.8: Experimental X-ray pole figures (0002) (or (0001)) at cross-sectional locations (see figure 4.1b) locations for unidirectional (a) 1 and (b) 4 pass FSP.

VPSC simulations captured, qualitatively, the location dependence of the pole shifts, see figure 4.10. This is shown schematically in figure 4.12. The near basal parent ‘p’ shifted to p1-p5 on the surface. To minimize effects of tool shoulder, measurements for p1-p5 were taken at 2 ± 2 mm from the top surface. It is clear that deflections at the extreme locations (p1 and p5) were approximated by appropriate velocity gradients (Eq. (9) and (10)). Even at the cross-section, the pole-shifts were consistent. AS1/AS2 and RS1/RS2 were almost identical and could be approached through VPSC. Though C1-C3 showed progressive shifts, changing the velocity gradient appeared to provide an explanation. It is also important to note that VPSC simulations also captured the pole-shifts of more complex tool movements: reverse (figure 4.10b) and transverse (figure 4.10c).

This itself is not a novel contribution. Past research [64–66] had also shown that FSW texture could be modeled with appropriate velocity gradients. However, this manuscript brought out two ‘limitations’ of the texture modeling. Firstly, the observed pole shifts were approached at a significantly lower strain (0.8-1.0 von Mises equivalent strain). Secondly, the extent of texturing was much higher than the experiments. Though Taylor type simulations typically provide a higher texturing [73], 3-5 times higher texture indices in the simulations

cannot be rationalized. The results from crystallographic texture, both experiments and simulations, thus indicate that FSP microstructure evolution cannot be explained solely from shear-induced dislocation slip. This interpretation is greatly strengthened by the experimental result that further FSP passes did not strengthen/modify the weak shear texture.

Optical, EBSD and TEM images, taken from the same location, revealed interesting contrast. The optical grain sizes were, in general, coarser. Optical images are biased by chemical etching. Ultra-fine grain (of few hundred nanometers) cannot be revealed by conventional metallography. EBSD (and TEM) observations on interleaved bi-modal grain structure (see figure 4.5) thus remained 'undetectable' in optical metallography.

This interleaved microstructure was also the topic of the preceding study [50]. It was shown the ultra-fine grains were harder and had lower texture. It was also shown, through controlled thermal treatment, the grain coarsening was almost instantaneous in the fine-grained regions. It is thus proposed that during the FSP an ultra-fine grain structure is developed allowing continued shearing to occur, as in super plastic flow by grain boundary sliding. As the strain rate falls after passage of the tool these fine grains rapidly coarsen to give the micron-sized grain structures almost universally reported [29,30] in both FSP and FSW. In other words, ultra-fine grain superplasticity is proposed here as a plausible deformation mechanism for FSP/FSW.

Plausible ultra-fine grain superplasticity can explain the texture evolution reported in this study. Following stages may be considered. (i) Initial local shear plus appropriate dynamic restoration mechanism(s) (dynamic recovery and recrystallization) created the FSP/FSW texture (the observed pole-shifts) and ultra-fine grain structure. (ii) Further deformation was accommodated by ultra-fine grain superplasticity, which is expected to reduce the texturing [37]. The superplastic deformation model proposed here can also explain the observed consistency of the crystallographic texture in the multi-pass FSP. (iii) Post-FSP microstructure involved grain coarsening, leading to bimodal grain size distributions and increase in texturing. Normal grain coarsening is expected to strengthen, and not alter, the crystallographic texture [73]. If one considers that FSP texture evolved through dislocation slip alone, then a strain of 40 (and much more for multi-pass FSP) should give a greatly strengthened (and significantly modified) shear texture (see figure 4.11). It is hence proposed that the initial shear-induced dislocation slip plus possible dynamic restoration mechanisms

created the ultra-fine grain microstructure and the appropriate texture at the initial stage. Most of the subsequent strains were then accommodated by the ultra-fine grain superplastic deformation.

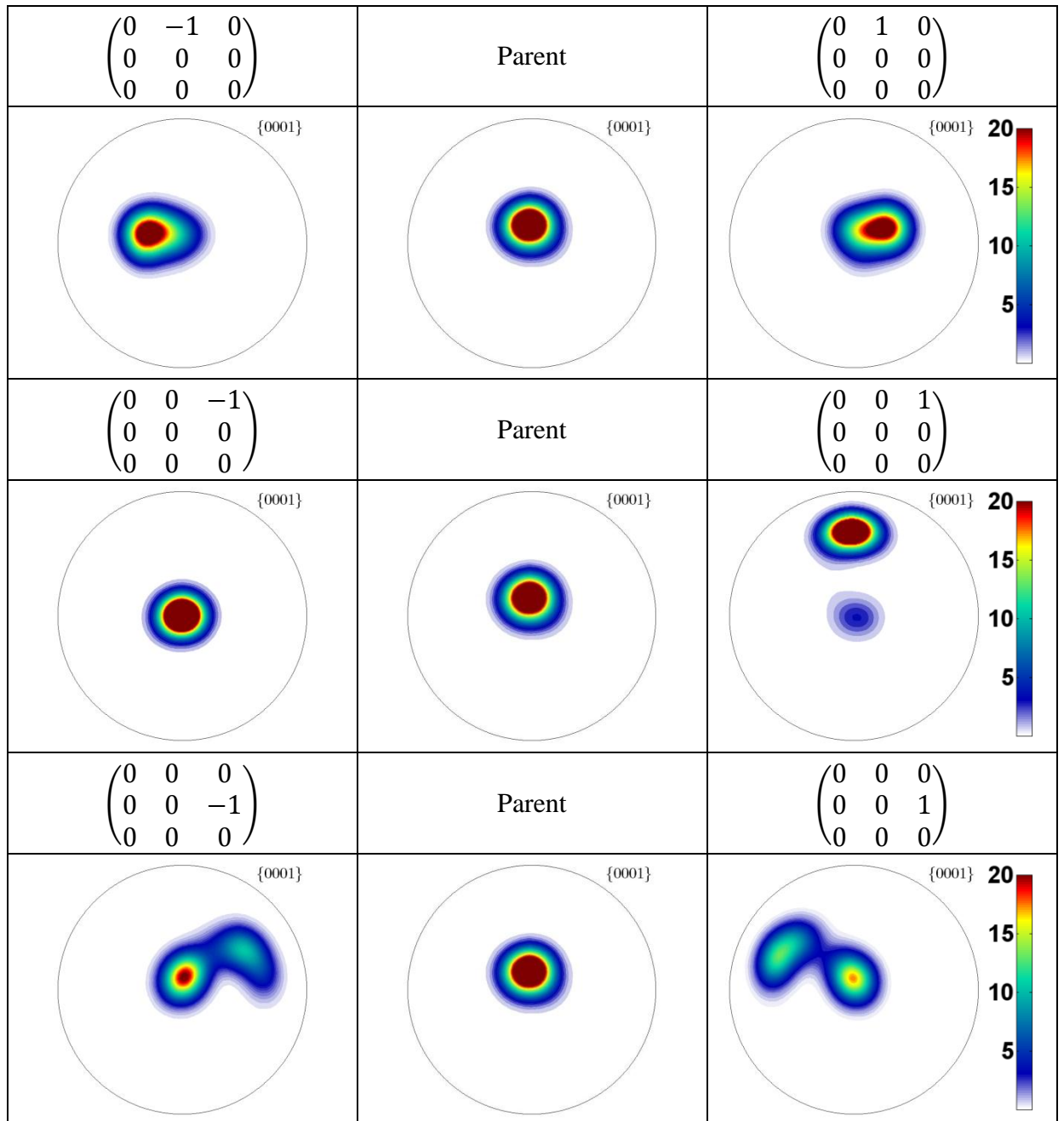
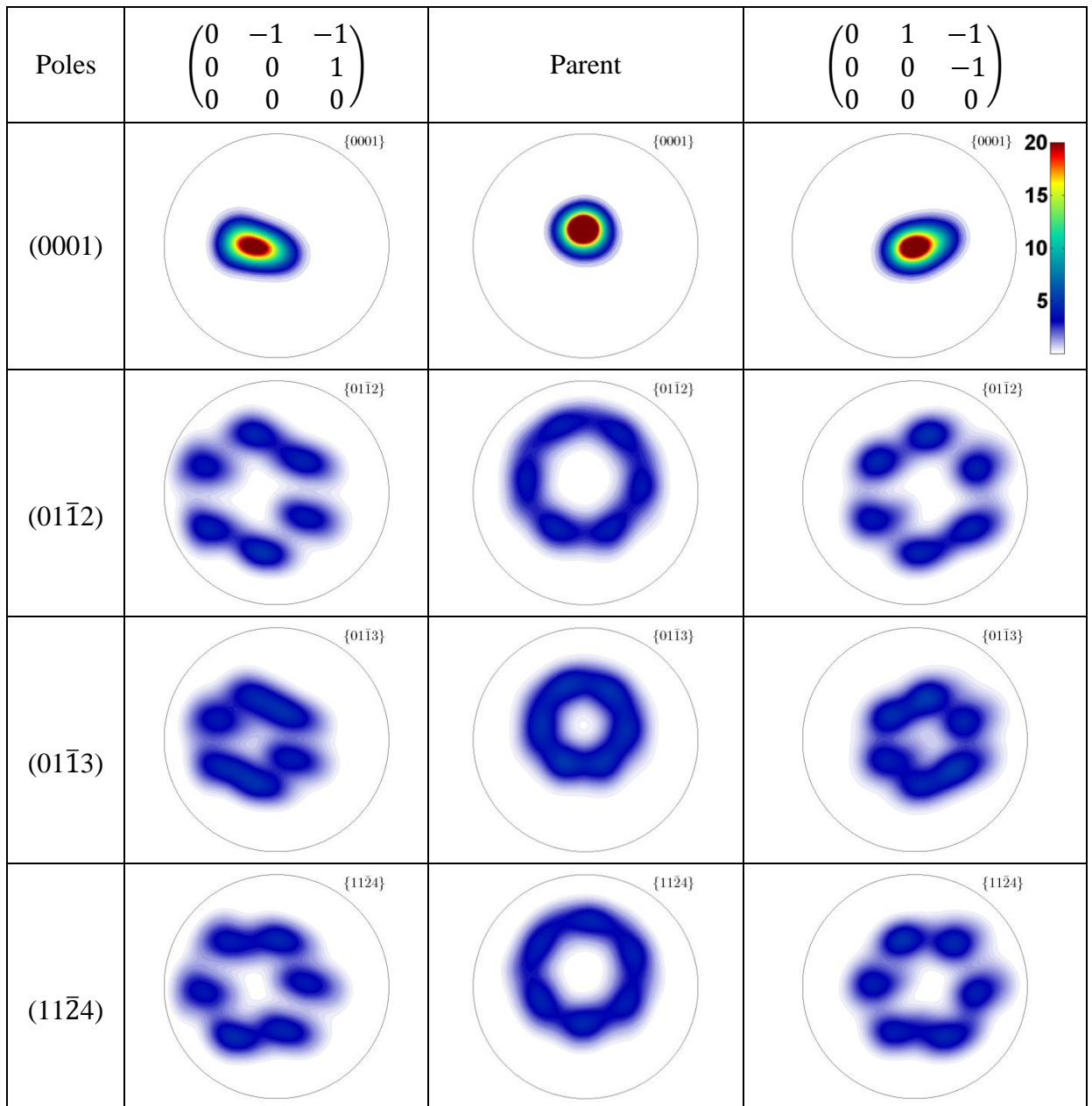
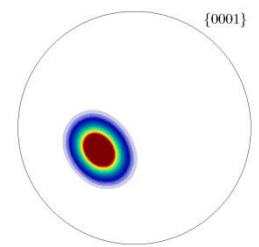
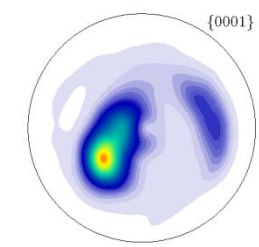
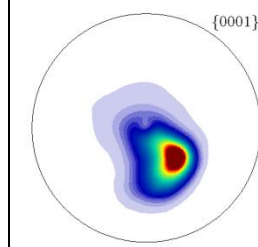
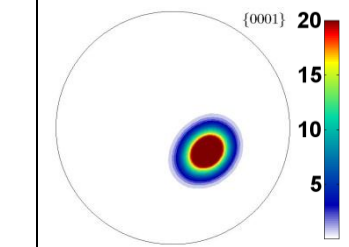
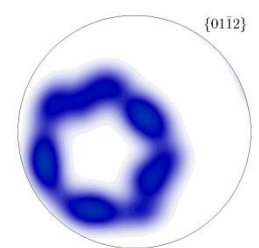
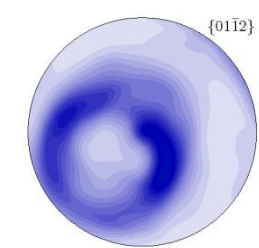
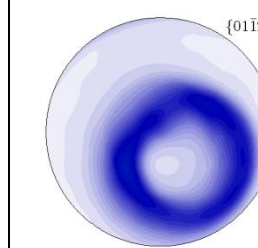
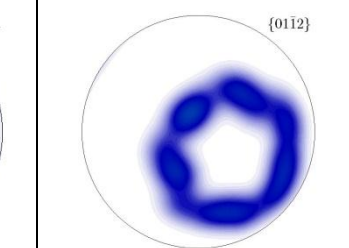
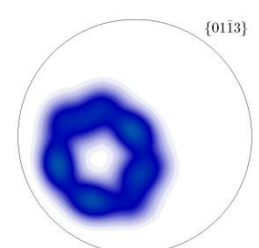
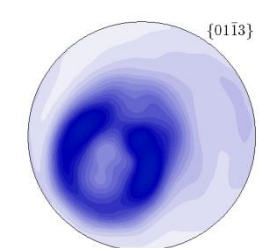
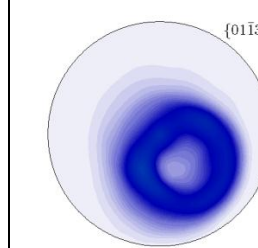
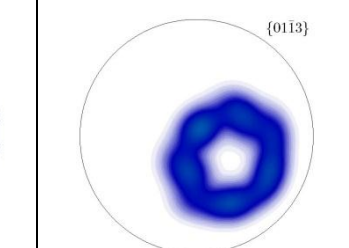


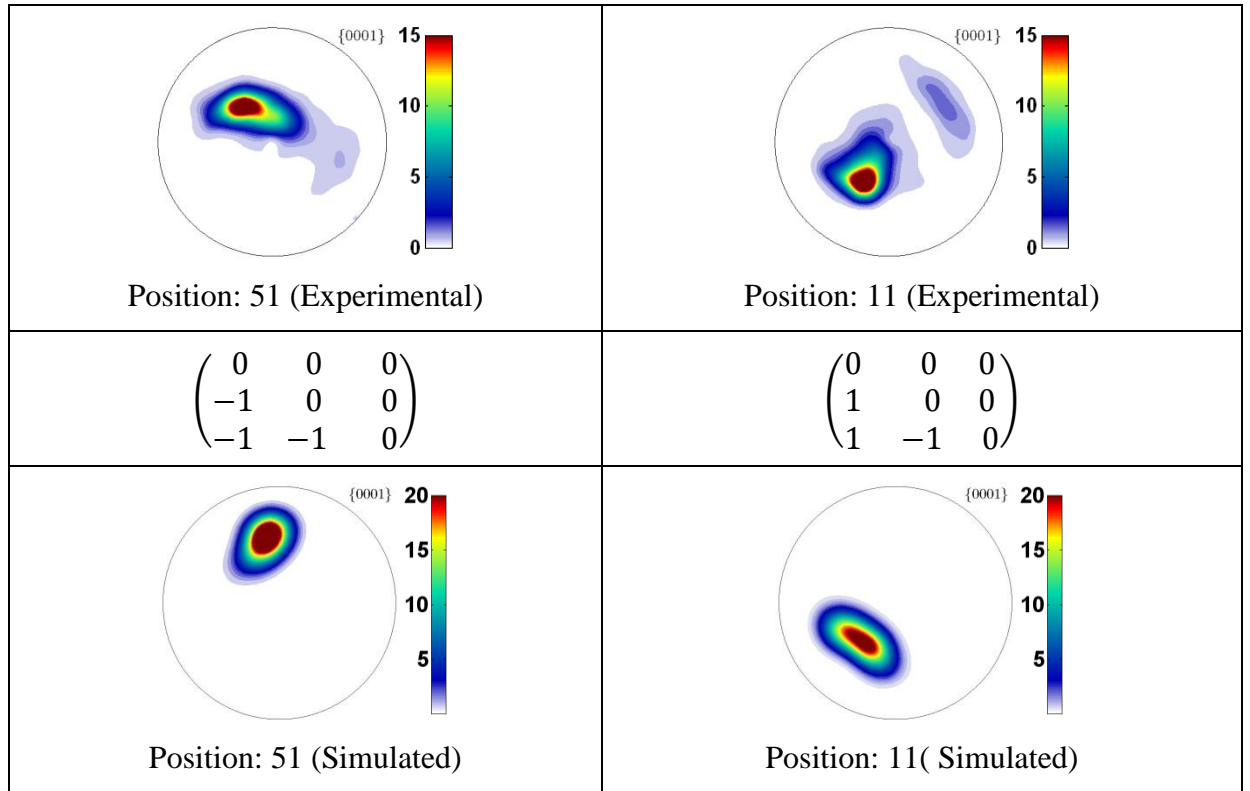
Figure 4.9: Simulated pole figures after imposition of different velocity gradients. The simulations were conducted by considering -1 and +1 values for L_{12} , L_{13} and L_{23} components.



(a)

Position	p1 (Simulated)	p1 (Experimental)	p5 (Experimental)	p5 (Simulated)
Velocity Gradient	$\begin{pmatrix} 0 & 0 & 0 \\ 0 & 0 & 0 \\ 1 & -1 & 0 \end{pmatrix}$			$\begin{pmatrix} 0 & 0 & 0 \\ 0 & 0 & 0 \\ 1 & 1 & 0 \end{pmatrix}$
Poles (0002)				
(01 $\bar{1}$ 2)				
(01 $\bar{1}$ 3)				

(b)



(c)

Figure 4.10: (a) Simulated pole figures, with an effective von Mises strain ($\bar{\epsilon}$) of 1.0 and appropriate velocity gradients, approximately captured experimental results at extreme FSP locations of p1 and p5 for unidirectional FSP. (b) Simulated pole figures with appropriate velocity gradient matrix for the reverse pass FSP at the locations p1 and p5. (c) Simulated pole figures with appropriate velocity gradient matrix for 51 and 11 locations (as in figure 4.1d) of transverse pass FSP.

Though the aforementioned hypothesis appears plausible and certainly capable of explaining the experimental observations, well-structured experiments are needed to test the hypothesis further and to relate to the micro-mechanism(s) involved. The present observations on crystallographic texture and microstructure, however, remain consistent and reproducible.

4.6 Summary

This study involved multi-pass FSP of Mg under different tool movements. Though most of the FSPs were conducted in air, additional FSP processing was also performed under water. The latter showed smaller grains, higher misorientation and weaker texture intensities. This highlights the role of post-FSP grain coarsening in the final microstructure evolution. Experimental texture measurements revealed location and tool movement dependent, but pass independent, texture evolution. The experimental texture evolution was generalized as pole-shifts and texture randomization. The pole-shifts did depend on tool movement and location, but were independent of the number of passes and imposed cooling.

VPSC simulations, with appropriate velocity gradients, could capture the location dependent developments in FSP crystallographic textures. However, required strain in the VPSC was more than an order of magnitude lower than the expected values in a FSP process. Even at the lower strains, VPSC simulations had 3-5 times higher texturing than the experimental observations. Microstructural observations showed interleaved structure of fine (a few hundred nanometer) and coarse (several micron) grains. The fine grains had higher defect density, but lower texturing.

Based on the experimental observations, following model or mechanism(s) for FSP/FSW microstructural evolution was proposed: Initial local shear plus dynamic recovery/recrystallization leading to ultra-fine grains, deformation being accommodated by ultra-fine grain superplasticity followed by post-FSP grain coarsening. Though such model appears to rationalize the post-FSP microstructural evolution, it needs to be tested further with carefully crafted experiments.

References

1. B. L. Mordike and T. Ebert, *Mater. Sci. Eng. A* **302**, 37 (2001).
2. M. Easton, A. Beer, M. Barnett, C. Davies, G. Dunlop, Y. Durandet, S. Blacket, T. Hilditch, and P. Beggs, *JOM* **60**, 57 (2008).
3. A. Luo, *Mater. Sci. Forum* **419-422**, 57 (2003).

4. K. U. Kainer, Magnesium : Proceedings of the 6th International Conference Magnesium Alloys and Their Applications (2003).
5. S. R. Agnew and Ö. Duygulu, *Int. J. Plast.* **21**, 1161 (2005).
6. S. R. Agnew, J. W. Senn, and J. A. Horton, *JOM* **58**, 62 (2006).
7. S. R. Agnew and O. Duygulu, *Mater. Sci. Forum* **419-422**, 177 (2003).
8. F.-K. Chen and T.-B. Huang, *J. Mater. Process. Technol.* **142**, 643 (2003).
9. Y. Wang and J. Huang, *Mater. Chem. Phys.* **81**, 11 (2003).
10. B. Hutchinson, *Int. J. Mater. Res.* **100**, 556 (2009).
11. W. B. Hutchinson and M. R. Barnett, *Scr. Mater.* **63**, 737 (2010).
12. H. T. Jeong and T. K. Ha, *J. Mater. Process. Technol.* **187-188**, 559 (2007).
13. G. Huang, Q. Liu, L. Wang, R. Xin, X. Chen, and F. Pan, *Trans. Nonferrous Met. Soc. China* **18**, s170 (2008).
14. A. Styczynski, C. Hartig, J. Bohlen, and D. Letzig, *Scr. Mater.* **50**, 943 (2004).
15. M. Wang, R. Xin, B. Wang, and Q. Liu, *Mater. Sci. Eng. A* **528**, 2941 (2011).
16. M. R. Barnett, M. D. Nave, and C. J. Bettles, *Mater. Sci. Eng. A* **386**, 205 (2004).
17. M. D. Nave and M. R. Barnett, *Scr. Mater.* **51**, 881 (2004).
18. J. Bohlen, M. R. Nürnberg, J. W. Senn, D. Letzig, and S. R. Agnew, *Acta Mater.* **55**, 2101 (2007).
19. N. Stanford and M. R. Barnett, *Mater. Sci. Eng. A* **496**, 399 (2008).
20. P. Bakke, K. Pettersen, and H. Westengen, *JOM* **46** (2003).
21. S. Liang, H. Sun, Z. Liu, and E. Wang, *J. Alloys Compd.* **472**, 127 (2009).
22. G. Vespa, L. W. F. Mackenzie, R. Verma, F. Zarandi, E. Essadiqi, and S. Yue, *Mater. Sci. Eng. A* **487**, 243 (2008).
23. K. Matsubara, Y. Miyahara, Z. Horita, and T. G. Langdon, *Acta Mater.* **51**, 3073 (2003).
24. G. Bhargava, W. Yuan, S. S. Webb, and R. S. Mishra, *Metall. Mater. Trans. A* **41**, 13 (2009).
25. J. A. del Valle, F. Carreño, and O. A. Ruano, *Acta Mater.* **54**, 4247 (2006).
26. R. B. Figueiredo and T. G. Langdon, *Mater. Sci. Eng. A* **430**, 151 (2006).

27. L. Kestens, R. H. Petrov, P. Gobernado, and E. Leunis, *Solid State Phenom.* **160**, 23 (2010).
28. Z. Y. Ma, R. S. Mishra, and M. W. Mahoney, *Acta Mater.* **50**, 4419 (2002).
29. Z. Y. Ma, *Metall. Mater. Trans. A* **39**, 642 (2008).
30. R. S. Mishra and Z. Y. Ma, *Mater. Sci. Eng. R Reports* **50**, 1 (2005).
31. R. Nandan, T. Debroy, and H. K. D. H. Bhadeshia, *Prog. Mater. Sci.* **53**, 980 (2008).
32. Y. N. Zhang, X. Cao, S. Larose, and P. Wanjara, *Can. Metall. Q.* **51**, 250 (2012).
33. K. Elangovan and V. Balasubramanian, *Mater. Des.* **29**, 362 (2008).
34. A. Arora, R. Nandan, A. P. Reynolds, and T. DebRoy, *Scr. Mater.* **60**, 13 (2009).
35. K. Elangovan and V. Balasubramanian, *Mater. Sci. Eng. A* **459**, 7 (2007).
36. W. Yuan, S. K. Panigrahi, and R. S. Mishra, *Metall. Mater. Trans. A* **44**, 3675 (2013).
37. S. H. Chowdhury, D. L. Chen, S. D. Bhole, X. Cao, and P. Wanjara, *Metall. Mater. Trans. A* **44**, 41 (2012).
38. K. Nakata, Y. G. Kim, H. Fujii, T. Tsumura, and T. Komazaki, *Mater. Sci. Eng. A* **437**, 274 (2006).
39. Z. Y. Ma, S. R. Sharma, and R. S. Mishra, *Scr. Mater.* **54**, 1623 (2006).
40. R. W. Fonda, J. F. Bingert, and K. J. Colligan, *Scr. Mater.* **51**, 243 (2004).
41. D. P. Field, T. W. Nelson, Y. Hovanski, and K. V. Jata, *Metall. Mater. Trans. A* **32**, 2869 (2001).
42. A. Arora, Z. Zhang, A. De, and T. DebRoy, *Scr. Mater.* **61**, 863 (2009).
43. C. N. Tomé, P. J. Maudlin, R. A. Lebensohn, and G. C. Kaschner, *Acta Mater.* **49**, 3085 (2001).
44. L. Commin, M. Dumont, J.-E. Masse, and L. Barrallier, *Acta Mater.* **57**, 326 (2009).
45. C. I. Chang, C. J. Lee, and J. C. Huang, *Scr. Mater.* **51**, 509 (2004).
46. C. I. Chang, X. H. Du, and J. C. Huang, *Scr. Mater.* **57**, 209 (2007).
47. K. V. Jata and S. L. Semiatin, *Scr. Mater.* **43**, 743 (2000).
48. B. M. Darras, *J. Mater. Eng. Perform.* **21**, 1243 (2011).

49. U. F. H. R. Suhuddin, S. Mironov, Y. S. Sato, H. Kokawa, and C.-W. Lee, *Acta Mater.* **57**, 5406 (2009).
50. A. Tripathi, A. Tewari, N. Srinivasan, G. M. Reddy, S. M. Zhu, J. F. Nie, R. D. Doherty, and I. Samajdar, *Metall. Mater. Trans. A* **46**, 3333 (2015).
51. W. Yuan, R. S. Mishra, B. Carlson, R. K. Mishra, R. Verma, and R. Kubic, *Scr. Mater.* **64**, 580 (2011).
52. M. D. Abràmoff, I. Hospitals, P. J. Magalhães, and M. Abràmoff, *Biophotonics Int.* **11** (7), 36 (2004).
53. A. J. Schwartz, M. Kumar, and B. L. Adams, *Electron Backscatter Diffraction in Materials Science*, Second Edition (2000).
54. O. Engler and V. Randle, *Introduction to Texture Analysis Macrotecture, Microtexture and Orientation Mapping*, Second Edition (2010).
55. F. Bachmann, R. Hielscher, and H. Schaeben, *Solid State Phenom.* **160**, 63 (2010).
56. R. Hielscher and H. Schaeben, *J. Appl. Crystallogr.* **41**, 1024 (2008).
57. R. M. Langford and C. Clinton, *Micron* **35**, 607 (2004).
58. R. A. Lebensohn, C. N. Tome, *Acta Mater.* **41**, 2611 (1993).
59. H. Yoshinaga, R. Horiuchi, *Trans. JIM* **4**, Vol. 4 (1963).
60. B. C. Liechty and B. W. Webb, *J. Mater. Process. Technol.* **208**, 431 (2008).
61. J. Young, D. Field, and T. Nelson, *Metall. Mater. Trans. A* **44**, 3167 (2013).
62. J. M. Root, D. P. Field, and T. W. Nelson, *Metall. Mater. Trans. A* **40**, 2109 (2009).
63. S. H. C. Park, Y. S. Sato, and H. Kokawa, *Metall. Mater. Trans. A* **34**, 987 (2003).
64. J.-H. Cho, D. E. Boyce, and P. R. Dawson, *Mater. Sci. Eng. A* **398**, 146 (2005).
65. J.-H. Cho and P. R. Dawson, *Metall. Mater. Trans. A* **37**, 1147 (2006).
66. H.-H. Cho, S.-T. Hong, J.-H. Roh, H.-S. Choi, S. H. Kang, R. J. Steel, and H. N. Han, *Acta Mater.* **61**, 2649 (2013).
67. H. N. B. Schmidt, T. L. Dickerson, and J. H. Hattel, *Acta Mater.* **54**, 1199 (2006).
68. R. Nandan, G. G. Roy, and T. Debroy, *Metall. Mater. Trans. A* **37A**, 1247 (2006).
69. R. Nandan, G. G. Roy, T. J. Lienert, and T. Debroy, *Sci. Technol. Weld. Join.* **11**, 526 (2006).

70. P. Heurtier, C. Desrayaud, and F. Montheillet, *Mater. Sci. Forum* **396-402**, 1537 (2002).
71. J. A. Schneider and A. C. Nunes, *Metall. Mater. Trans. B* **35**, 777 (2004).
72. R. W. Fonda and J. F. Bingert, *Metall. Mater. Trans. A* **35**, 1487 (2004).
73. B. Verlinden, J. Driver, I. Samajdar, and R. D. Doherty, *Thermomechanical Processing of Metallic Materials*, First Edition (Pergamon Materials Series, 2007).

Chapter 5

Friction stir processing under different thermal history: Experimental observation and numerical validation

5.1 Abstract

Friction stir processing (FSP) processing of a commercial magnesium alloy was performed under air, liquid nitrogen and water. Experimental observations, on the process zone dimensions and temperature profiles, showed significant differences: highlighting the influence of the thermal history. Numerical validations were attempted using multi-physics finite element simulations. A three-dimensional steady-state coupled laminar fluid flow and heat transfer model was developed. The model considered the alloy as a non-Newtonian visco-plastic fluid, with the viscosity being defined as a function of temperature. The effect of the convective heat transfer coefficient on the simulated profiles was thus explored. The simulations were remarkably effective in capturing the experimental observations on process zone dimensions and temperature profiles.

5.2 Introduction

Friction stir processing (FSP) was developed [1–3] on the principles of friction stir welding (FSW). FSP enforces severe plastic deformation and associated refinement of the grain size [4–9] and modifications in crystallographic texture [10–17] and properties [14,18–23]. The microstructural evolution in FSP is dictated by the intense shear and dynamic/static restorations of the deformed structure in the wake of the high temperatures present during the processing [9,24–26]. There have been debates on the relative roles of deformation and softening mechanisms [4,27–29]. For example, dynamic recovery and recrystallization were stipulated to play an important role [4,9,24,27]. Post FSP fine grain structure is also expected to be amenable to grain coarsening [9,26]. Recent studies in magnesium [30,31] even highlighted the possibilities ultra-fine grain superplasticity followed grain coarsening as a plausible mechanism of FSP microstructure developments.

The processing inputs to microstructure evolution involve the plastic deformation and the thermal history [9,24–26,32–36]. The latter was often shown to play an important role. For example, application of appropriate external cooling enforced [24,26,33–35] significant modifications to the post-FSP microstructures. Complete thermal mapping of the stir zone is difficult. This initiated the need for accurate thermal model(s). Numerical [37–42] as well as analytical models [43–46] were proposed. Many of them were also evaluated against ‘limited’ experimental data. The numerical modeling typically involved 3-dimensional steady-state deformation or fluid flow and heat transfer [38,39,41,45,47–55]. Though the steady-state approach is arguably a simplification of the actual non-steady-state process, but they were remarkably successful in capturing the experimental temperature profiles. Similarly, the deformation part has been modeled both as classical deformation mechanism [51,53,56] as well as a fluid flow [37,48,52,57,58] problem: the latter being easier to formulate. However, both approaches were shown to capture the experimental results.

Though rich literature [38,39,41,45,47–55,59,60] exists on the modeling and validation of temperature profiles during FSP/FSW, rarely such efforts include the effect of coolant application. In fact, to the author’s best knowledge, there is only one such simulation study [61], which unfortunately did not involve experimental validation. In this study, FSP of commercial magnesium alloy (AZ31) was conducted under air, liquid nitrogen and water. The

application of different cooling rates affected the microstructural evolution and mechanical responses during the process. The most significant differences were in the dimensions of the process zone and in the measured temperature profiles. In this manuscript, a coupled fluid mechanics and heat transfer approach based steady state 3-D model was developed in a commercial multi-physics software platform (COMSOL™). The material was assumed to be viscoplastic, and the material constants were derived from available [62] hot compression test data. The simulated thermal history, under different convective heat transfer coefficients, was then verified with experimental temperature profiles and process zone dimensions.

5.3 Experimental methods

Commercially procured hot rolled AZ31 (see table 5.1 for chemical composition) plate was subjected to friction stir processing (FSP). The detailed schematics of the FSP, including locations of embedded thermocouple is shown in figure. 5.1. AISI-4340 tool steel (Rockwell ‘C’ hardness of 55) was used as the tool material. The tool consisted of a cylindrical shoulder of diameter 18 mm with a conical tool of upper diameter 6 mm and lower diameter of 3 mm. Tool tilt of approximately 3° with respect to the vertical axis was given. The processing was done at a constant rotational and translational speed of 600 RPM and 1.33 mm/min respectively. These conditions provided consistent defect free FSP of the AZ31. During FSP, the processing parameters (like spindle speed and torque, z-axis load and torque) were monitored. Temperature measurements were obtained through appropriately embedded thermocouples (see figure. 5.1b).

The processing was performed in three different ambient environment conditions: water (PW), liquid nitrogen (PLN) and air (PA). In the first case, the processing assembly (figure. 5.1a) was submerged in water kept at ambient (298K) temperature. Continuous water circulation was used to avoid temperature rise by more than +50K. Similarly, in the second case, the assembly was submerged under liquid nitrogen (83K). During FSP, continuous pouring of liquid nitrogen helped replenish and compensate the loss due to boiling. For processing under air, workshop air circulation was used as the cooling medium. Processing parameters were otherwise identical in all three cases.

Table 5.1 Chemical composition (in wt% alloying elements) of the friction stir processed AZ31 magnesium alloy

Al	Zn	Mn	Ca	Si	Cu
3.1	0.7	0.4	0.04	0.1	0.01

Microstructural observations were made at the respective process zone centers (1.5 mm from the surface). Standard metallographic technique [63], followed by polishing with sub-micron colloidal silica in a StruersTM Tegrapol was used. For optical microstructure, the polished samples were etched in acetic picral solution (4.2 g picric acid, 20 ml distilled water, 50 ml ethanol and 10 ml acetic acid). Optical micrographs were observed in ZeissTM Axio Imager unit. For EBSD (electron backscattered diffraction), final polishing was done in a GatanTM PECS-682 system operated at 6 keV. Additional plasma cleaning in GatanTM Solaris was also provided. EBSD measurements were made in a FEITM Quanta 3D-FEG (field emission gun) SEM (scanning electron microscope) and OIMTM EBSD system.

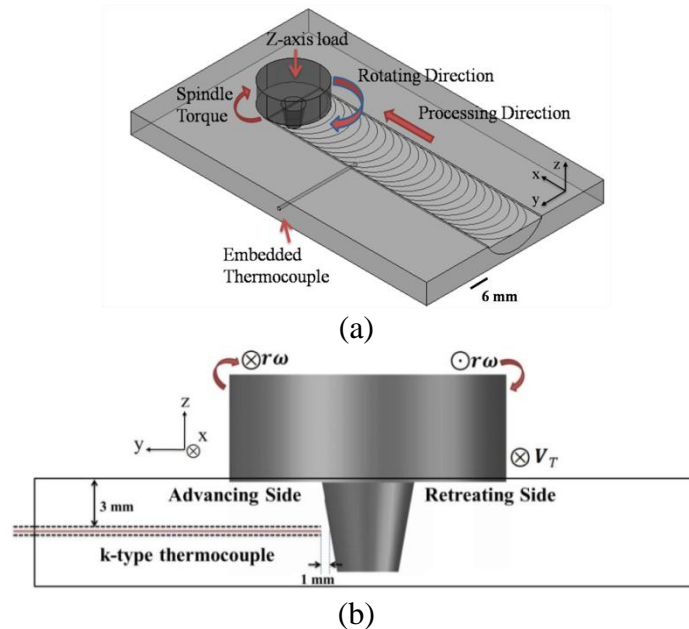


Figure 5.1: (a) Schematic of the tool and workpiece used in the FSP. This includes processing direction and tool rotation. The set-up was used to measure z-axis load, spindle torque and temperature profiles (through embedded thermocouple). (b) Cross-sectional schematic of the FSP. Advancing and retreating sides and the position of the embedded k-type thermocouple are shown.

Beam and video conditions were kept identical between the scans. For data analysis, EBSD data with confidence index (CI: scale of 0-1) greater than 0.1 were taken. CI is the statistical measure of accuracy in automated indexing [64]. EBSD scans were represented in

inverse pole figure (IPF) maps [65]. A grain was considered as a region bound by a continuous boundary above 5° misorientation. Grain size was estimated by measuring the equivalent circle diameter on the EBSD maps. The EBSD scans were conducted on large areas to generate statistically robust quantitative data.

5.4 Three dimensional steady state model

5.4.1 Simulation geometry and boundary conditions

A steady state 3-D model with coupled multi-physics of fluid mechanics and heat transfer was developed in COMSOL™. All the symbols and notations involved in the definition of the model are summarized in table 5.2. The assumption of steady state is well justified, since after the initial transient, the process of FSP is arguably at steady state with respect to the FSP tool reference frame. Multi-physics was essential in coupling heat transfer in fluids and laminar stationary fluid flow. The model was applied to a region of 125 mm by 50 mm by 7 mm volume, filled with viscous fluid. The viscosity varied as a function of temperature. The tool (pin and the shoulder) fluid interfaces were given sliding wall condition. The tool was assumed to be rotating at a constant rotational velocity, while the fluid moved at a constant translational velocity of u_{weld} (figure 5.2a). This was implemented by giving an inlet and outlet flow velocity of u_{weld} to the fluid as shown in figure 5.2a. Selective physics based meshing (adaptive meshing) was used: fine meshing near the tool-fluid interface and relatively coarser meshing at a distance (see figure 5.2b). The tool consisted of a conical pin, with upper ($r_{pin,upper}$: 3mm) and lower ($r_{pin,lower}$: 1.5 mm) radius, and a thin cylindrical shoulder (with upper radius of 9 mm). As a part of FSP processing, a small portion (0.1 mm) of the shoulder was inserted inside the workpiece. Figure 5.2c shows the geometry of tool. The tool was assumed to be rotating at a constant rotational velocity (ω). The velocity vector (\mathbf{v}) at a given position on the tool is schematically shown in figure 5.2d, where (x, y) are the Cartesian coordinates of the point and r is the radial distance (square root of addition of square of x and y) of the point from the center of the tool.

Table 5.2: List of symbols and notations

u_{weld}	Translational velocity of the fluid (m/sec)
$r_{pin,upper}$	Radius of the upper part of pin (m)
$r_{pin,lower}$	Radius of the lower part of pin (m)
$r_{shoulder}$	Radius of the shoulder (m)
ω	Rotational velocity (RPM)
ρ	Density (kg/m ³)
\mathbf{u}	Velocity (m/sec)
p	Pressure (N/m ²)
μ	Viscosity (N-sec/m ²)
\mathbf{F}	Body forces (N)
$\mathbf{i}, \mathbf{j}, \mathbf{k}$	Unit vectors in x,y,z directions of Cartesian coordinate system
\mathbf{n}	Normal vector at the surface
h	Convective heat transfer coefficient (W/m ² K)
T_{ext}	External ambient temperature (K)
k	Thermal conductivity (W/mK)
q_o	Constant heat flux (W)
∇T	Temperature gradient (K/m)
σ	True stress (N/m ²)
ε	True strain
$\dot{\varepsilon}$	Strain rate (s ⁻¹)
C_p	Specific heat capacity (J/KgK)
c	Speed of sound (m/sec)
K'	Coefficient of stiffness
μ'	Coefficient of friction
$\bar{Y}(T)$	Yield strength (MPa)
A_s	Cross sectional area of shoulder (m ²)
F_n	Vertical force (N)

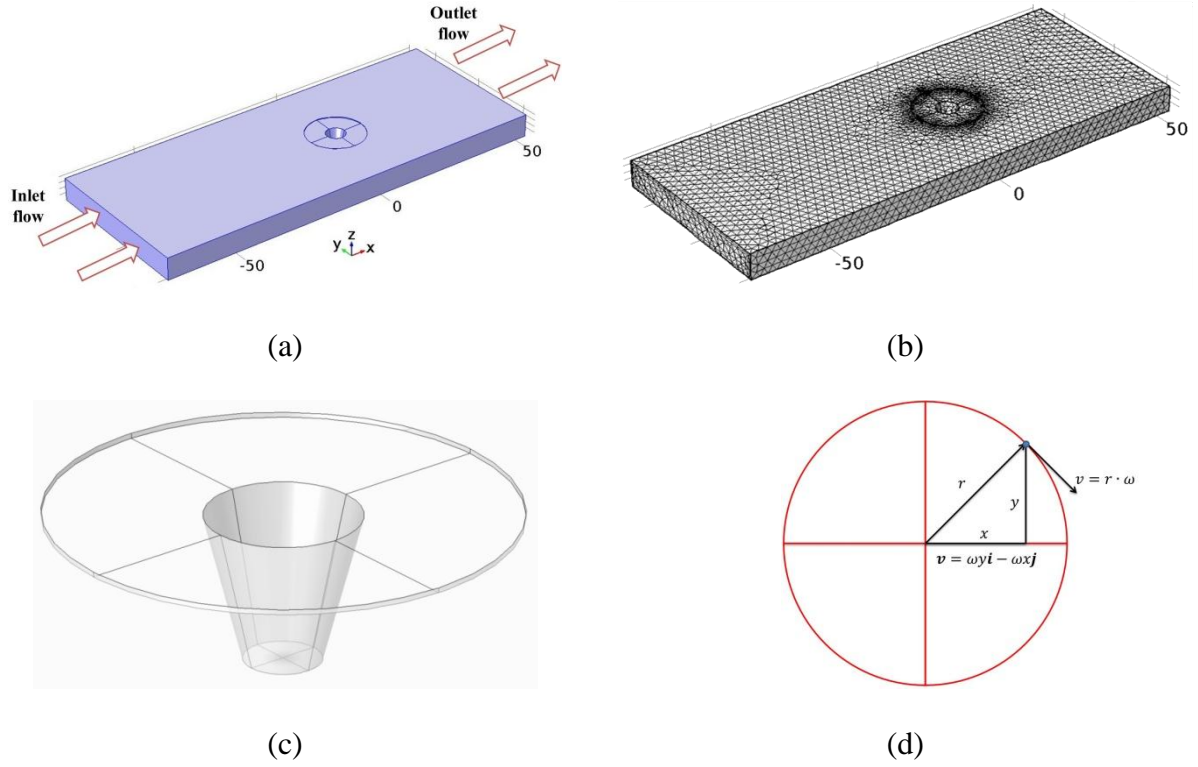


Figure 5.2: (a) Schematic of the workpiece in Comsol™, (b) mesh distribution, (c) tool profile used, and (d) velocity profile and its expression.

5.4.2 Equations for steady state material and heat flow

In the present coupled model, magnesium alloy was considered as non-Newtonian, viscoplastic, incompressible and laminar fluid. Based on conservation of mass,

$$\frac{\partial \rho}{\partial t} + \nabla \cdot (\rho \mathbf{u}) = 0 \quad (1)$$

where, ρ is the density and \mathbf{u} is the velocity vector, which for the incompressible fluid ($\rho = \text{constant}$) can be simplified to

$$\nabla \cdot (\rho \mathbf{u}) = 0 \quad (2)$$

Laminar flow of viscous fluid in the stir zone for the stationary case was defined as,

$$\rho(\mathbf{u} \cdot \nabla)\mathbf{u} = \nabla \cdot \left[-p\mathbf{I} + \mu(\nabla\mathbf{u} + (\nabla\mathbf{u})^T - \frac{2}{3}\mu(\nabla \cdot \mathbf{u})\mathbf{I}) \right] + \mathbf{F} \quad (3)$$

Where, p is the pressure, μ is the viscosity of the AZ31 Mg alloy and \mathbf{F} is the body forces. To capture the constitutive behavior of AZ31 Mg alloy, the viscosity μ was defined as a function of strain-rate and temperature. The rotational velocity at the surface of the tool was represented as $\omega y\mathbf{i} - \omega x\mathbf{j}$ for the first coordinate. It needs to be noted that this expression is true for all the four coordinates and hence for the entire pin and shoulder surface of the tool. Convective heat flux boundary condition given at the surfaces, which are in contact with the ambient environment, was given by the following expression.

$$-\mathbf{n} \cdot (-k\nabla T) = h(T_{ext} - T) \quad (4)$$

where \mathbf{n} is the normal vector at the surface, h is the convective heat transfer coefficient and T_{ext} is the external ambient temperature.

For the case of air, convective heat transfer coefficient (h) for the 5 surfaces (4 side faces and top surface) of the workpiece (exposed to air) was taken as 25W/m²K. The ambient external air temperature was taken as 298K and radiative heat loss with surface emissivity of 0.4 was assumed. For the bottom surface (backing plate), which was not exposed to air, the heat transfer coefficient value was taken as 150W/m²K. This is because the heat transfer occurs through contact resistance between the AZ31 Mg alloy and the mounting fixture at the backing plate. This value of heat transfer coefficient was kept the same for all the three processing conditions. For processing under liquid nitrogen, respective values of h and ambient temperature were taken as 150 W/m²K and 83K. For the case of FSP under water, external forced convection condition was used for the upper horizontal face with plate length of 0.125 m and external fluid velocity of 0.565 m/sec. For the 4 side faces, on the other hand, external natural convection condition was used. External ambient temperature of 298K was imposed for all the faces. The faces/wall of the tool (pin and shoulder) was considered to be constant heat flux boundary conditions, where q_o is the given constant heat flux.

$$-\mathbf{n} \cdot (-k\nabla T) = q_o \quad (5)$$

The equations for the heat and fluid flow were discretized in the COMSOL™, using the stationary linear direct solver PARDISO and the nested dissection multithreaded reordering algorithm.

5.4.3 Constitutive properties of AZ31 Mg alloy

The generalized stress strain curves (see appendix) of AZ31 Mg alloy was defined as,

$$\sigma = K(T, \dot{\epsilon}) \epsilon^{C(T, \dot{\epsilon})} \quad (6)$$

where σ and ϵ are the true stress and true strain values. K and C are functions of temperature (T) and strain rate ($\dot{\epsilon}$). Since the alloy was modelled as a viscous fluid, the constitutive property of the material was incorporated in the viscosity of the alloy/fluid. The viscosity was considered as function of temperature and strain rate as,

$$\mu(T) \equiv \frac{\partial \sigma}{\partial \dot{\epsilon}} \quad (7)$$

The viscous flow was assumed at the point when the flow stress was assumed to be strain independent ($\frac{\partial \sigma}{\partial \epsilon} = 0$). Heat capacity of AZ31 Mg alloy was taken as,

$$C_p = 26.19 - 1.01 \times 10^{-3} T - 1.60 \times 10^5 \times T^{-2} + 8.41 \times 10^{-6} \times T^2 \quad (8)$$

Density of the alloy was calculated as a function of temperature as given below:

$$\rho(T) = 1.778926 - 1.3968 \times 10^{-4} \times T \quad (9)$$

Speed of sound used in the model was calculated by the Newton-Laplace equation (see equation below).

$$c = \sqrt{\frac{K'}{\rho}} \quad (10)$$

where K' is the coefficient of stiffness (bulk modulus, 45 GPa for the given material). Thermal conductivity of the alloy was also considered a function of temperature.

5.4.4 Heat input

In the present model, the heat generation between the pin and the workpiece was given by a function of radius, coefficient of friction, rotational velocity and temperature dependent yield strength (captured in the viscosity function) of the alloy [42]:

$$q_{pin}(T) = \frac{\mu'}{\sqrt{3(1 + \mu'^2)}} r \omega \bar{Y}(T) \quad (11)$$

where μ' is the friction coefficient, r is the radius of the pin (which was a function of the depth of the tool: varying linearly from $r_{pin,lower}$ to $r_{pin,upper}$), ω (rad/s) is the angular velocity of the tool and $\bar{Y}(T)$ is the yield strength of the alloy at a temperature of T (K). The latter was defined by the interpolation function (see appendix). This heat flux condition was given at the conical interface of the tool with the workpiece.

Heat generation by the lower horizontal section of the pin and the shoulder of the tool was given by a piece wise function of temperature, where heat generation was null when temperature was greater than melting point of the alloy [42].

$$q_{shoulder}(r, T) = \left\{ \begin{array}{ll} \left(\frac{\mu' F_n}{A_s} \right) \omega r & \text{for } T < T_{melt} \\ 0 & \text{for } T \geq T_{melt} \end{array} \right\} \quad (12)$$

where F_n is the normal force, A_s is the total area of the lower horizontal section of the pin and the shoulder surface, in contact with the workpiece: $\pi(r_{shoulder}^2 - r_{pin,upper}^2)$.

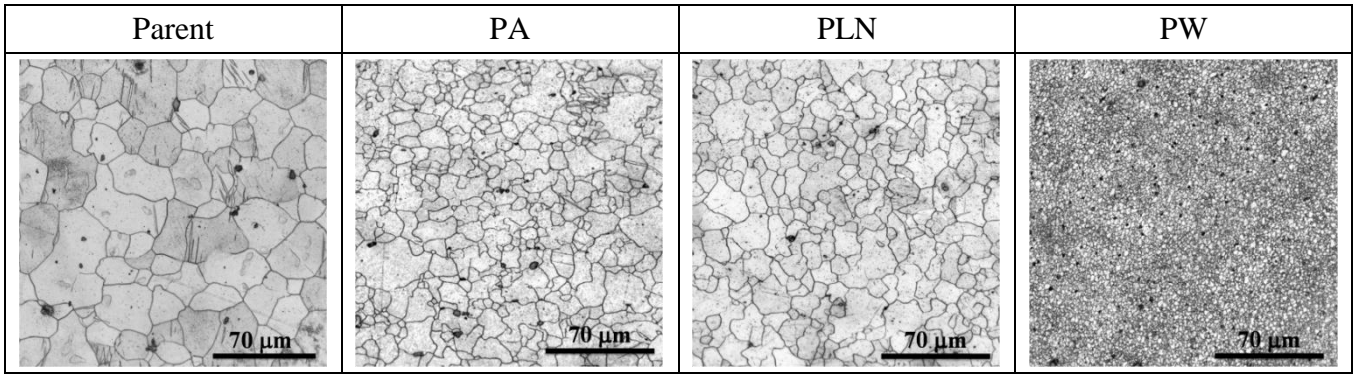
For the small vertical part of the shoulder, which was plunged into the workpiece, the heat generation term was given by the following expression.

$$q_{shoulder1}(T) = \frac{\mu'}{\sqrt{3(1 + \mu'^2)}} r_{shoulder} \omega \bar{Y}(T) \quad (13)$$

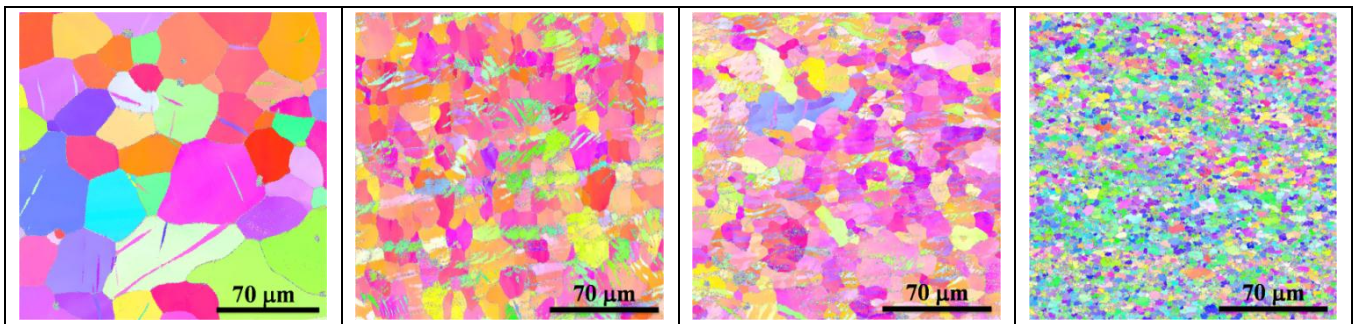
5.5 Results and discussion

The optical microstructure at the center zone after FSP at various processing conditions (PA, PLN, and PW) along with the parent microstructure is given in figure 5.3a. Similar region as observed through EBSD is given in figure 5.3b. From both these figures it is clear that the parent microstructure is refined by FSP under all three mediums. The degree of refinement, however, varied with the processing medium. The IPF maps (figure 5.3b) also reveal the presence of large fractions of twins, which are not very apparent in the optical microstructure (figure 5.3a). A quantitative estimate of equivalent circle diameter grain size as measured through EBSD¹ is shown in figure 5.3c. The grain size of parent material, prior to FSP, was ~48 μm . This was refined to respective average sizes of ~12, ~10 and ~3 μm , as the cooling medium was changed from air to liquid nitrogen and then to water. The difference in average grain size between air and liquid nitrogen is not statistically significant since it is of the order of the experimental error bars (figure 5.3c).

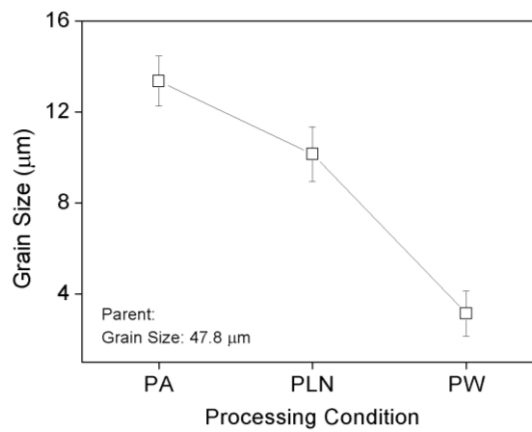
¹ The estimated grain sizes between optical and EBSD differed. The former depends on the imposed chemical etching, while EBSD grain size is subject to the grain boundary definition (taken as $> 5^\circ$ in this study).



(a)



(b)



(c)

Figure 5.3: (a) Optical micrographs and (b) EBSD images (in inverse pole figure notation) for the prior and post FSP specimens. These include prior-FSP parent and microstructures at the center of the processed zones. (c) Grain size (from EBSD data) in the respective process zones. Error bars representing standard deviations from multiple EBSD scans. The images and data include FSP under air (PA), water (PW) and liquid nitrogen (PLN).

The vertical load (z-axis load) required to keep the spindle inside the workpiece during FSP is given in figure 5.4a. The initial z-loading can be considered as analogous to the loading observed during micro-hardness indentation. At the start of FSP, the z-axis load is zero. The z-axis load starts increasing as the pin of the spindle penetrates the workpiece. After the pin has completely penetrated the workpiece (at time t^*), the shoulder of the spindle impinges the workpiece. Since, the shoulder is very broad compared to the pin, the impingement of shoulder leads to rapid increase in the z-axis load as shown in figure 5.4a. The impingement of the tool in the workpiece can be separated into two stages. In the first stage, insertion of the pin up to a depth of 5.8 mm occurs. In the second stage, insertion of the shoulder up to a depth of 0.1 mm occurs. Although the shoulder penetrates by only 0.1 mm, the increase of load due to shoulder insertion is nearly half of the increase in load due to pin insertion. The total increase of load due to tool insertion is found to be highest for the case of PA; however, the total increase is same for the case of PW and PLN. The load significantly drops further indicating the plastic softening of the workpiece and the start of the translational motion of the tool. With further processing the load is found to be stable for PA; however, PW and PLN experience fluctuations. The load is seen to be lower for the case of PA and PLN compared to PW, indicating higher thermal softening in these two cases. This also indicates higher rate of heat extraction for PW.

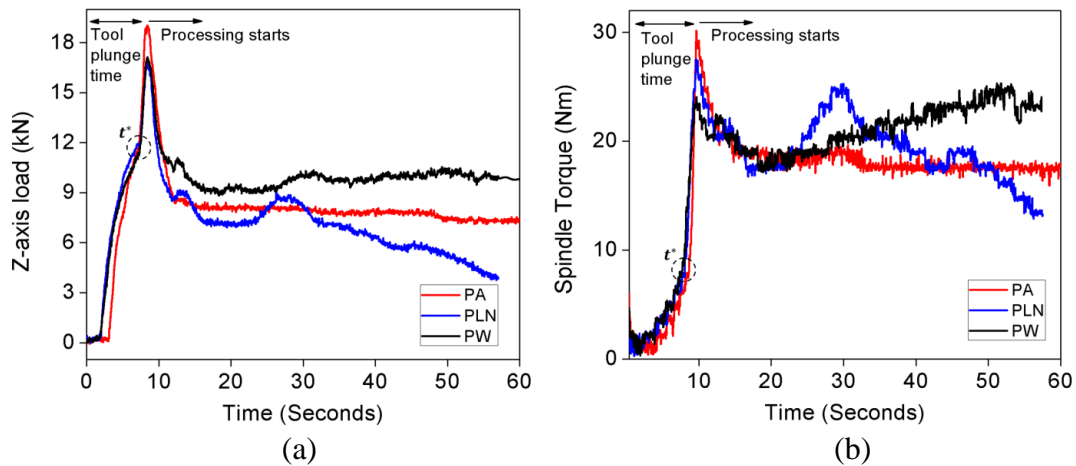


Figure 5.4: Profiles of the experimentally measured (a) z-axis load and (b) spindle torque. These are shown covering tool plunge duration and the start of the translational movement of the tool. The figures include FSP under air (PA), water (PW) and liquid nitrogen (PLN).

Figure 5.4b shows the variation of the spindle torque as the function of processing time for the three processing conditions. As seen for the case of load, spindle torque also starts from zero, and increases rather erratically till the point the pin is completely inserted as indicated by t^* . During the shoulder insertion stage, the increase of spindle torque is much steeper than the corresponding observed increase in load. This can be rationalized given the much larger diameter of the shoulder compared to pin, hence contributing a much larger moment of the force to the spindle torque. The total increase of spindle torque due to shoulder insertion was almost three times more than the total increase of spindle torque due to pin insertion. Spindle torque decreased as the translational motion of the tool started. PA showed a steady spindle torque during the subsequent processing. However, PLN and PW showed large fluctuations in spindle torque. The fluctuations in these two cases can be attributed to the variation in thermal softening. The variation in thermal softening can in turn be attributed to fluctuating heat transfer coefficient at the surface due to the steam/gas blanket formation because of boiling of water/LN₂. Load as well as torque was higher for PW than under PA and PLN for most of the processing times. Lower force/torque is an indicator of the higher softening and thus an indicator of the lower heat transfer coefficient for the case of PA.

Figure 5.5a shows the experimentally observed cross sectional profiles (with the tool overlay marked by dotted lines) of the FSP zone for the three processing medium. The images are obtained on a stereo-microscope by macro-etching. The boundary between the parent material and the FSP processed zone is clearly visible. The process zone is seen to be slightly larger than the pin at the bottom, whereas the top of the cross section (near the shoulder) shows a very broad processed zone. This implies that the FSP modifies structure not only in the space where pin/shoulder impinges, but also in the near surrounding due to viscoplastic stirring of the workpiece. The region of influence of this viscoplastic stirring is much larger at the top (as compared to the bottom) indicating that the workpiece is hotter at the top and thus has a larger region which exhibits viscoplasticity.

The simulated thermal profiles of the cross section (corresponding to figure 5.5a) for the three processing conditions are given in figure 5.5b. As concluded by experimental observations from figure 5.5a, the simulated thermal profiles show higher temperatures at the top in all the three processing conditions. Within the three processing conditions, PW shows the lowest temperature while PA shows the highest. This is in agreement with the

experimental observation (figure 5.5a) that PW shows the smallest processed zone, while PA shows the largest. In general, the simulated temperature profiles qualitatively capture the experimentally observed process zone profiles.

Figure 5.6a shows variation of experimentally measured temperatures with processing time. The temperature measurements were performed using embedded k-type thermocouple at the mid plane of the workpiece at a location very close to the pin (see figure 5.1b). The temperature at the start of the experiment is seen to be the ambient temperature for the specific processing condition. Thus, PA and PW are at room temperature, whereas PLN is at sub-zero temperature.

With increase in time, as the tool approaches the location of thermocouple, the temperature for all the three processing conditions is seen to increase. This increase is a result of the thermal balance between heat generation and heat dissipation (which is different for different processing conditions) coupled with the thermal conductivity of the workpiece. Finally, a maxima in temperature is achieved followed by a decrease, as the tool moves away from the thermocouple. As expected, the measured peak temperature was highest for PA (630K) indicating a low rate of heat dissipation. The peak temperatures for PLN (573K) and PW, (563K) were very close to each other (though PLN was marginally higher). However, the ascending temperature-time profiles for PA and PLN were similar and were very different from PW. Both PA and PLN showed a linear increase in temperature with time, whereas PW showed a bi-linear behavior, with a low rate of increase in the initial stage followed by a rapid increase. This indicated that water (PW) was a more effective medium in keeping the workpiece cool for longer time duration.

Following the peak, the temperatures in all the three processing conditions decreased with time. Similar to the ascending case, the rate of temperature decrease for PA and PLN were similar; however, the exact profiles did not overlap since their peak temperatures were different. The descending temperature profile of PW (similar to the ascending profile) showed a rapid initial decrease followed by a slow decrease. The final temperature, at the end of the FSP, was highest for PA and lowest for PW.

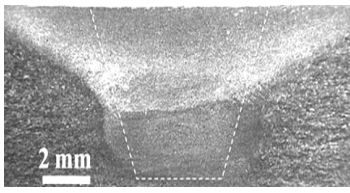
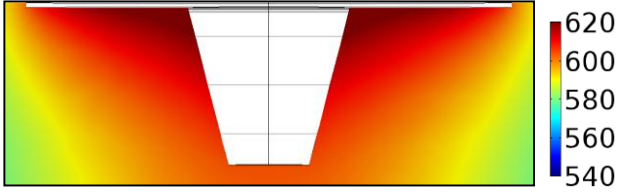
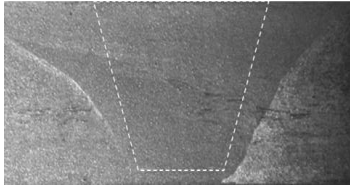
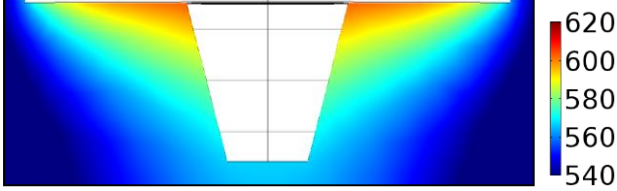
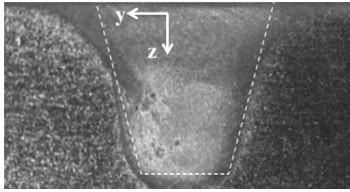
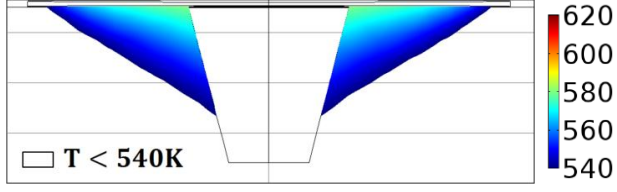
Processing Condition	Experimental Profiles	Simulated Temperature Profiles
Processed in Air (PA)		
Processed in Liquid Nitrogen (PLN)		
Processed in Water (PW)		
	(a)	(b)

Figure 5.5: (a) Cross-sectional images of the FSP zone and (b) FE simulated temperature profiles. These are shown for FSP under air, water and liquid nitrogen. The tool profile is marked in the respective images.

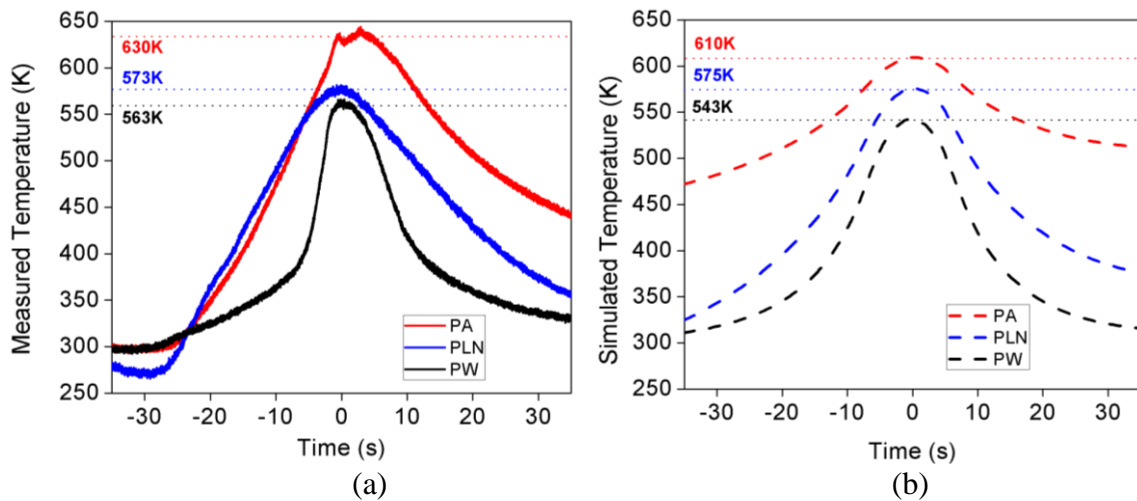


Figure 5.6: (a) Experimental and (b) FE simulated temperature profiles for FSP under air (PA), water (PW) and liquid nitrogen (PLN). In both figures, the peak temperatures are identified.

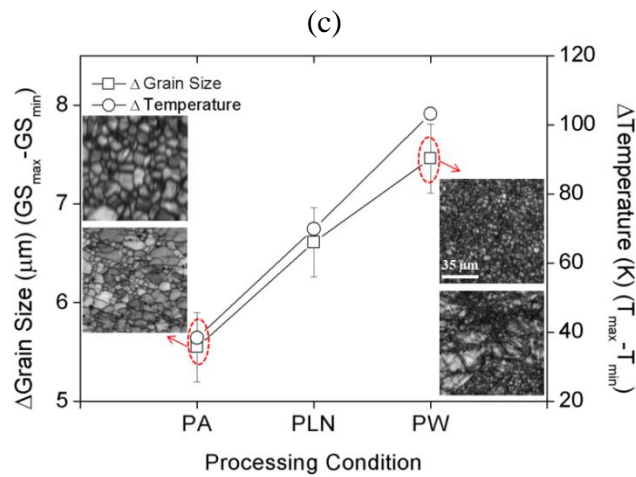
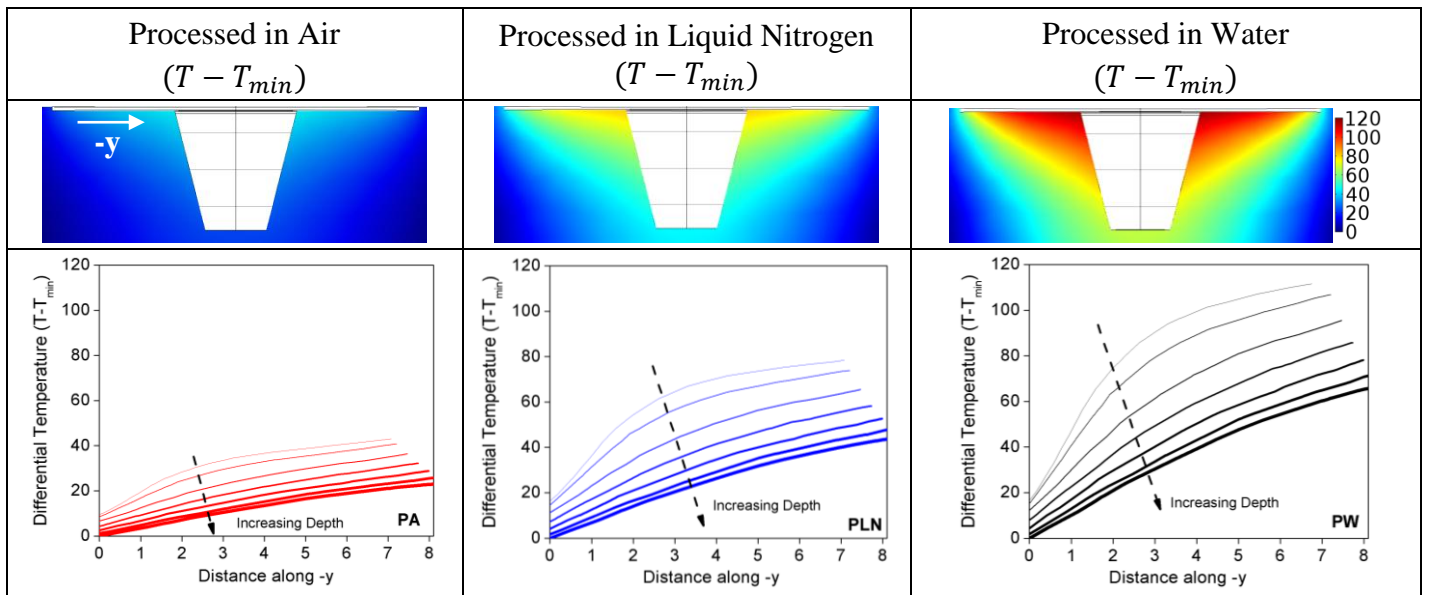
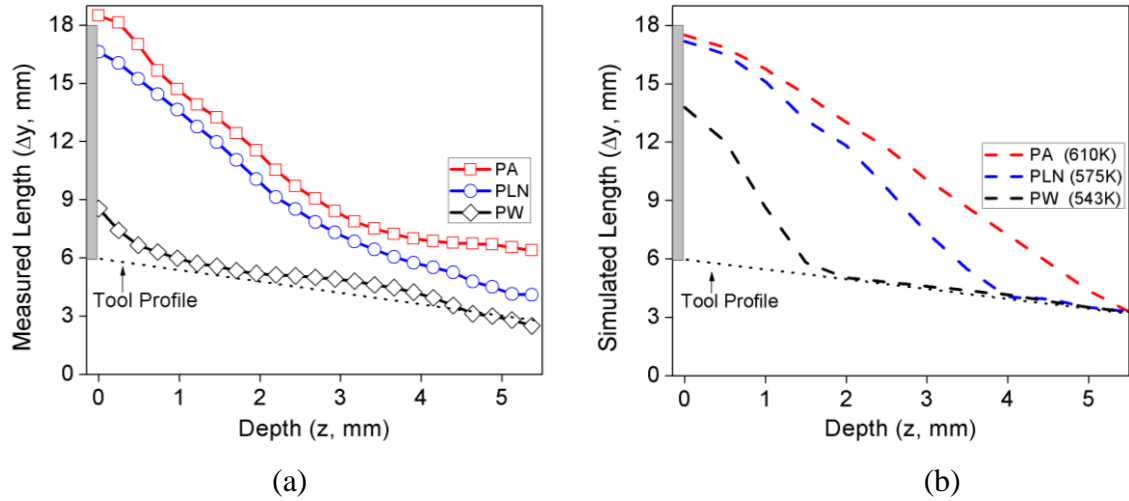
Corresponding to figure 5.6a, the temperature-time profile at the same location in simulation for the three processing conditions is given in figure 5.6b. It should be noted that the simulation is a 3D steady-state model and thus is incapable of capturing the initial transient behavior which is experimentally observed. This is apparent since the initial temperature for PA in experiment is ambient temperature (300K), whereas for the simulation it is much higher (465K). Apart from the initial transient, the simulation shows a reasonable qualitative agreement with the experimentally observed peak temperature and the descending temperature profile for all the three processing conditions.

Figure 5.7a shows process zone dimensions from the experimental profiles (figure 5.5a) at different depths. As can be seen in the figure, water showed smallest and narrowest process zone while air showed the largest and broadest process zone. From the simulations (figure 5.5b), thermal-criteria-based lengths at different depths were estimated corresponding to 610K, 575K and 543K (respectively for PA, PLN and PW). The temperature used in the above thermal-criteria was taken from the peak temperatures as observed in figure 5.6b. It is seen that the experimental process zone dimensions for PA and PLN (figure 5.7a) closely resemble the processed zone dimensions from simulations (figure 5.7b). The process zone dimension for PW, however, is overestimated by simulations.

Figure 5.7c shows the simulated differential-temperature maps within the processed zone. Differential-temperature is defined as the difference in temperature at a location to the minimum temperature present in the given simulation. This is an indicator of temperature variability with space for a given processing condition and provides a common basis for comparison across processing conditions, since absolute temperatures are not involved. These simulation results are rather difficult to validate through direct experiments since a complete plot of temperature distribution cannot be experimentally measured. However, these can be validated through indirect experimental observations through microstructural studies.

Differential-temperature profiles (at various depths) along $-y$ direction are plotted in figure 5.7c. The slope of these curves is the y -axis components of the gradient vector. It is seen that the temperature gradients (along y -axis) decrease with increase in depth for all the processing conditions. Moreover, it is seen that the gradients are highest for PW and lowest for PA. This, as previously noted, cannot be validated through direct experimental

observations. However, experimental observations of microstructural variability can be used to corroborate these results.



(d)-(see next page for caption)

Figure 5.7: (a) Experimental and (b) FE simulated profiles of length versus depth. In (b), respective temperatures (as in figure 5.6b) of 610K, 575K and 543K were used to draw the profiles. (c) Differential temperature ($T - T_{min}$) in the cross-section and also along y-axis (as a function of depth). (d) Change in grain size and temperature between processed zone center and advancing side. These are shown for FSP under air (PA), water (PW) and liquid nitrogen (PLN).

In an attempt to do so, the maximum difference in experimentally measured grain size (ΔG) and maximum difference in simulated temperature (ΔT) was plotted for the three processing conditions (figure 5.7d). It is interesting to see that the maximum difference in simulated temperature scaled linearly with maximum difference in experimentally measured grain size. The finite element simulation, thus have the potential to be coupled with appropriate deformation [13,16,66] and grain coarsening [41,61,67] models for a realistic prediction of the microstructure developments.

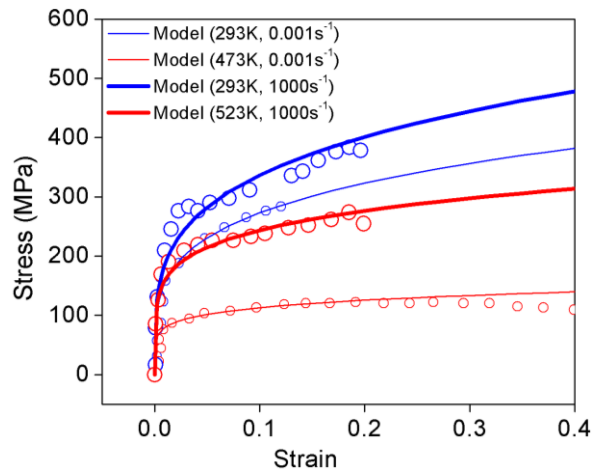


Figure 5.8: Experimental (marked as \circ) true stress versus true strain data of AZ31 compression tests [61]. Data for different temperatures (293K, 473K and 523K) and strain rates (0.001 s^{-1} and 1000 s^{-1}) were ‘fitted’ into constitutive equations of ‘model’.

5.6 Summary

Friction stir processing was conducted under air, liquid nitrogen and water. Observed grain size refinement followed an expected pattern of heat extraction. Embedded

thermocouples showed maximum temperature gradient for water, while the measured processed zone was the narrowest. Coupled heat transfer and viscoplastic fluid flow were incorporated in a steady-state 3-D finite element simulation to model the FSP. The simulations were remarkably successful in capturing the experimental temperature profiles and estimating the processed zone dimensions. It was observed that the maximum difference in simulated temperature scaled linearly with maximum difference in experimentally measured grain size.

In totality, the steady-state thermal simulations were able to capture temperature variation both in space and time for all the three processing conditions. The remarkable agreement between simulations and experiments open an opportunity for steady-state simulation (which are computationally less expensive than the more realistic transient models [38,58]) being used for microstructural modelling of FSP.

5.7 Appendix

The alloy was assumed to be a viscous fluid. Dynamic viscosity was decided by the strain rate and temperature. Available compression test data (at temperatures of 293K, 473K and 523K; strain rates of 0.001s^{-1} and 1000s^{-1}) on AZ31 [62] were ‘fitted’ into appropriate constitutive equations, see figure 5.8. Following were the equations,

$$\sigma = K(T, \dot{\varepsilon})\varepsilon^{C(T, \dot{\varepsilon})} \quad (i)$$

$$C = C_0 + C_1T + C_2 \ln(\dot{\varepsilon}) + C_3T \ln(\dot{\varepsilon}) \quad (ii)$$

$$K = \{K_0 + K_1T + K_2 \ln(\dot{\varepsilon}) + K_3T \ln(\dot{\varepsilon})\} \left\{1 - \left(\frac{T - T_0}{T_m - T_0}\right)\right\}^2 \quad (iii)$$

$$\text{where, } T_0 = 293\text{K, } T_m = 881\text{K}$$

where σ is the true stress, ε is the true strain, T is the temperature, $(\dot{\varepsilon})$ is the strain rate, C_i and K_i are constants where $(i = 0,1,2,3)$, T_m is the melting temperature and T_0 is the ambient temperature.

The values of the constants calculated for the above equations are summarized in the table below.

C₀	C₁	C₂	C₃
0.367475809	-0.00041	-0.00331	1.39E-05
K₀	K₁	K₂	K₃
405.8812	0.459329	-44.3641	0.182514

Thermal conductivity of the alloy was also taken as a function of temperature as input in the model. The corresponding values are given as.

Temperature (in kelvin)	Thermal conductivity (W/mK)
298	84.7
373	90.5
473	95.8
573	98.4
673	98.6

Yield strength decreased with the rise of temperature and the corresponding values used for the alloy as a function of temperature is given in the table below.

Temperature (in kelvin)	Y-bar (MPa)
300	225
375	140
425	95
475	60
525	35
590	15
640	10

References

1. R. S. Mishra and Z. Y. Ma, Mater. Sci. Eng. R Reports **50**, 1 (2005).
2. Z. Y. Ma, Metall. Mater. Trans. A **39**, 642 (2008).
3. R. Nandan, T. Debroy, and H. K. D. H. Bhadeshia, Prog. Mater. Sci. **53**, 980 (2008).
4. Z. Y. Ma, R. S. Mishra, and M. W. Mahoney, Acta Mater. **50**, 4419 (2002).
5. Z. Y. Ma, S. R. Sharma, and R. S. Mishra, Scr. Mater. **54**, 1623 (2006).

6. U. F. H. R. Suhuddin, S. Mironov, Y. S. Sato, H. Kokawa, and C.-W. Lee, *Acta Mater.* **57**, 5406 (2009).
7. C. I. Chang, C. J. Lee, and J. C. Huang, *Scr. Mater.* **51**, 509 (2004).
8. P. Asadi, M. K. Besharati Givi, and G. Faraji, *Mater. Manuf. Process.* **25**, 1219 (2010).
9. P. B. Prangnell and C. P. Heason, *Acta Mater.* **53**, 3179 (2005).
10. J. M. Root, D. P. Field, and T. W. Nelson, *Metall. Mater. Trans. A* **40**, 2109 (2009).
11. S. H. C. Park, Y. S. Sato, and H. Kokawa, *Metall. Mater. Trans. A* **34**, 987 (2003).
12. Y. N. Wang, C. I. Chang, C. J. Lee, H. K. Lin, and J. C. Huang, *Scr. Mater.* **55**, 637 (2006).
13. D. P. Field, T. W. Nelson, Y. Hovanski, and K. V. Jata, *Metall. Mater. Trans. A* **32**, 2869 (2001).
14. Q. Yang, A. H. Feng, B. L. Xiao, and Z. Y. Ma, *Mater. Sci. Eng. A* **556**, 671 (2012).
15. S. H. Chowdhury, D. L. Chen, S. D. Bhole, X. Cao, and P. Wanjara, *Metall. Mater. Trans. A* **44**, 41 (2012).
16. J.-H. Cho, D. E. Boyce, and P. R. Dawson, *Mater. Sci. Eng. A* **398**, 146 (2005).
17. G. Proust, C. N. Tomé, and G. C. Kaschner, *Acta Mater.* **55**, 2137 (2007).
18. W. Woo, H. Choo, M. B. Prime, Z. Feng, and B. Clausen, *Acta Mater.* **56**, 1701 (2008).
19. W. Yuan, R. S. Mishra, B. Carlson, R. K. Mishra, R. Verma, and R. Kubic, *Scr. Mater.* **64**, 580 (2011).
20. G. Bhargava, W. Yuan, S. S. Webb, and R. S. Mishra, *Metall. Mater. Trans. A* **41**, 13 (2009).
21. W. Woo and H. Choo, *Scr. Mater.* **54**, 1859 (2006).
22. Y. S. Sato, A. Sasaki, A. Sugimoto, A. Honda, and H. Kokawa, *Mater. Sci. Forum* **539-543**, 3775 (2007).
23. S. R. Agnew and O. Duygulu, *Mater. Sci. Forum* **419-422**, 177 (2003).
24. R. W. Fonda, J. F. Bingert, and K. J. Colligan, *Scr. Mater.* **51**, 243 (2004).
25. R. W. Fonda and J. F. Bingert, *Metall. Mater. Trans. A* **35**, 1487 (2004).
26. J.-Q. Su, T. W. Nelson, and C. J. Sterling, *Mater. Sci. Eng. A* **405**, 277 (2005).
27. T. R. McNelley, S. Swaminathan, and J. Q. Su, *Scr. Mater.* **58**, 349 (2008).
28. K. V. Jata and S. L. Semiatin, *Scr. Mater.* **43**, 743 (2000).
29. J.-Q. Su, T. Nelson, R. Mishra, and M. Mahoney, *Acta Mater.* **51**, 713 (2003).
30. A. Tripathi, A. Tewari, N. Srinivasan, G. M. Reddy, S. M. Zhu, J. F. Nie, R. D. Doherty, and I. Samajdar, *Metall. Mater. Trans. A* **46**, 3333 (2015).
31. A. Tripathi, A. Tewari, A. K. Kanjarla, N. Srinivasan, G. M. Reddy, S. M. Zhu, J. F. Nie, R. D. Doherty, and I. Samajdar, *Metall. Mater. Trans. A* Submitted, E (2015).
32. F. Chai, D. Zhang, Y. Li, and W. Zhang, *Mater. Sci. Eng. A* **568**, 40 (2013).

33. C. I. Chang, X. H. Du, and J. C. Huang, *Scr. Mater.* **57**, 209 (2007).
34. C. I. Chang, X. H. Du, and J. C. Huang, *Scr. Mater.* **59**, 356 (2008).
35. F. Chai, D. Zhang, and Y. Li, *Materials (Basel)*. **7**, 1573 (2014).
36. A. Arora, T. Debroy, and H. K. D. H. Bhadeshia, *Acta Mater.* **59**, 2020 (2011).
37. R. Nandan, G. G. Roy, and T. Debroy, *Metall. Mater. Trans. A* **37A**, 1247 (2006).
38. M. Song and R. Kovacevic, *Proc. Inst. Mech. Eng. Part B J. Eng. Manuf.* **217**, 73 (2003).
39. R. Nandan, G. G. Roy, T. J. Lienert, and T. Debroy, *Sci. Technol. Weld. Join.* **11**, 526 (2006).
40. R. Nandan, G. G. Roy, T. J. Lienert, and T. Debroy, *Acta Mater.* **55**, 883 (2007).
41. A. N. Albakri, B. Mansoor, H. Nassar, and M. K. Khraisheh, *J. Mater. Process. Technol.* **213**, 279 (2013).
42. M. Song and R. Kovacevic, *Mach. Tools Manuf.* **43**, 605 (2003).
43. P. Heurtier, M. J. Jones, C. Desrayaud, J. H. Driver, F. Montheillet, and D. Allehaux, *J. Mater. Process. Technol.* **171**, 348 (2006).
44. H. B. Schmidt and J. H. Hattel, *Proc. COMSOL Conf.* (2008).
45. H. B. Schmidt and J. H. Hattel, *Scr. Mater.* **58**, 332 (2008).
46. H. N. B. Schmidt, T. L. Dickerson, and J. H. Hattel, *Acta Mater.* **54**, 1199 (2006).
47. H.-H. Cho, S.-T. Hong, J.-H. Roh, H.-S. Choi, S. H. Kang, R. J. Steel, and H. N. Han, *Acta Mater.* **61**, 2649 (2013).
48. K. Mundra, T. DebRoy, and K. M. Kelkar, *Numer. Heat Transf. Appl. An Int. J. Comput. Methodol.* **Part A**, 115 (1996).
49. P. Ulysse, *Mach. Tools Manuf.* **42**, 1549 (2002).
50. C. M. Chen and R. Kovacevic, *Mach. Tools Manuf.* **43**, 1319 (2003).
51. X. Deng and S. Xu, *J. Manuf. Process.* **6**, 125 (2004).
52. P. A. Colegrove and H. R. Shercliff, *J. Mater. Process. Technol.* **169**, 320 (2005).
53. G. Buffa, J. Hua, R. Shivpuri, and L. Fratini, *Mater. Sci. Eng. A* **419**, 389 (2006).
54. H. W. Zhang, Z. Zhang, and J. T. Chen, *J. Mater. Process. Technol.* **183**, 62 (2007).
55. M. Assidi, L. Fourment, S. Guerdoux, and T. Nelson, *Int. J. Mach. Tools Manuf.* **50**, 143 (2010).
56. D. Kim, H. Badarinarayan, J. Kim, C. Kim, K. Okamoto, R. H. Wagoner, and K. Chung, *Eur. J. Mech. Solids* **29**, 204 (2010).
57. B. C. Liechty and B. W. Webb, *J. Mater. Process. Technol.* **208**, 431 (2008).
58. Z. Yu, W. Zhang, H. Choo, and Z. Feng, *Metall. Mater. Trans. A* **43A**, 724 (2012).
59. Z. Yu, W. Zhang, H. Choo, and Z. Feng, *Metall. Mater. Trans. A* **43**, 724 (2012).
60. W. X. Pan, D. S. Li, M. Tartakovsky, S. Ahzi, M. Khraisheh, and M. Khaleel, *Int. J. Plast.* **48**, 189 (2013).

61. S. Aljoaba, O. Dillon, M. Khraisheh, and I. S. Jawahir, *J. Mater. Eng. Perform.* **21**, 1141 (2011).
62. I. Ulacia, S. Yi, M. T. Perez-Prado, N. V Dudamell, F. Gálvez, D. Letzig, and I. Hurtado, in *4th Int. Conf. High Speed Form.* (2010), pp. 189–197.
63. T. V Padfield, *ASM Handb.* **9**, 801 (2004).
64. A. J. Schwartz, M. Kumar, and B. L. Adams, *Electron Backscatter Diffraction in Materials Science*, Second Edition (Springer, 2000).
65. O. Engler and V. Randle, *Introduction to Texture Analysis Macrotecture, Microtexture and Orientation Mapping*, Second Edition (Taylor and Francis Group, 2010).
66. J.-H. Cho and P. R. Dawson, *Metall. Mater. Trans. A* **37**, 1147 (2006).
67. B. M. Darras, *J. Mater. Eng. Perform.* **21**, 1243 (2011).

Chapter 6

Study of grain structure evolution during study of a twin roll cast Mg alloy

6.1 Abstract

The evolution of microstructure under static annealing was studied for mid-thickness section of a twin-roll-cast (TRC) magnesium alloy. Annealing was performed at 300°C and 500°C for different times. Microstructural evolution was quantitatively analyzed, from optical micrographs, using grain path envelope analysis. Additional information from electron backscatter diffraction (EBSD) was used for addressing the possible mechanism(s). It was found that the TRC structure had a bimodal grain size, which was preserved even after annealing at 300°C. However, the annealing at 500°C led to a unimodal grain size. This difference in the grain size distribution created a contrasting behavior in the normalized standard deviations. This was primarily attributed to a competition between recovery and

recrystallization, and their respective dominance at 300° and 500°C. A deformation induced recrystallization recovery (DIRR) model was proposed. The proposed model could successfully address the experimental microstructural evolution.

6.2 Introduction

Magnesium (Mg) alloys have attractive properties: high specific strength and stiffness, castability, machinability and recyclability. However, their use in light weight structural applications, especially in the automobile sector, has been limited [1–3]. Sheet metal production using conventional direct chill (DC) casting is complex for Mg alloys. DC cast Mg has poor workability and low heat capacity, often requiring repeatable reheating during hot rolling [4]. This restricts commercial Mg alloy sheet production [5].

Twin-roll-casting (TRC) is an emerging manufacturing technology for producing metal sheets, strips or plates [4,6]. TRC is known to produce superior properties than the conventional ingot or DC casting. In this process, both casting and rolling is done in a single step. The molten metal is fed between the gaps of internally cooled rolls, eventually leading to rapid solidification and hot deformation [7]. This has the potential of avoiding subsequent rolling. It needs to be noted that TRC involves significantly higher solidification rate: 10^2 to 10^3 K/s in TRC as opposed to ~ 50 K/s in conventional ingot casting. Though often considered as a practical processing route Mg sheet production, TRC is also known to impose through thickness heterogeneity in microstructure. Post-TRC annealing has been used to redeem such heterogeneities. However, studies addressing microstructure evolution during grain coarsening of typical TRC Mg-sheet remains limited [8–11]. This was the motivation behind this study.

Grain coarsening has a rich reservoir of published literature. With the initial work of Greenwood and LSW [12–14], an understanding about the physics based nucleation and growth was achieved for very dilute systems. However, this was inadequate to look at polycrystalline grain coarsening. Naturally, geometric approaches to grain coarsening and microstructure evolution were formulated [15–24]. These approaches assume some functionality for nucleation and growth rate (which could even vary with time and space [22,23]) and then using stochastic point processes to predict microstructure evolution: volume

fraction, interfacial surface area, mean curvatures, etc. Geometric models addressing experimental data also came up with the development of the Growth Path Envelop (GPE) formulation [25]. This used inverse cumulative size distribution and provided an ability to track growth of each grain size class with time for a general nucleation and growth system (see appendix for details). This resembled, in many ways, to the equation of continuity for fluid system [18,26]. This very powerful analysis framework for studying microstructure evolution has been used in many polycrystalline and particle system and is still an area of active research [27].

In the present study, the evolution of microstructure under static annealing of twin roll cast (TRC) AZ31 Mg alloy was studied. The concept of grain path envelope was used to quantitatively understand the evolving structure. The competition between recovery and recrystallization was assessed using microtexture data.

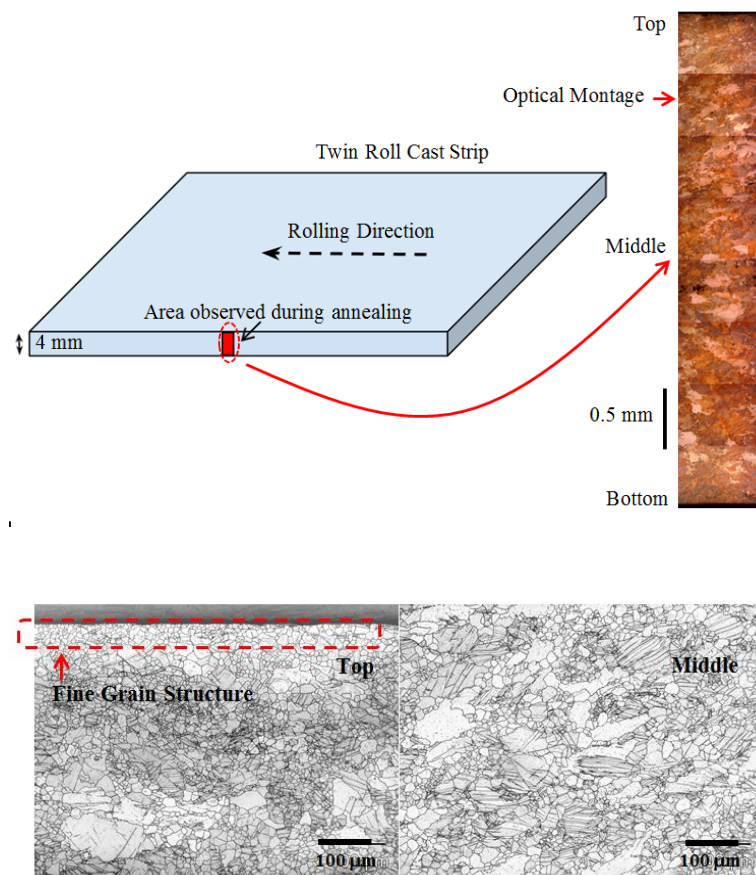


Figure 6.1: Schematic of the twin-roll-cast (TRC) sheet indicating rolling direction (RD) and the area observed through optical microscopy. Montage of optical images and magnified images from middle and top are also included.

6.3 Experimental procedure

Twin roll casting of AZ31 magnesium alloy (for composition refer table 6.1) sheet was performed by Commonwealth Scientific and Industrial Research Organization (CSIRO) casting facility at Clayton (Melbourne, Australia). The sheet produced was 4 mm thick and 35 cm in width. Small samples (length 10 mm, width 7 mm and thickness 4 mm) were cut from the sheet and annealed at temperatures of 300°C ($\sim 0.6T_m$) and for 1, 2 and 16 hours, and at temperature of 500°C ($\sim 0.85T_m$) (T_m is the liquidus temperature of AZ31 alloy) for 0.25, 0.5, 2 and 16 hours. The samples were kept in the muffle furnace after the specified temperature was reached. The samples were kept for the specified amount of time and then immediately quenched in water.

Annealed samples were hot mounted (CitoPress-10 by StruersTM) for microstructural observations. Metallographic polishing was performed in steps by going from 1000 to 4000 silicon carbide grit paper to diamond polishing with 1 μ m paste in oil based lubricant followed by final polishing with 0.05 μ m colloidal silica solution. Samples were etched for optical microstructural observations with acetic picral solution (4.2 g picric acid, 20 ml distilled water, 50 ml ethanol and 10 ml acetic acid) for 5 seconds. Microstructural characterization was performed using high resolution montage of the complete through thickness surface (long transverse) as shown in figure 6.1. True 3D mean intercept length measure L3 [28] was measured by grain intercept count method. The intercept counts were manually selected on a series of horizontal lines drawn on the micrographs and counted using programs written in ImageJTM [29]. This provided a large statistically robust data set of over 2000 measurements which were used to calculate mean-intercept-length statistics and growth path envelope.

Table 6.1: Chemical composition (in wt% alloying elements) of the twin-roll cast AZ31 magnesium alloy

Al	Zn	Mn	Ca	Si	Cu
3.1	0.7	0.4	0.04	0.1	0.01

Micro-texture and misorientation distribution of the grains were studied using Electron Back Scatter Diffraction (EBSD) for which polished samples (without etching) were ion-milled (Ar^+ ion in a GatanTM PECS 682, at 6 keV with 70° tilt) followed by plasma cleaning (GatanTM Solaris). EBSD measurements were performed in FEITM Quanta 3D-FEG (field emission gun) SEM (scanning electron microscope) using EDAX-OIMTM EBSD system. Areas of 500 μm by 500 μm were scanned at 0.5 μm step size for each annealed sample from the central region of long-transverse section. Beam and scanning conditions were kept identical between the scans.

6.4 Results and discussion

Figure 6.1 presents a montage of through thickness microstructures. Though this montage comprised of over 8000 pixels, it was digitally compressed to fit in the figure. Barring regions very close to the top and bottom surfaces - which were finer, the microstructure was statistically similar along the thickness. EBSD images, as inverse pole figure (IPF) maps, of the twin-roll-cast (TRC) alloy and all the annealed samples (at various temperatures and times) are given in figure 6.2. The as-received TRC specimen (see figure 6.2) had bimodal grain-size distribution. More specifically, it had a few large grains surrounded by many very fine grains. The large grains were slightly elongated along the rolling direction, whereas the fine grains were reasonably equiaxed with no shape anisotropy. A closer observation also revealed that the finer grains were uniformly colored, while the large grains had varying shades. In other words, the large TRC grains showed presence of orientation gradients and in-grain misorientations. Some of them also had twins. Figure 6.2 also shows the EBSD images after 300°C and 500°C annealing. The bimodal grain size distribution was retained after 300°C annealing, while 500°C annealing created more equiaxed and uniform grain size distribution. Annealing at 500°C for 16 hours also led to the elimination of orientation gradients in all the grains.

Mean-intercept-length (MIL) measurements from various stages of annealing are collated in figure 6.3a. It needs to be noted that each measurement point consisted of at least 2000 grains. The MIL value of the TRC sheet was 24.8 μm , as indicated by the dotted line in figure 6.3a. Annealing caused the MIL to initially decrease followed by a monotonic increase. It is important to note that the drop in MIL was more for the sample annealed at 500°C (and

for shorter annealing time). The final MIL at 16 hours was also marginally higher for 500°C annealing.

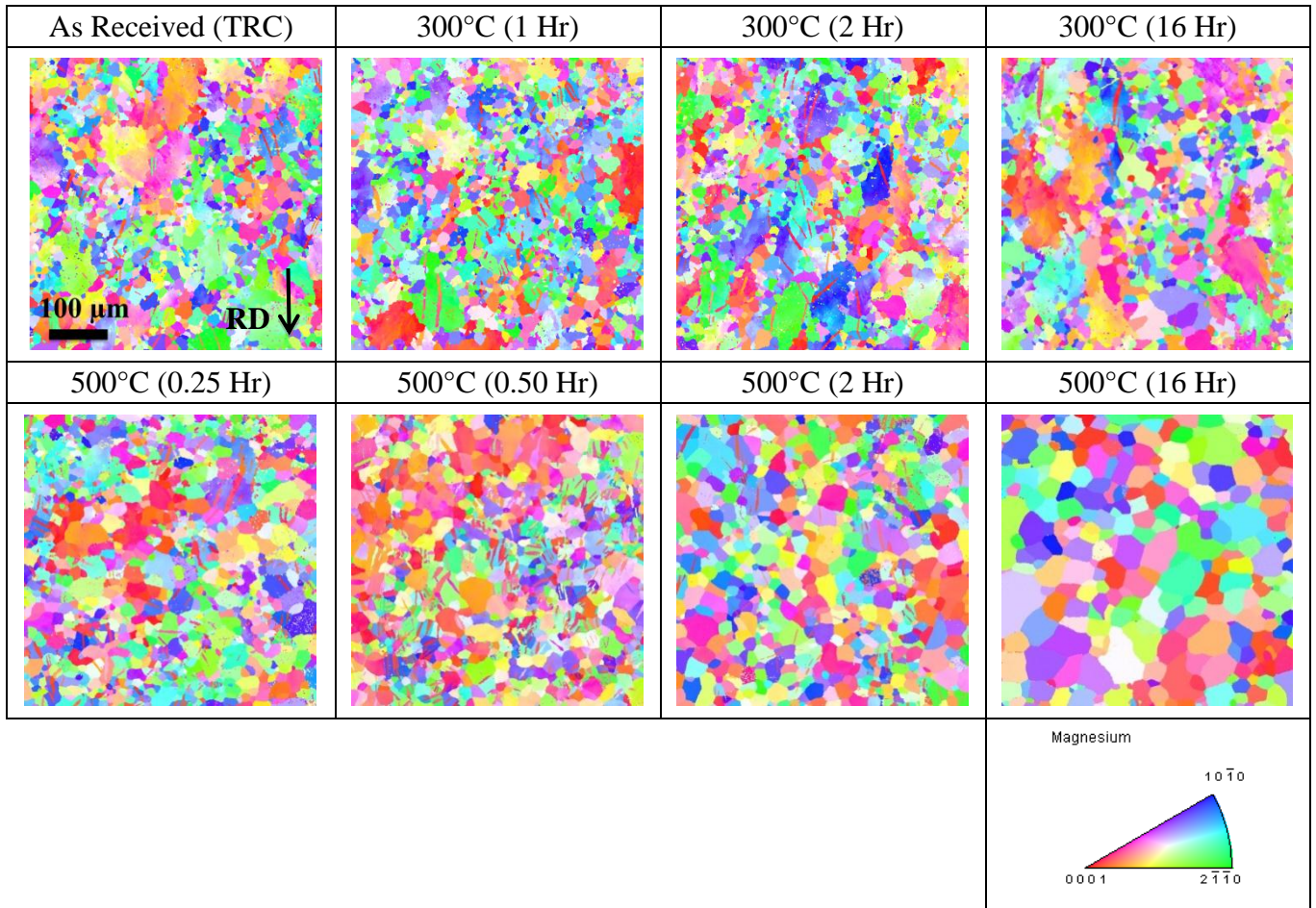


Figure 6.2: EBSD images in inverse pole figure (IPF) notation of as received TRC sheet (mid thickness section) and after annealing treatment at different temperature/time

Figure 6.3b shows the variation in normalized standard deviation of intercept-length distribution (normalized with their corresponding MIL) as a function of annealing time. The normalized standard-deviation of intercept-length distribution for the as received sample was 0.96; 500°C reduced this value: 0.69 to 0.60 with progressive annealing. This is a classical grain coarsening behavior. With progress in grain coarsening, as the whole sample approaches a single grain, the standard deviation is expected to approach zero. The drop in the standard deviation after 500°C annealing is thus an expected trend. However, the standard-deviation for samples annealed at 300°C shows a completely opposite trend with a monotonic increase with annealing time (from 0.91 to 1.1). This implies that, although the MIL followed a similar

trend for samples annealed at both the temperatures, the inherent mechanism(s) was not the same. At 300°C the intercept-length distribution was widening, while at 500°C it narrowed.

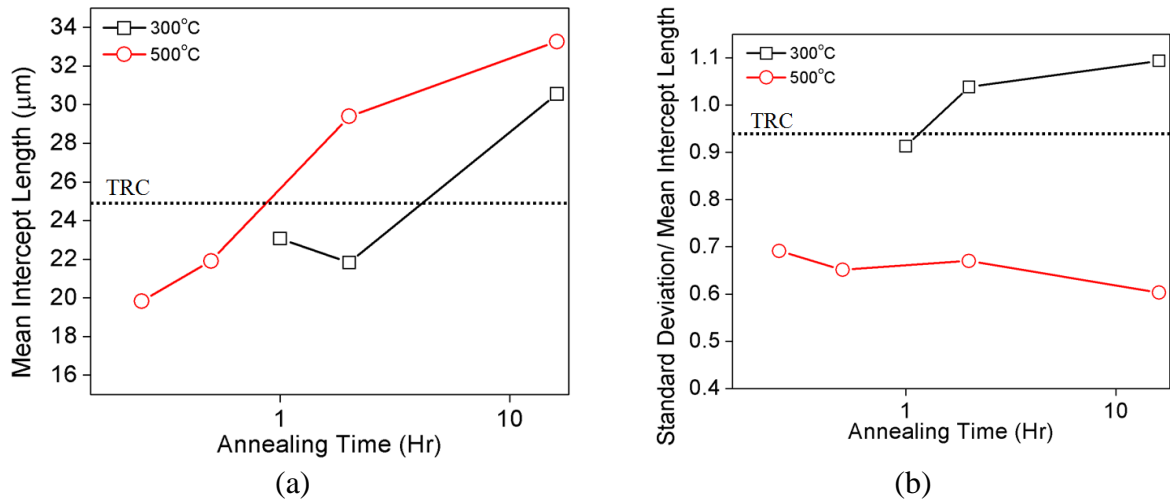


Figure 6.3: (a) Mean intercept length and (b) standard deviation (normalized by mean intercept length) versus annealing time. Measurements were obtained from optical micrographs subjected to 300°C and 500°C annealing respectively. Values for the pre-annealing TRC sheet is shown as dotted lines.

This anomalous behavior of mean and standard deviation of the intercept-lengths for the two temperatures can be quantitatively analyzed by observing the complete intercept-length distribution (figure 6.4). The intercept-length distribution was seen to have the classical log-normal shape for all the temperatures and annealing times. It is intriguing to note that the intercept length distribution did not show bimodal distribution for any samples, otherwise seen often in the microstructures (see figure 6.2). In grain size distribution each grain contributes one value. The intercept-length distribution, on the other hand, is formed by collection of a large number of intercepts (of varying length) from each grain and thus diminishing the bimodal character of the distribution.

For the samples annealed for 16 hours (figure 6.4), the fraction of large grains (towards the tail) was more for 300°C annealing. As the mean-intercept-length of 300°C annealing was smaller, the samples annealed at 300°C also had a large fraction of small grains. The combination naturally increased the standard deviation for samples annealed at 300°C.

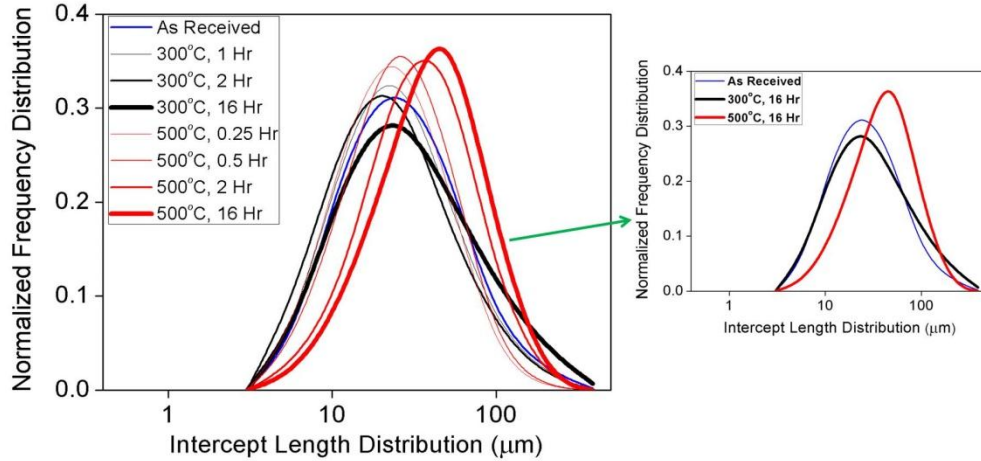


Figure 6.4: Normalized frequency distribution of mean intercept length after 300°C and 500°C for various annealing times. The insert shows the frequency distribution after 16 hour annealing.

The observation of intercept-length distribution merely confirmed the anomalous behavior of mean and standard deviation, but failed to provide a mechanistic explanation for the observation. Thus, to understand the mechanism of grain coarsening, grain-envelop analysis was performed [25,30–32] by tracking each grain-size class with time.

Intercept-length distribution was used to obtain inverse-cumulative size distribution $N_{L>}(R, t)$ [25]: required to calculate grain path envelope (see appendix). $N_{L>}(R, t)$ represents the number of intercepts (per unit test line length) greater than size R at time t . This value, in a nucleation and growth system, is the number associated with nucleated grains which of the concerned grain-size bin. Being an inverse-cumulative size distribution, $N_{L>}(R, t)$ monotonically decreased (see figure 6.5) with increasing mean-intercept-length for all annealing temperatures and times. From figure 6.5a and figure 6.5b, it is clear that the number of smaller intercepts increased initially (as compared to the TRC). It is also clear (see figure 6.5) that the initial increase in number of smaller intercepts was much larger for 500°C annealing. On the other hand, the number of large intercepts (greater than 100 μm) showed a drastic decrease for samples annealed at 500°C. These results indirectly suggest advent of recrystallization: large twin-rolled grains being consumed by nucleation of finer recrystallized grains. Arguably, the process was more active for annealing at 500°C.

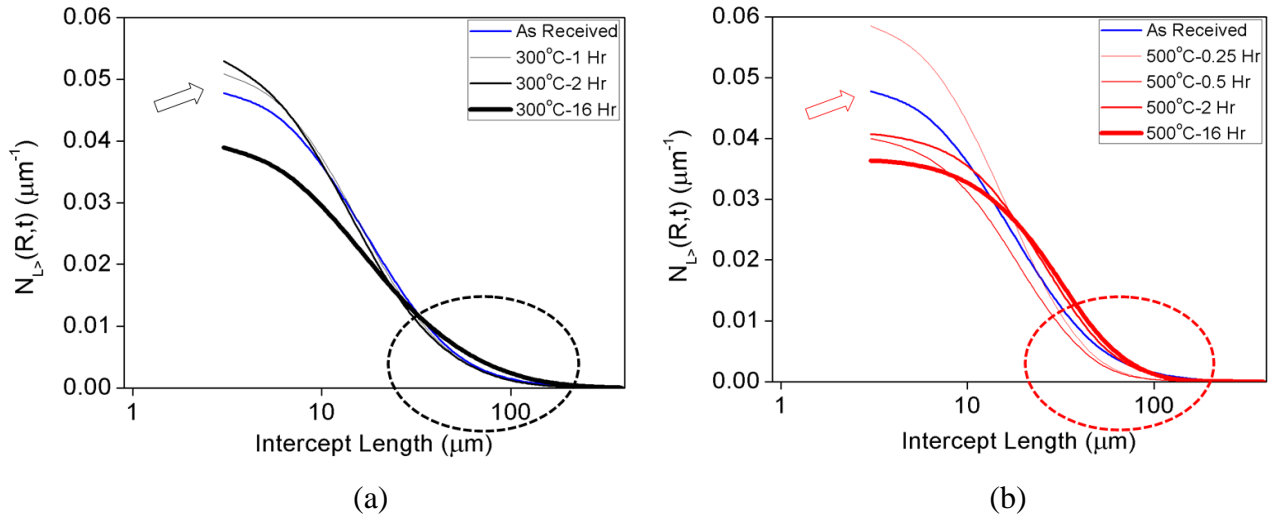


Figure 6.5: Inverse size distribution function having intercept length more than R as a function of R (intercept length) at annealing temperature of (a) 300°C and (b) 500°C.

Grain path envelope [25] was derived (from figure 6.5) for the two annealing temperatures by drawing series of horizontal lines which gave the constant $N_{L>}(R, t)$ contour. This was done for large set of $N_{L>}(R, t)$ to get the entire growth envelope. Figure 6.6 shows the grain path envelope deduced from the inverse-cumulative frequency distribution curve at both the annealing temperatures. It shows the evolution of grains with annealing time. The mean-intercept-length observed at a particular annealing time and temperature is also marked. Grain path envelope contour shows that above a critical size, intercept-length increased and below the critical size, intercept-length decreased. The widening of the range of the intercept-length distribution at higher annealing time for the annealing temperature of 300°C was also clearly observed.

Grain path envelop indicated the initial drop with annealing time at both the annealing temperatures. However, this drop is seen for all the intercept-length bins. Thus the contrasting evolution observed experimentally with mean and standard deviation behaving differently for the two temperatures is validated quantitatively by the grain path envelope analysis. However, it fails to provide any plausible mechanism of grain structure evolution at the two given annealing temperatures.

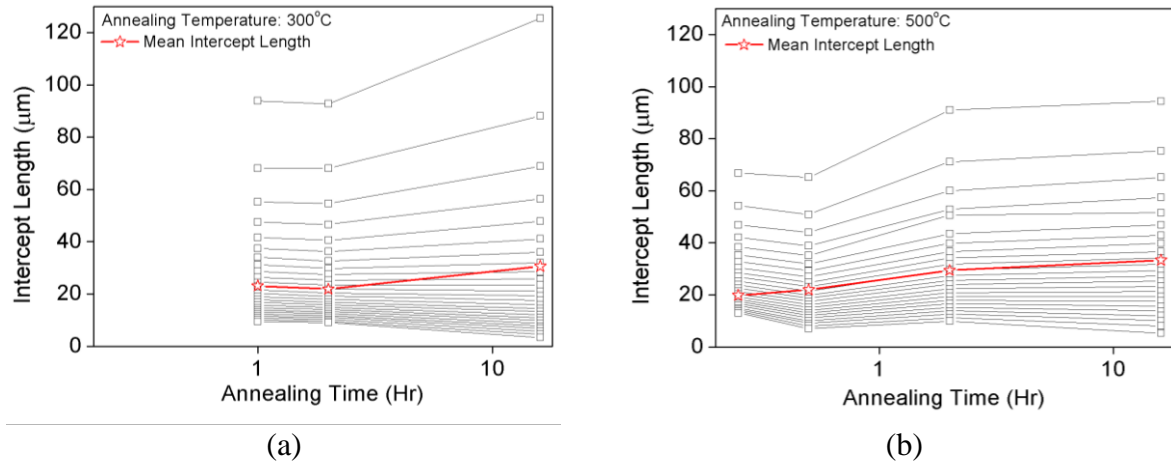


Figure 6.6: Grain evolution envelope at annealing temperature of (a) 300°C and (b) 500°C. Mean intercept length at the given annealing time is also given.

The grain path envelope analysis essentially assumes that the largest mean-intercept-length bin would always be the largest with its mean-intercept-length growing and the number of grains in the bin will be constant. This is true for the grain coarsening where the large grains grow at the expense of smaller grains due to Gibbs-Thompson effect. This, however, is not true in these experiments since the large grains have large deformation which triggers recrystallization in the as received material, thus reducing the number of large grains. Thus, grain path envelope analysis is not capable (in its current formulism) of explaining the anomalous behavior of mean and standard deviation observed for the two annealing temperatures.

The incapability of GPE analysis (in its current formulism) is primarily due to two basic limitations. This first limitation is that it cannot handle the observation that two grains of similar size could have different growth rates. This would mean that the growth paths for a size class can split in to two and also intersect, which violates the basic assumption of GPE analysis. This can be achieved by a Modified GPE analysis where a probabilistic growth rate model for each size class (rather than deterministic growth rate) is used. Hence two grains, which nucleated at the same time (in past) and currently have the same size, may still have different sizes in future due to probabilistic growth rates. The modified GPE with a growth path described in a higher dimension by not just the present size but also the time of nucleation of the grain, would resolve the problem of intersecting growth paths.

The second limitation of the current GPE analysis is in its approach to handle grain annihilation. The analysis assumes that the grain annihilation occurs when a large grain fully consumes a smaller grain due to Gibbs Thompson effect. This means that for annihilation a grain reduces to zero size and then ceases to exist. However, in this study it is observed that some large grains (containing plastic deformation) can trigger nucleation of many smaller grains and thus cease to exist. The modified GPE analysis thus needs to also account for this type of grain annihilation to mimic the microstructure evolution studied in the current work.

In order to have a better understanding than provided by GPE analysis, micro-texture of the annealed samples was studied. Figure 6.7 indicates the area fraction based distribution of grain size from the EBSD scans, for the as-received, 300°C-16 hour annealing condition and 500°C-16 hour annealing condition. Bimodal grain size distribution² was clearly seen for the as-received sample (figure 6.7a) and was seen to exist up till annealing time of 16 hours for samples annealed at 300°C (figure 6.7b). However, for the annealing condition of 500°C for 16 hours, the grain size distribution was largely unimodal (figure 6.7c). This confirms the increase of the normalized standard deviation of intercept length (figure 6.3b) for the annealing at 300°C and its decrease for the annealing done at 500°C.

To further study the misorientation distribution with annealing time, the EBSD scan data was partitioned for each bin size as used in figure 6.7. For each partitioned data set, Kernel Average Misorientation (KAM) was measured. Average misorientation between any pixel point and its neighbours (six in case of the hexagonal grid used) was considered as KAM, provided any of these misorientations do not exceed 5°. KAM calculated for the i^{th} pixel was defined by $KAM_i = \frac{1}{6} \sum_j (g_i - g_j)$ where $(g_i - g_j)$ represents the misorientation between the i^{th} pixel and its neighbouring points (total six combinations) for a hexagonal grid system. The value of KAM for each partition was plotted against the corresponding bin size as given in figure 6.8 (a, b, c) for the as-received sample and samples annealed at 300°C and 500°C for 16 hours.

² It should be noted that in this figure the ordinate is area fraction contribution (and not the number fraction) by each grain size bin. Since area is proportional to square of the size, large grain-size bins will have a greater weight, thus bringing out the bimodality in grain size which otherwise could be missed in a number fraction based grain-size distribution.

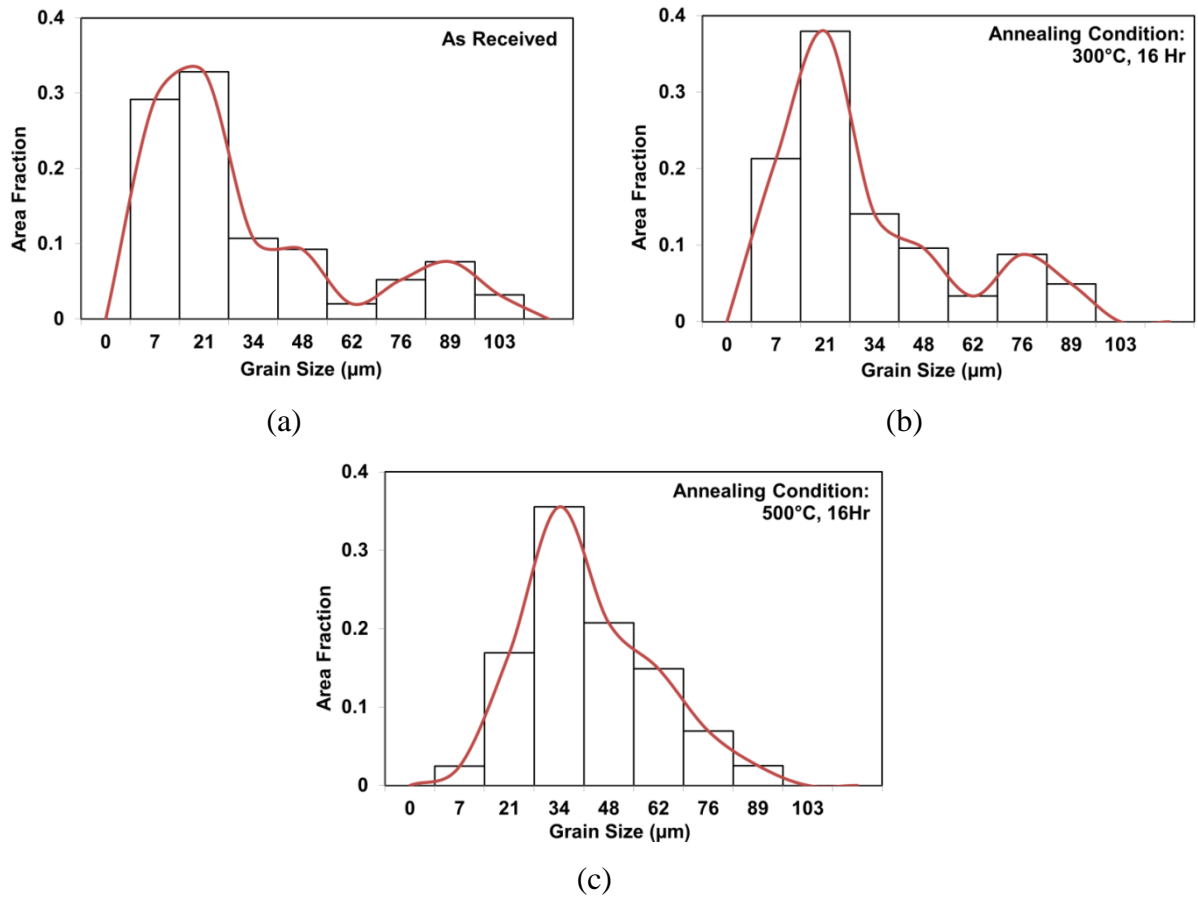


Figure 6.7: Variation of area fraction of the grain size bins for (a) as received TRC and for the annealing time of 16 hours for the two annealing temperatures of (b) 300°C and (c) 500°C.

The KAM distribution for each grain size class/bin for the as-received sample (figure 6.8a) showed a step behavior with small grains having low KAM and large grains having high KAM. This implies that the small grains are recrystallized strain free grains. Whereas, large grains are un-recrystallized grains from cast structure which are deformed during twin-roll process. This is further validated by the observation that small grains are equiaxed whereas large grains are elongated in the rolling direction (see the insert in figure 6.8).

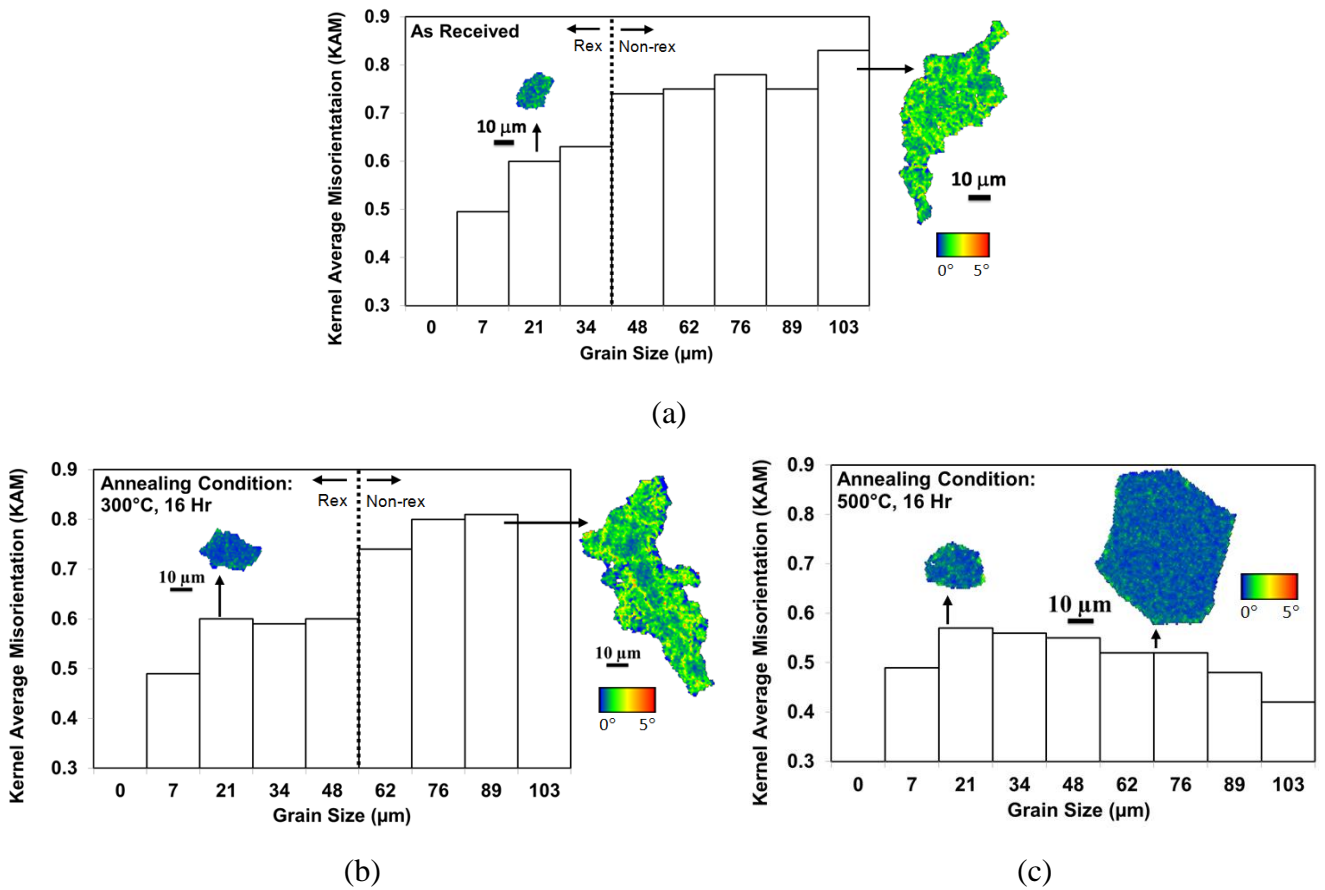
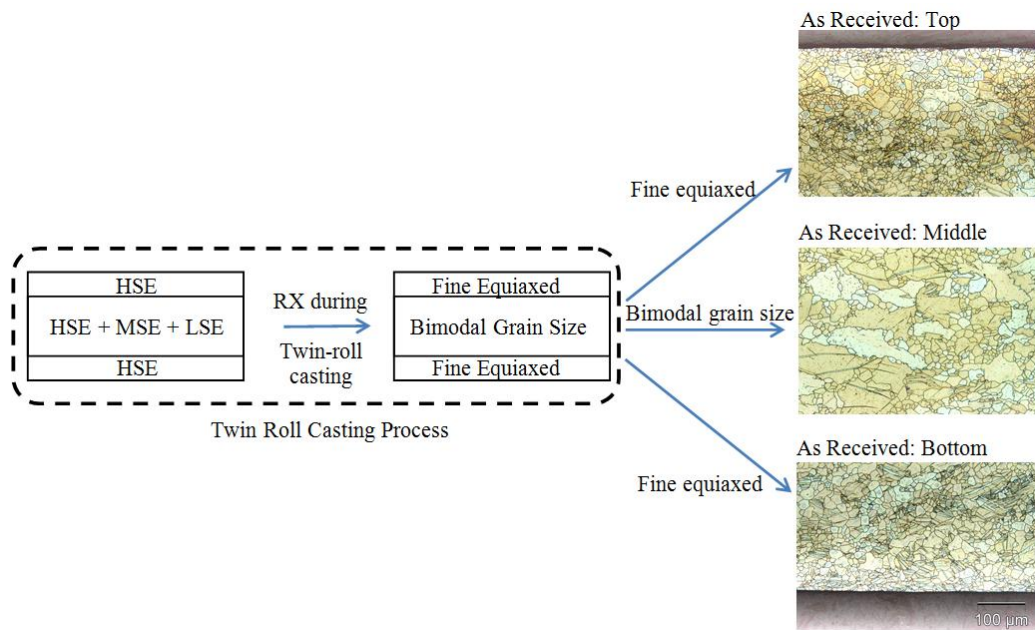
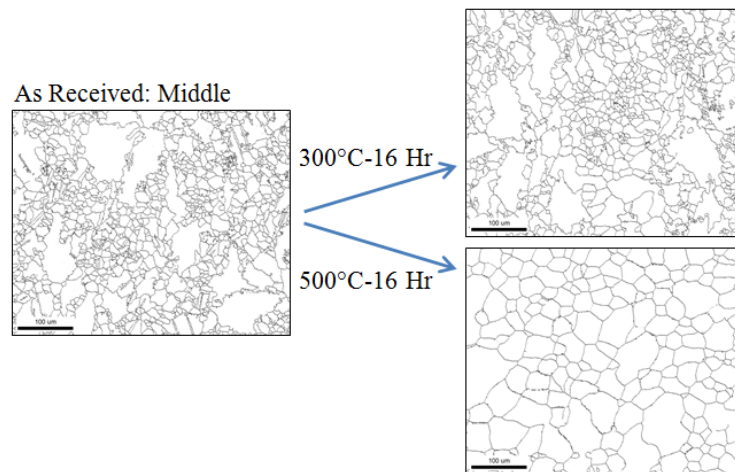


Figure 6.8: Variation of Kernel Average Misorientation (KAM) as a function of grain size for (a) as received TRC and for the annealing time of 16 hours for the two annealing temperatures of (b) 300°C and (c) 500°C. The figures distinguish between small and large grains.

The transition from low KAM to high KAM was seen at a crossover grain size of 41 μm for the as-received sample (figure 6.8a). This KAM analysis when conducted for samples annealed at 300°C for various times revealed that this crossover grain size kept increasing with annealing time, with its value reaching 55 μm for annealing time of 16 hours (figure 6.8b). This corroborates with the observed bimodal grains size distribution for the as-received sample and the sample annealed at 300°C (figure 6.7 (a, b)). This analysis when performed for 500°C case, however, showed a low KAM value for all grain size bins at the annealing time of 16 hours (figure 6.8 c).



(a)



(b)

Figure 6.9 (a) Schematic of the TRC resulting in fine equiaxed grains at the top and bottom of the sheet and bimodal grains at the middle region. (b) shows the microstructural evolution of the middle region after 300°C (16 hours) and 500°C (16 hours) annealing. Actual microstructures, taken at the same magnification, are used to describe the microstructure evolution.

6.4.1 Microstructure evolution model

The difference in the evolution of as-received twin-roll cast microstructure at the two annealing temperatures can be summarized as follows.

1. The as-received twin-roll cast microstructure shows a bimodal grain size distribution with fine equiaxed strain free grains and large elongated strained grains.
2. The annealing at 300°C results in static recrystallization followed by growth. The recrystallization does not completely destroy the deformed structure and preserves some large elongated strained grains. This results in an increase in both mean grain size and its standard deviation after 16 hours of annealing.
3. The annealing at 500°C also results in static recrystallization followed by grain growth. However, at this temperature all the deformed grains are consumed to nucleate (and grow) strain free grains. This leads to a structure with equiaxed grains where mean grain size increases and the standard deviation decreases with time.

A deformation induced recrystallization recovery (DIRR) mechanistic model for the above process is proposed as is schematically shown in figure 6.9. The DIRR model can be divided into the following stages:

1. The twin-roll casting process produces large cast grains of varying orientations, which subsequently are deformed due to the rolling action.
2. The deformation induces strains of varying magnitude depending on the orientation, size and spatial locations of the cast grains. This leads to varying degree of stored strain energy in the cast grains. Based on the stored strain energy, the grains can be classified as high strain energy (HSE) grains, medium strain energy (MSE) grains and low strain energy (LSE) grains.
3. The twin-roll caster continuously cools the cast strip so that the strip is substantially cool as it exits the caster [33]. Since the temperature at which recrystallization occurs decreases as strain increases [34], the exit temperature, which is not very hot, can only trigger recrystallization in grains with high strain energy (HSE grains). Due to the mechanics of rolling deformation, the structure at the top and bottom surface has HSE grains. Thus, it results in formation of fine equiaxed grains at the top and bottom surface. Whereas, the middle region of the sheet (grains depending on the grain orientation, spatial location and neighborhood) has a collection of all HSE, MSE and LSE grains. Hence, a bimodal grain

size distribution develops in the middle region (figure 6.9a) with fine equiaxed strain free grains (due to recrystallization of HSE grains) and large elongated deformed grains (due to MSE and LSE grains).

4. The subsequent annealing at 300°C ($\sim 0.6T_m$) triggers recrystallization in MSE grains (but not LSE grains since their stored strain energy is very low). Thus, the resulting structure is a combination of fine equiaxed grains and large elongated strained grains (from the LSE grain collection), figure 6.9b. The large elongated strained grains, though cannot trigger recrystallization, undergo recovery process thus reducing its stored strain energy. The structure undergoes grain growth with time, but since it has a bimodal grain size, it leads to non-uniform growth kinetics due to Gibbs-Thomson effect³.
5. The annealing at 500°C ($\sim 0.85T_m$) is so high a temperature that it triggers recrystallization in both MSE and LSE grains. Thus resulting in an equiaxed poly-crystalline grain structure as shown in figure 6.9b.

6.4.1.1 Initial stages of annealing

The evidence to support the above model is observed in figure 6.5, where there is a decrease in the fraction of large grains and an increase in the fraction of small grains at the start of annealing for both temperatures. However, the decrease in the fraction of large grains and the increase in the fraction of small grains is far greater in sample annealed at 500°C than the sample annealed at 300°C. This is in agreement with the model which states that the nucleation process at 300°C would be limited to a smaller fraction of deformed grains (MSE grains) as compared to nucleation at 500°C which would be in all deformed grains (MSE and LSE grains).

6.4.1.2 Long term annealing

After annealing for 16 hours (at both the temperatures) as predicted by the model, the mean grain size increases for both annealing temperatures. However, as the grain size distribution at 300°C is bi-modal, the disparity in grain size increases, due to anomalous

³ The Gibbs-Thomson effect suggests that larger grains would have higher growth kinetics than smaller grains, which would cause an anomalous grain growth.

growth kinetics, leading to an increase in standard deviation of grain size distribution (as observed by the normalized intercept length distribution).

The DIRR model rests on the premise that only a fraction of deformed grains participate in recrystallization in the twin-rolled sample and the sample annealed at 300°C. This means that some large deformed grains survive the annealing at 300°C. Whereas, no deformed grain survives the annealing at 500°C. This can be validated by observing the shape and misorientation of large grains at the end of 16 hours for the two temperatures. As predicted, it is seen in figure 6.8a and figure 6.8b, that all the large grains in twin-rolled samples and the sample annealed at 300°C have elongated morphology with higher misorientation (which is an indicator of deformation). On the other hand, all the large grains at 500°C are equiaxed with low misorientation (figure 6.8c) indicating that they are recrystallized grains.

6.5 Summary

Annealing of twin roll cast magnesium alloy (AZ31) was performed at temperatures of 300°C and 500°C at different times, and their microstructure evolution was studied. It was found that at the end of 16 hours of annealing the mean grain size grew for both the annealing temperatures; however, the normalized standard deviation of grain size increased for samples annealed at 300°C whereas it decreased for sample annealed at 500°C. It was also found that the large grains were elongated and had large misorientation for sample annealed at 300°C whereas the large grains were equiaxed with low misorientation for sample annealed at 500°C. This was described based on the competition between recovery and recrystallization, where recovery is dominant factor at 300°C whereas recrystallization is dominant at 500°C. Based on the these observations a deformation induced recrystallization recovery (DIRR) mechanistic model was developed and was shown to successfully explain all the above observations.

6.6 Appendix

6.6.1 Grain path envelope formalization

Feret diameter of a convex object is defined as:

$$\mathbf{R}(\theta, \varphi) = f(\mathbf{R}, t, \mathbf{X}, \Gamma) \quad (1)$$

where $\mathbf{R}(\theta, \varphi)$ is assumed to be the average grain-size of the polycrystalline sample and it is a implicit function of \mathbf{R} , annealing time t , position of the grain in the sample in Cartesian coordinate system \mathbf{X} and nucleation time Γ of the concerned grain, θ and φ are the angular positions where the diameter of the object is measured.

Growth rate is defined as the rate of change of the grain-size with time and it is assumed to be independent of the location of the grain in the sample. Each position is assumed to be equivalent in the sample domain.

$$\frac{\partial R}{\partial t} = f(\mathbf{R}, t, \Gamma) \quad (2)$$

Growth rate can be assumed to be size dependent (Eq. 3) or time dependent (Eq. 4). In case of continuous distribution of grain-size, frequency function $f(\mathbf{R}, t)$ is defined such that $f(R, t)dR$ is the fraction of grain-sizes at time t which lie in the range R to $R + dR$. Number density function $n(R, t)$ is also defined where $n(R, t)dR$ is the number of grains per unit volume in the size range R to $R + dR$. $N(t)$ is the number of particles in the structure at time t (Eq. 5).

$$f(\mathbf{R}_1, t_1, \Gamma_1) = f(\mathbf{R}_1, t_2, \Gamma_2) \quad \forall t_2, \Gamma_2 \quad (3)$$

$$f(\mathbf{R}_1, t_1, \Gamma_1) = f(\mathbf{R}_2, t_1, \Gamma_2) \quad \forall \mathbf{R}_2, \Gamma_2 \quad (4)$$

$$n(\mathbf{R}, t) = N(t)f(\mathbf{R}, t) \quad (5)$$

Number of grains of size greater than R can thus be defined by the function (Eq. 6)

$$N_{>}(R, t) = \int_R^{\infty} n(R, t) dR \quad (6)$$

Size distribution can also be expressed in terms of the nucleation rate of the grains from time $t=0$ to $t=\Gamma$, assuming monotonic behaviour.

$$N_{>}(R, t) = \int_R^{\infty} n(R, t) dR = \int_0^{\Gamma(R, t)} \dot{N}(T) dT \quad (7)$$

In case of grain coarsening the grain-size distribution can be expressed in terms of the annihilation rate $A(T)$ as given below.

$$\int_R^{\infty} n(R, t) dR = \int_0^{\infty} n(R, 0) dR - \int_0^{\tau(R, t)} A(T) dT \quad (8)$$

Taking partial derivative with respect to R

$$\left\{ \frac{\partial}{\partial R} \int_R^{\infty} n(R, t) dR \right\}_t = \left\{ \frac{\partial}{\partial R} \left\{ \int_0^{\infty} n(R, 0) dR - \int_0^{\tau(R, t)} A(T) dT \right\} \right\}_t \quad (9)$$

Using Leibniz rule

$$\left\{ \int_R^{\infty} \frac{\partial}{\partial R} n(R, t) dR \right\}_t = - \frac{\partial}{\partial R} \int_0^{\tau(R, t)} A(T) dT = -A(\tau(R, t)) \frac{\partial \tau(R, t)}{\partial R} \quad (10)$$

$$n(R_{\infty}, t) - n(R, t) = -A(\tau(R, t)) \frac{\partial \tau(R, t)}{\partial R} \quad (11)$$

Assuming $n(R_{\infty}, t)$ to be a very small number

$$n(R, t) = A(\tau(R, t)) \frac{\partial \tau(R, t)}{\partial R} \quad (12)$$

Growth rate $G(R, t)$ can be defined as

$$\left(\frac{\partial R}{\partial t}\right)_\Gamma = \frac{dR}{dt} = G(R, t) \quad (13)$$

Growth rate is assumed to be a function of grain-size and time t

$$\frac{dR}{dt} = G(R, t) = f_1(R)f_2(t) \quad (14)$$

$$\int_0^R \frac{dR}{f_1(R)} = \int_\Gamma^t f_2(T)dT$$

Taking partial derivative with respect to R and applying Leibniz rule we get

$$\begin{aligned} -\frac{1}{f_1(R)} &= -f_2(\Gamma) \left(\frac{\partial \Gamma}{\partial R}\right)_t \\ \left(\frac{\partial \Gamma}{\partial R}\right)_t &= -\frac{1}{f_1(R)f_2(\Gamma)} = -\frac{1}{G(R, \Gamma)} \end{aligned} \quad (15)$$

Using the expression of the number density function derived before (Eq. 10) we get

$$n(R, t) = \frac{A[\Gamma(R, t)]}{G[R, \Gamma(R, t)]} \quad (16)$$

$$n(R, t) = \frac{A[\Gamma(R, t)]}{G(R)} \quad (17)$$

$$n(R, t) = \frac{A[\Gamma(R, t)]}{G[\Gamma(R, t)]} \quad (18)$$

Where Γ is the time when all the grains smaller than size R (at time t) gets annihilated.

References

1. B. L. Mordike and T. Ebert, Mater. Sci. Eng. A **302**, 37 (2001).
2. K. U. Kainer, Magnesium – Alloys and Technology (2003).

3. I. J. Polmear, *Mater. Sci. Technol.* **10**, 1 (1994).
4. R. V Allen, D. R. East, T. J. Johnson, W. E. Borbidge, and D. Liang, *Magnes. Technol.* 2001 75 (2001).
5. M. Easton, A. Beer, M. Barnett, C. Davies, G. Dunlop, Y. Durandet, S. Blacket, T. Hilditch, and P. Beggs, *JOM* **60**, 57 (2008).
6. D. Liang and C. B. Cowley, *JOM* **56**, 26 (2004).
7. P. D. Ding, F. S. Pan, B. Jiang, J. Wang, H. L. Li, J. C. Wu, Y. W. Xu, and Y. Wen, *Trans. Nonferrous Met. Soc. China (English Ed.)* **18**, s7 (2008).
8. Y. Wang, S. B. Kang, and J. Cho, *J. Mater. Process. Technol.* **210**, 1270 (2010).
9. Z. Liu, S. Xing, P. Bao, N. Li, S. Yao, and M. Zhang, *Trans. Nonferrous Met. Soc. China* **20**, 776 (2010).
10. S. S. Park, Y. S. Oh, D. H. Kang, and N. J. Kim, *Mater. Sci. Eng. A* **448-451**, 352 (2007).
11. P. Málek, K. Turba, M. Slámová, and I. Drbohlav, *Mater. Charact.* **59**, 1046 (2008).
12. G. W. Greenwood, *Acta Metall.* **4**, 243 (1956).
13. I. M. Lifshitz and V. V Sloyozov, *J. Phys. Chem. Solids* **19**, 35 (1961).
14. C. Wagner, *Z. Electrochem* **65**, 581 (1961).
15. W. A. Johnson and R. F. Mehl, *Tranz AIME* **135**, 416 (1939).
16. M. Avrami, *Chem. Phys.* **7**, 1103 (1939).
17. A. N. Kolmogorov, *Nauk SSSR* **3**, 355 (1937).
18. A. M. Gokhale and R. T. DeHOFF, *Metall. Trans. A* **10A**, 1952 (1979).
19. A. M. Gokhale and R. T. Dehoff, *Metall. Trans. A* **16**, 559 (1985).
20. R. T. Dehoff, *Acta Mater.* **46**, 5175 (1998).
21. P. R. Rios and M. E. Glicksman, *Acta Mater.* **55**, 1565 (2007).
22. P. R. Rios and M. E. Glicksman, *Acta Mater.* **56**, 1165 (2008).
23. M. E. Glicksman, P. R. Rios, and D. J. Lewis, *Acta Mater.* **55**, 4167 (2007).
24. J. W. Cahn, *Mat. Res. Soc. Symp. Proc.* **398**, 425 (1996).
25. R. T. Dehoff, *Metall. Trans. A* (1971).
26. F. G. Yost, *Metall. Trans. A* **6**, 1607 (1975).
27. P. Streitenberger and D. Zöllner, *Acta Mater.* **88**, 334 (2015).
28. H. J. Gundersen and E. B. Jensen, *J. Microsc.* **138**, 127 (1985).
29. M. D. Abràmoff, I. Hospitals, P. J. Magalhães, and M. Abràmoff, *Biophotonics Int.* **11 (7)**, 36 (2004).
30. R. T. DeHoff and G. Q. Liu, *Metall. Trans. A* **16**, 2007 (1985).
31. R. T. Dehoff, *Acta Mater.* **51**, 2259 (2003).

32. A. M. Gokhale, C. V. Iswaran, and R. T. Dehoff, *Metall. Mater. Transactions A* **10**, 1239 (1979).
33. H. Zhao, P. Li, and L. He, *J. Mater. Process. Technol.* **211**, 1197 (2011).
34. F. J. Humphreys and M. Hatherly, *Recrystallization and Related Annealing Phenomenon*, Second Edition (Elsevier, 2004).

Chapter 7

Concluding Remarks

In this thesis, microstructural and texture evolution during friction stir processing (FSP) of AZ31 magnesium alloy was investigated. The thesis started with the study of the origin of the microstructure during friction stir processing. Most of the reported microstructural analysis and evolution during FSP in the literature has been done after looking at the post processed structures. However, the structure had typically undergone post-processing thermal annealing. The latter is unavoidable, as the ultra-fine grains reported in FSW/FSP is expected [1,2] to be extremely unstable and amenable to grain coarsening. In the third chapter of this thesis microstructure evolution very close to the edge region was explored. This region was chosen since it has the highest cooling rate and lowest tool passage time, hence the region mimics the in-situ structures and can be considered as a ‘self-quenching’ experiment. TEM analysis, using lift-out technique, revealed formation of very fine grains and strain localizations in these regions. Given the very fine grains and the large strain rate, grain boundary sliding was proposed as a plausible mechanism of microstructure evolution during friction stir processing. This postulate was supported by the texture measurements for multi-

pass FSP (fourth chapter), which reported no change in texture with increasing number of passes.

This leads to the fourth chapter of the thesis, which talked about the microstructural and textural evolution during multipass friction stir processing. Though FSPs were mostly performed in air, a limited number of FSP were also conducted under water. For FSP under water, grains were smaller, and had higher misorientation and weaker texture. It was observed that the morphological and crystallographic texture was independent of the number of passes, and was determined by the last-pass in a multi-pass sequence. Visco-plastic-self-consistent (VPSC) modeling, plus imposition of appropriate velocity gradients, successfully captured the texture evolution at different locations. Though simulated textures matched the experimental textures remarkably well (and for different sequences of multi-pass FSP), the simulations were 'limited' by von-Mises strain of 1.0. Even at the lower strains (at least one order of magnitude lower than the experimental strains [3]), VPSC simulations had 3-5 times higher texturing than the experimental observations. Based on the experimental observations, following model or mechanism(s) for FSP/FSW microstructural evolution was proposed: Initial local shear plus dynamic recovery/recrystallization leading to ultra-fine grains, deformation being accommodated by ultra-fine grain superplasticity followed by post-FSP grain coarsening. Chapters 3 and 4, thus came up with a new model/hypothesis for FSW/FSP microstructure evolution.

A critical problem in FSW/FSP microstructures is possibility of post-FSW/FSP grain coarsening. Such coarsening can be deleterious to the microstructure and hence properties. Thermal gradients in the process zone, and appropriate use of heat sinks to control this, are critical importance. The fifth chapter of this thesis deals with this aspect: microstructural evolution and thermal profiles during FSP with different heat sinks. Water and liquid nitrogen, together with normal processing in ambient air, were used. Water proved to be a better heat sink than liquid nitrogen, although liquid nitrogen provided cooler ambient temperatures. Experimental observations, on the process zone dimensions and temperature profiles, showed significant differences: highlighting the influence of the thermal history. Thermal profiles in all three cases (air, water and liquid nitrogen) were simulated using a three-dimensional steady-state coupled laminar fluid flow and heat transfer model based developed in COMSOLTM multi-physics software which could successfully capture the experimental observations on process zone dimensions and temperature profiles.

The sixth chapter of the thesis talked about the grain evolution during annealing of AZ31 alloy sheet produced from another emerging and very significant processing technique for magnesium alloys, i.e. twin roll casting (TRC). Annealing of twin roll cast AZ31 was done at 300°C and 500°C for varying times and grain evolution was studied using large set of data points obtained from the intercept length counting of the through thickness micrographs. The phenomenon of nucleation at the start of annealing at both the temperature was quantitatively captured. Grain size initially decreased with respect to the as received sheet and increased with further annealing. However, the bimodality of the structures as observed in the as received twin rolled sheet was maintained for higher annealing times for the annealing temperature of 300°C but the bimodality was lost for the annealing temperature of 500°C. This leads to the query for the grain evolution mechanism at these two temperatures which was explained by the proposed deformation induced recrystallization recovery (DIRR) mechanistic model.

References

1. P. B. Prangnell and C. P. Heason, *Acta Mater.* **53**, 3179 (2005).
2. J.-Q. Su, T. W. Nelson, and C. J. Sterling, *Mater. Sci. Eng. A* **405**, 277 (2005).
3. Z. Y. Ma, *Metall. Mater. Trans. A* **39**, 642 (2008).

List of journal publications from thesis

1. **A. Tripathi**, A. Tewari, N. Srinivasan, G.M. Reddy, S.M. Zhu, J.F. Nie, R.D. Doherty and I. Samajdar, Microstructural Origin of Friction Stir Processed Zone in a Magnesium Alloy, *Metallurgical and Materials Transactions A*, Volume 46, Issue 8, 3333-3336, 2015
2. **A. Tripathi**, A. Tewari, A.K. Kanjarla, N. Srinivasan, G.M. Reddy, S.M. Zhu, J.F. Nie, R.D. Doherty and I. Samajdar, Microstructural Evolution During Multi-Pass Friction Stir Processing of a Magnesium Alloy, *Metallurgical and Materials Transactions A*, Volume 47A, 2201-2216, 2016
3. **A. Tripathi**, I. Samajdar, J.F. Nie and A. Tewari, Study of grain structure evolution during annealing of a twin-roll-cast Mg alloy, *Materials Characterization*, 114, 157-165, 2016
4. **A. Tripathi**, A. Tewari, K. Mohan, N. Srinivasan, G.M. Reddy, J.F. Nie and I. Samajdar, Friction stir processing of AZ31 magnesium alloy under different cooling conditions: numerical simulation and experimental validation, *Submitted to Journal of Materials Processing Technology* (PROTEC-S-16-01409)

Other publications/work (during PhD)

5. **A. Tripathi**, I. Samajdar, A. Tewari, A.K. Kanjarla, N. Srinivasan, G.M. Reddy and J.F. Nie, Texture and microstructure developments during friction stir processing of magnesium alloy AZ31, Volume 3, 2013, 1516-1517, *Materials Science and Technology*, Montreal, Canada, 2013
6. M.Z. Bian, **A. Tripathi**, H. Yu, N.D. Nam and L.M. Yan, Effect of aluminium content on the texture and mechanical behaviour of Mg 1wt% Mn wrought magnesium alloys, *Materials Science and Engineering A* 639, 320-326, 2015
7. A. Mierczynska, A. Michelmore, **A. Tripathi**, R.V. Goreham, R. Sedeva and K. Vasilev, pH-tunable gradients of wettability and surface potential, *Soft Matter*, 8, 8399-8404, 2012
8. **A. Tripathi**, A. Tewari, S. Murty and I. Samajdar, Microstructural and texture evolution during groove rolling of AZ31 Mg alloy at different temperatures (work in progress)

Selected oral/poster presentations (during PhD)

1. **A. Tripathi**, A. Tewari, A.K. Kanjarla, G.M. Reddy, N. Srinivasan, J.F.Nie and I. Samajdar: Friction Stir Processing of Magnesium: Defining the Microstructural Anisotropy, The Indian Institute of Metals (IIM), National Metallurgist Day (NMD), Annual Technical Meet (ATM), 12-15 November 2014, at Pune, India (Oral)
2. **A. Tripathi**, A. Tewari, S.M. Zhu, I. Samajdar and J.F. Nie, Effect of coolant on the texture and micro structure developments during Friction Stir Processing of magnesium alloy AZ31, The 8th International Conference on Advanced Materials Processing (ICAMP 8), 27-30 July 2014, at Gold Coast, Queensland, Australia (Oral)
3. **A. Tripathi**, A. Tewari, A.K. Kanjarla, G.M Reddy, N Srinivasan, J.F.Nie and I Samajdar: Friction Stir Processing of AZ31 Mg alloy, 8th International Conference on Processing and Manufacturing of Advanced Materials (THERMEC 2013), at Las Vegas, Nevada, USA, 2-6 December, 2013 (Poster)
4. **A. Tripathi**, A. Tewari, A.K. Kanjarla, G.M Reddy, N Srinivasan, J.F.Nie and I Samajdar: Texture and Microstructure Developments during Friction Stir Processing (FSP) of AZ31 Magnesium Alloy, Materials Science and Technology 2013 (MS and T 13), at Montreal, Quebec, Canada, 27-31 October, 2013 (Oral)
5. **A. Tripathi**, A. Tewari, A.K. Kanjarla, G.M Reddy, N Srinivasan, J.F.Nie and I Samajdar: Microstructural and Texture Evolution during Friction Stir Processing of AZ31 Magnesium alloy, National Conference on Advances in Naval Materials ADNAM 2013, 22-23 February 2013, at IIT Madras, India (Poster)
6. **A. Tripathi**, A. Tewari, A.K. Kanjarla, G.M Reddy, N Srinivasan, J.F.Nie and I Samajdar: Poster Presentation, Microstructural Evolution of AZ31 Mg alloy under Severe Plastic Deformation, 16th International Conference of Texture of Materials (ICOTOM 16), 12-17 December 2011 at IIT Bombay, Mumbai, India (Poster)